MOLECULAR & NANOTECHNOLOGY

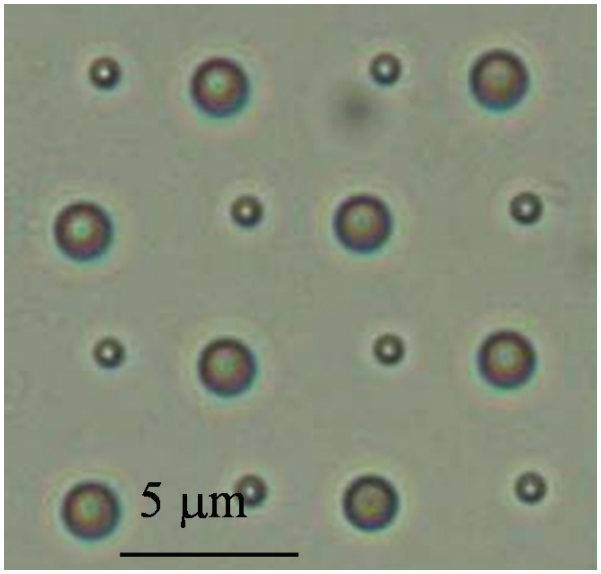

▲ Optical micrograph of 600 nm and 2 μm spheres assembled into designated sites on a surfaces (K.-J. Lee, T.S. Cho, A.P. Chandrakasan, J. Kon, p. 175).

Studies of Field Ionization Using PECVD-grown CNT Tips 150
Combinatorial Sensing Arrays of Phthalocyanine-based Field-effect Transistors 151
Nanoelectromechanical Switches and Memories 152
Growth of Carbon Nanotubes for Use in Origami Supercapacitors 153
Self-Alignment of Folded, Thin-Membranes via Nanomagnet Attractive Forces 154
Control System Design for the Nanostructured Origami™ 3D Nanofabrication Process 155
Tomographic Interferometry for Detection of Nafion® Membrane Degradation in PEM Fuel Cells 156
Modelling the Optical Properties of Superconducting Nanowire Single-photon Detectors 157
Using Optical Mixtures of Materials to Control Index, Speed of Light, and Transparency 158
Increasing Detection Efficiency of Superconducting Nanowire Single-photon Detectors 159
Enhancing Etch Resistance of Nanostructured Spin-on-Glass Electron Resist via Post-Develop Electron Curing 160
Robust Shadow-Mask Evaporation via Lithography-Controlled Undercut 161
Pattern Generation Using Multi-Step Room-Temperature Nanoimprint Lithography 162
Modeling of Electrical and Thermal Response of Superconducting Nanowire Single Photon Detectors (SNSPD) 163
Quantum Dot Photodetectors Deposited via Microcontact Printing 164
Microcontact Printing of J-Aggregate Thin Films for Photonic Devices 165
Measuring Thermal and Thermoelectric Properties of Single Nanowires and Carbon Nanotubes 166
Nanocomposites as Thermoelectric Materials 167
Flux and Force due to Near-field Thermal Radiation 168
CNT Assembly by Nanopelleting 169
Integrated Carbon Nanotube Sensors 170
Templated Assembly by Selective Removal 171
Vibrational, Thermodynamic, and Transport Properties of Carbon Nanotubes from Density-functional Perturbation Theory 172
Static Dielectric Response of Single-wall and Multi-wall Carbon Nanotubes from First-principles 173
Niobium Superconducting Persistent-Current Qubits with Deep Submicron Josephson Junctions 174
Mach-Zehnder Interferometry in a Persistent-Current Qubit 175
Coherent Quasi-classical Dynamics of a Niobium Persistent-Current Qubit 176
Resonant Readout of a Persistent Current Qubit 177
Type-II Quantum Computing Using Superconducting Qubits 178
Scalable Superconducting Architecture for Adiabatic Quantum Computation 179
Fabrication Methods for Adiabatic Quantum Computing Devices 180
Probing Decoherence with Electromagnetically Induced Transparency in Superconductive Quantum Circuits 181
Magnetoelastic Behavior of Magnetic Nanostructures 182
Templated Self-assembly of Block Copolymers for Nanolithography 183
Scanning Beam Interference Lithography 184
Nanofabricated Reflection and Transmission Gratings 185
Nanometrology 186
Building Three-dimensional Nanostructures via Membrane Folding 187
Fabrication of Nanostructured Optical Fiber-to-Chip Couplers 188
Polarization-insensitive Optical Add-drop Multiplexers in Silicon Nitride 189
Nanofabrication of Reconfigurable Optical Add-drop Multiplexers in Silicon 190
Nanofabrication of Optical Microring Filter Banks for Ultra-fast Analog-to-Digital Converters 191
Imprint Lithography with Multilevel Alignment via Interferometric-Spatial-Phase Imaging 192
Interference Lithography 193
Immersion-Achromatic-Interference Lithography 194
Three-dimensional Photonic Crystals by Membrane Assembly 195
Absorbance-Modulation Optical Lithography 196
Zone-Plate-Array Lithography (ZPAL) 197
Spatial-phase-locked E-beam Lithography 198
Controlled Assembly of 20-nm-diameter Gold Nanoparticles into Nanogaps using AC Dielectrophoresis 199
Carbon Nanotube Assembly for Interconnect and Device Applications 200
Catalyst Engineering and Nanowire Growth Mechanisms 201
Templated Self-Assembly for Nano-particle Organization: Solid State Dewetting 202
Catalyst Engineering and Carbon Nanotube Growth Mechanisms 203
Templated Self-Assembly for Nano-Particle Organization: Templated, Ordered Porous Alumina Templates 204
Templated Dewetting of Nano-Particle Solutions 205
Surface Mound Formation and Stress Evolution during Growth of High-Mobility Metal Films 206

Stress and Structure Evolution Film Formation through Island Coalescence 207
Hybrid Carbon Nanotube-Composite Architectures 208

for additional reading…

Fabrication of Germanium-on-Insulator by Means of Wafer Bonding and Layer Transfer 56
Towards MOS Memory Devices Containing 1 nm Silicon Nanoparticles 58
Surface Electromigration and Void Dynamics in Copper Interconnects 85
Bonded Copper Interconnects and Integrated Microchannels for 3D Integrated Circuits 86
A Double-gated CNF Tip Array for Electron-impact Ionization and Field Ionization 90
A MEMS Electrometer for Gas Sensing 94
A Single-Gated CNT Field-Ionizer Array with Open Architecture 95
A MEMS Quadrupole that Uses a Meso-scaled DRIE-patterned Spring Assembly System 96
Aligning and Latching Nano-structured Membranes in 3D Micro-Structures 98
Microfluidic Synthesis and Surface Engineering of Colloidal Nanoparticles 117
Microreactors for Synthesis of Quantum Dots 121
A Nanoscanning Platform for Biological Assays 124
Self-powered Wireless Monitoring System Using MEMS Piezoelectric Micro Power Generator 126
Atomic Force Microscopy with Inherent Disturbance Suppression for Nanostructure Imaging 131
A Low Contact Resistance MEMS-Relay 139
Organic Photovoltaics with External Antennas 211
Optical Models of Organic Photovoltaic Cells 212
Percolation Model of Charge Transport in Organic Semiconductors 213
Energy Transfer from an Organic Phosphorescent Thin Film to a Monolayer of Quantum Dots 217
Charge Dynamics in Organic Heterojunction Lateral Photoconductors 220
Packing of Quantum Dot Monolayers 221
Energy Disorder and Device Performance in Organic Electronics 222
Resonant Cavity Quantum Dot LEDs 225
Patterning Micron-Sized Features of Quantum Dots and Metal Electrodes 226

Studies of Field Ionization Using PECVD-grown CNT Tips

B. Adeoti, A.I. Akinwande
Sponsorship: DARPA

The Micro Gas Analyzer project aims to develop the technology for portable, real-time sensors intended for chemical warfare and civilian air-purity control. For the analyzer, we are developing a field ionizer array based on gated CNTs. We plan to use arrays of CNTs because their small tip radii and high aspect ratio yield high fields at low voltage. One possible configuration for the device is to bias the CNTs to the highest potential and the collecting anode to the lowest potential. The electrons in the outer shell of the molecules tunnel out due to the ambient high electric fields, which serve to lower the unperturbed potential barrier seen by the electrons (Figure 1). The tunneling effect is a purely quantum-mechanical process whose probability of occurrence is strongly dependent on the applied electric fields [1]. We optimize the electron current by varying structural parameters in our device. The most relevant parameters include the radius of curvature, height, base radius and base angle of the grown tip; height and thickness of the tip; and the gate aperture. Varying the gate (or oxide) height without updating the height of the CNT yields the derivable result that the electric field is maximized with the tip peaks at about the same height as the gate. When the tip height is varied in sync with the height of the gate (or oxide), we see that an independent optimum height exists (Figure 2). The value of this height will depend, among other variables, on the electrostatic properties of the insulating material and the actual dimensions of the rest of the structure. These simulation results are being verified by experiment.

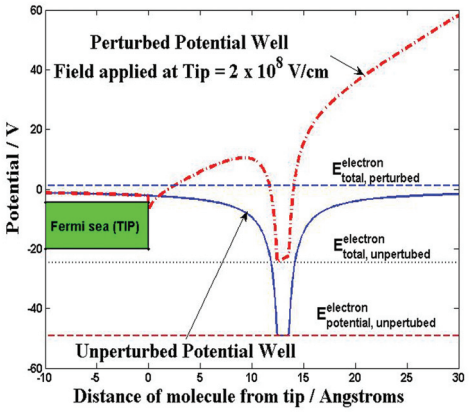

▲ Figure 1: Representative picture of potential barrier faced by electron in a single molecule when the molecule is close to a tip biased at a high potential.

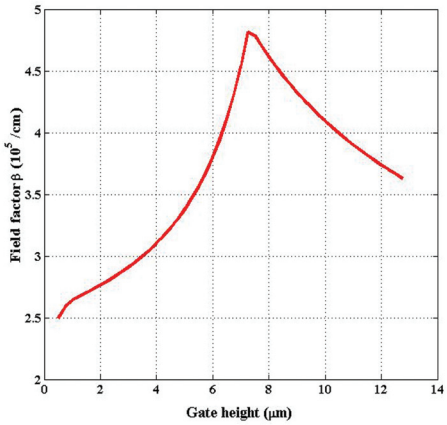

▲ Figure 2: Field factor ß for various heights of gate. Tip height was varied in sync with gate height so that the tip remained within the range of the gate width. A field ionization configuration was used. [CNT] : roc = 5.01 nm | Base: angle=85 , radius=101 nm [GATE] : Aperture=1.01 µm Thickness=0.301 µm V_{CNT} = 10 V, V_{GATE} = 0 V, V_{ANODE} = -150 V

REFERENCES

[1] R. Gomer, *Field Emission & Field Ionization*, Cambridge: Harvard University Press, 1961.

Combinatorial Sensing Arrays of Phthalocyanine-based Field-effect Transistors

M. Bora, D. Schut (HP), M.A. Baldo

Of the millions of molecular species floating in air or dissolved in water, a substantial fraction can be smelled and uniquely discriminated[1]. Biological systems achieve this functionality with a multitude of non-specific receptors. In this project, we are developing gas sensors based on combinatorial arrays of organic transistors. The combinatorial approach reduces the need to develop specific receptors for each and every molecule of interest. Rather, our sensors are based on exploiting the wide variation in interactions between molecules and metal ions[2], an approach previously employed in colorimetric sensors[3].

We have fabricated gas-sensitive organic transistors each consisting of an approximately 10-nm-thick polycrystalline layer of a metallophthalocyanine (MPC) with gold source and drain contacts. The width and length of the channel for each transistor is 2 mm and 50 μm, respectively. The charge-carrier mobility is typically between 10^{-3} and 10^{-4} cm^2/Vs. But the transconductances of various MPC transistors (CoPC, CuPC, ZnPC, and NiPC) are observed to vary when exposed to different gases (acetonitrile, tetrahydrofuran, and toluene); channel current in MPC transistors decreases linearly with increasing solvent concentration (Figure 1). The transient response of the current modulation (Figure 2) is chemically selective and depends on the interaction between the solvent and the central metal atom in the MPC. The linear dependence of channel current on solvent concentration, the steady state current modulation, and the transient response of the MPC transistors are all consistent with the disruption of percolation pathways leading to modulation of transistor channel currents. Since the sensors can be manufactured simply by inkjet printing on a patterned substrate, they may find application as single-use diagnostic aids.

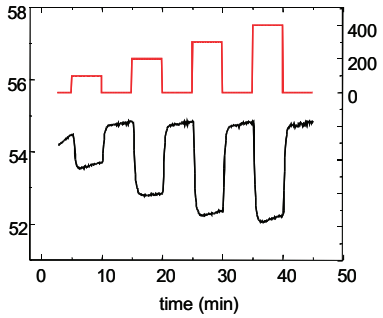

▲ Figure 1: The linearity of MPC sensors is tested by modulating the solvent concentration (V_{ds}=-20V, V_g=-20 V).

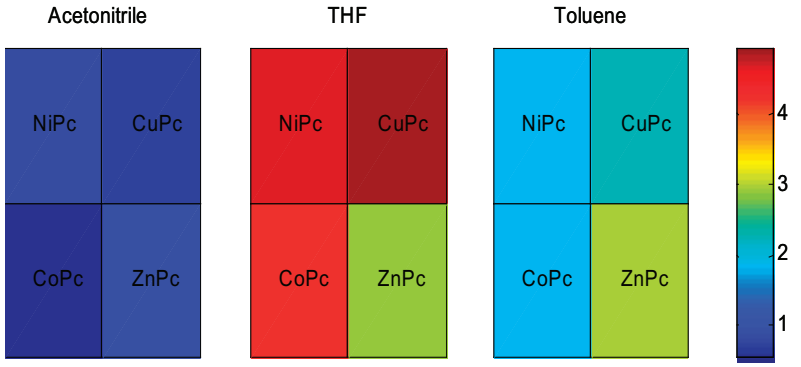

▲ Figure 2: The transient rate of channel current recovery, k_{OFF}, after removal of solvent vapor in units of min^{-1}, summarized for various MPC-solvent combinations. Transistor bias conditions are V_{ds}=-20 V, V_g=-20 V.

REFERENCES:

[1] P. Mombaerts, "Seven-transmembrane proteins as odorant and chemosensory receptors," *Science*, vol. 286, pp. 707-711, 1999.

[2] J. Wang, Z.A. Luthey-Schulten, and K.S. Suslick, "Is the olfactory receptor a metalloprotein?" in *Proc. of the Nat'l. Academy of Sciences of the United States of America*, vol. 100, pp. 3035-3039, 2003.

[3] N.A. Rakow and K.S. Suslick, "A colorimetric sensor array for odor visualization," *Nature*, vol. 406, pp. 710-713, 2000.

Nanoelectromechanical Switches and Memories

K.M. Milaninia, M.A. Baldo
Sponsorship: MARCO MSD, ISN

The ability to change shape is a compelling attraction of molecular semiconductors. Compared to rigid inorganic materials, molecules are soft and malleable, and their conformational changes are essential to the functionality of biological systems. Applications of nano-electro-mechanical (NEM) molecular devices include memories and transistors. Information can be stored in the conformation of molecules, potentially leading to very high density memories; molecular transistors that change shape under bias could exhibit sub-threshold slopes of << 60 mV/decade[1]. Indeed, as an example of the potential of NEMs, voltage gated ion channels possess subthreshold slopes of approximately 15 mV/decade [2].

Although many materials are available for NEM applications, carbon nanotubes exhibit low resistance and good mechanical properties. In this project, we are constructing a NEM testbed. The proposed design for our relay is shown in Figure 1. Nanotubes are directly grown at the bottom of an electron-beam defined trench etched in Si. This offers better control over nanotube growth and removes the need for additional steps that are required for the removal of surfactants and organics from the surface of the nanotubes. Because the nanotubes are vertically oriented, we are able to take advantage of the smallest size feature of the carbon nanotube - its diameter. This allows us to create dense arrays of relays for applications such as memory or logic devices. The vertical orientation allows NEM structures with very large aspect ratios. Theoretical results[3] have shown that increasing the aspect ratio of a carbon nanotube reduces the voltage needed to pull in the nanotube and thereby reduces the power requirement. Furthermore, because of the ability to easily functionalize the surface of nanotubes, we can functionalize the tube with charge to lower the pull-in voltage even further.

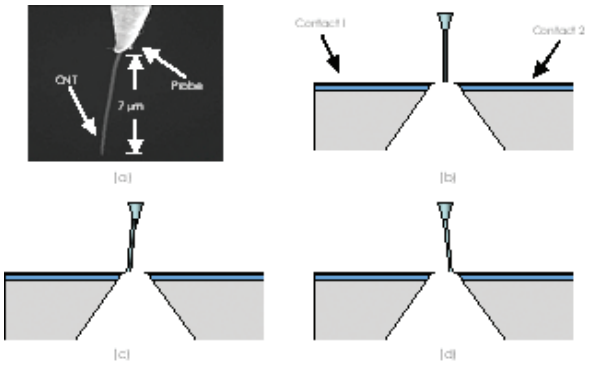

▲ Figure 1: Initial results were obtained by introducing a (a) carbon nanotube mounted to a tungsten probe between two (Au/SiO2/Si) contacts. (b),(c), and (d) are schematics of the device in state 1 (its initial state), state 2, and state 3, respectively.

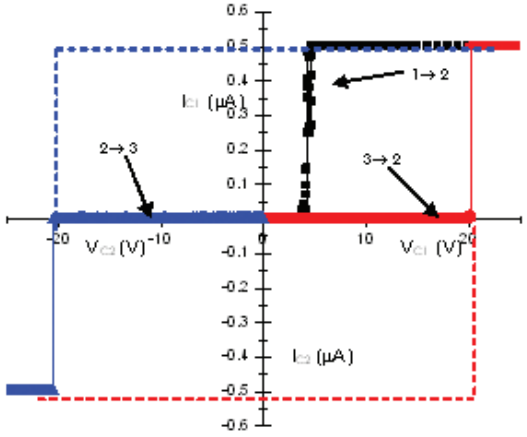

▲ Figure 2: An I-V of device being switched from state 1→2 by applying a bias between Contact 1 and CNT, then switched from state 2→3 by applying a bias between Contact 2 and CNT, and finally from state 3→2 by applying a bias between Contact 1 and CNT.

REFERENCES

[1] A.W. Ghosh, T. Rakshit, and S. Datta, "Gating of a molecular transistor: Electrostatic and conformational," *Nano Letters*, vol. 4, pp. 565-568, 2004.

[2] A.L. Hodgkin and A.F. Huxley, "Currents carried by sodium, potassium ions through the membrane of the giant squid axon of Logilo," *J. of Physiology*, vol. 116, pp. 449-472, 1952.

[3] M. Dequesnes, S.V. Rotkin, and N.R. Aluru, "Calculation of pull-in voltages for carbon-nanotube-based nanoelectromechanical switches," *Nanotechnology*, vol. 13, pp. 120-131, 2002.

Growth of Carbon Nanotubes for Use in Origami Supercapacitors

H.J. In, S. Kumar, Y. Shao-Horn, G. Barbastathis
Sponsorship: MARCO IFC, ISN, NSF SGER

The Nanostructured Origami™ 3D fabrication and assembly process can be used to create nanostructured, three-dimensional (3D) devices exclusively through existing 2D micro- and nano-fabrication techniques. Previously, the folding method was used in fabricating an origami supercapacitor with carbon electrodes [1]. The carbon electrode material was composed of 99 wt% Super P carbon black and 1 wt% polyvinylidene fluoride binder in N-methyl-2-pyrrolidone. This mixture was highly porous with a very high specific surface area and resulted in microscale supercapacitors with a high specific capacitance. However, the material had to be deposited manually using a probe tip, and its exact properties, e.g., surface area and variations in pore size could not be determined precisely. To enable *in situ* deposition of the electrode material, multi-walled carbon nanotubes (CNTs) were grown through a plasma-enhanced chemical-vapor deposition (PECVD) method in place of the manually deposited carbon paint. Moreover, as Figures 1 and 2 partially illustrate, growth conditions of the nanotubes determine their density, length, diameter, etc. Being able to control the nanotube properties will allow us to more carefully characterize the electrochemical properties of the origami supercapacitors. All nanotubes were grown using S. Kim group's PECVD CNT deposition equipment.

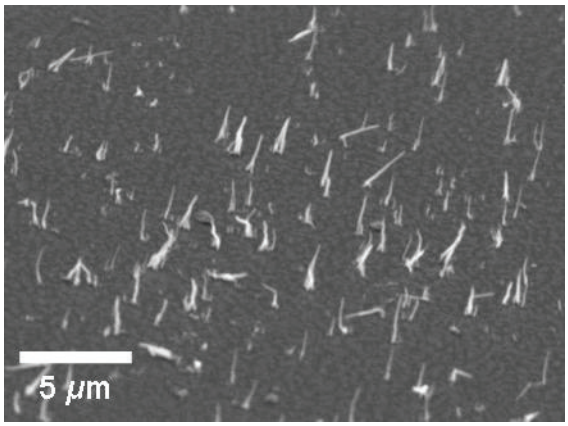

▲ Figure 1: Low-density growth of carbon nanotubes. Each tube is approximately 2 microns long.

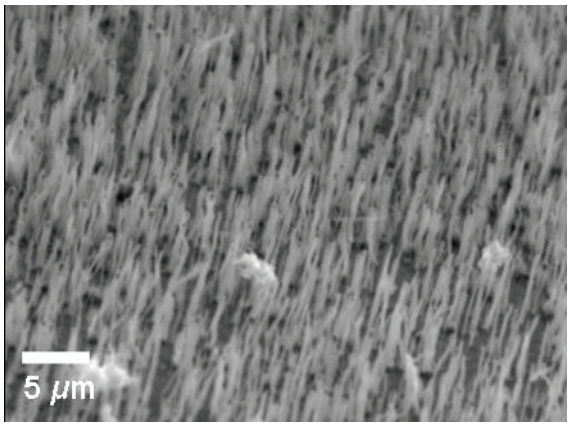

▲ Figure 2: High-density growth of carbon nanotubes.

REFERENCES

[1] H.J. In, S. Kumar, Y. Shao-Horn, and G. Barbastathis, "Origami fabrication of nanostructured, three-dimensional devices: Electrochemical capacitors with carbon electrodes," *App. Phys. Lett.*, vol. 88, no. 8, pp. 083104:1-3, Feb. 2006.

[2] T.A. El-Aguizy, J.-H. Jeong, Y.-B. Jeon, W.Z. Li, Z.F. Ren, and S.-G. Kim, "Transplanting carbon nanotubes," *App. Phys. Lett.*, vol. 85, no. 24, pp. 5995-5997, Dec. 2004.

[3] Z.F. Ren, Z.P. Huang, J.W. Xu, J.H. Wang, P. Bush, M.P. Siegal, and P.N. Provencio, "Synthesis of large arrays of well-aligned carbon nanotubes on glass," *Science*, vol. 282, pp. 105-1107, Nov. 1998.

Self-Alignment of Folded, Thin-Membranes via Nanomagnet Attractive Forces

A. Nichol, W.J. Arora, F.J. Castaño, G. Barbastathis
Sponsorship: ISN, MARCO IFC

We are developing a thin-membrane self-alignment technique based on the attractive force between arrays of nano-patterned magnetic material (nanomagnets). The alignment scheme shown in Figure 1 will be applied in the Nanostructured Origami™ fabrication method [1], which involves first nano-patterning membranes using 2D lithography and then folding the membranes in a 3D configuration. We have shown that the scaling of the attractive force between magnets is favorable for this application. The research is moving towards a completely self-assembling, 3D nanofabrication method with better than 50-nm accuracy of feature placement for use in 3D photonics, 3D integrated circuits, and other 3D hybrid devices.

Nanomagnets with preferred magnetization in-plane can be patterned on thin-membranes with nano-scale precision using e-beam lithography, e-beam evaporation for the metallization steps, and liftoff processing. The alignment system uses a large array of nanomagnets to increase force and to average out the local errors in magnetic pole positions. A dynamic model of the system has shown a significant dependency on the number of magnets for the precision of the final alignment.

The magnetic alignment scheme is most effective when the folding takes place in an external magnetic field that holds a common magnetization direction for the nanomagnets. The addition of an external field allows the use of soft magnetic material operating at saturation. This reduces processing constraints because hard permanent nanomagnets at this scale are more difficult to fabricate than soft magnets. Furthermore, the torque due to the external field provides alignment about two axes of rotation. Using a dipole approximation along with finite element magnetic modeling (FEMM) [2], we have determined the alignment forces that can be achieved with this method. A plot of the forces between two 100 nm x 1 µm x 3 µm saturated iron nanomagnets appears in Figure 2. We are characterizing the alignment force experimentally using sensitive 300 nm-thick silicon nitride flexures that have been e-beam-patterned with iron nanomagnets.

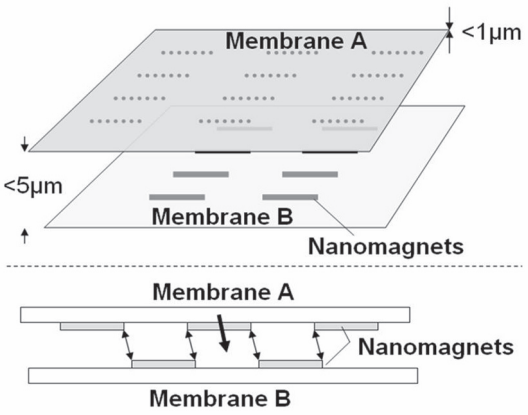

▲ Figure 1: Schematic of the alignment system of nanomagnets. The two membranes are patterned with magnetic material that is magnetized in-plane by using an external magnetic field. When the coarse alignment brings them close enough, self-alignment occurs.

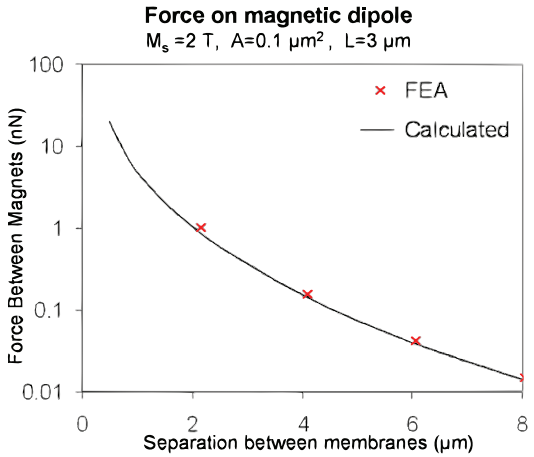

▲ Figure 2: The force exerted on a single 100 nm x 1 µm x 3 µm magnetically saturated iron nanomagnet by similarly-sized magnets on the other membrane. The force is highly dependent on the separation between the membranes.

REFERENCES

[1] S.M. Jurga, "Nanostructured Origami," *Third IEEE Conference on Nanotechnology,* vol. 2, pt. 2, 2003, pp. 220-223.
[2] D. Meeker. (2005.) *Finite Element Method Magnetic* v.3.4. [online]. Available: http://femm.foster-miller.net/

Control System Design for the Nanostructured Origami™ 3D Nanofabrication Process

P. Stellman, G. Barbastathis
Sponsorship: NSF, MARCO IFC, ISN

Nanostructured Origami™ is the 3D nanomanufacturing process that folds patterned membranes into useful 3D structures. Since the origami segments must be accurately aligned in the 3D folded state, the actuation mechanisms for Nanostructured Origami must be both controllable and repeatable. Accurate analytical models of the actuation are therefore necessary to expedite the design of complex origamis. We borrow techniques from the robotics community to simulate the motion of the origami as it folds from 2D to its 3D shape. The dynamics of the folding process are computed using wrench calculus [1] and are used to design a control scheme for folding the segments in the laboratory. A PD position control scheme is briefly described here.

To date, we have modeled the dynamics of two classes of origamis: accordions and single-vertex origamis [2]. In this abstract, we describe the analysis of a single-vertex origami referred to as the corner cube. The creases are modeled as revolute joints, which represent the generalized coordinates of the systems. The segments of the origami are assumed to remain rigid throughout the origami's motion. This allows us to use screw calculus [1] to describe the geometry and kinematics of the corner cube. Since the corner cube has a closed chain kinematic topology, the motion of the segments is interdependent. The dependencies are manifested through holonomic equality constraints. The corner cube is then virtually cut at an unactuated joint, and the dynamics of the resulting one degree-of-freedom system are computed. The equations of motion of the system are then formed according to the principles outlined in [1]. These nonlinear equations can be integrated in time to simulate the trajectory of the origamis. The dynamic response of the corner cube subject to a PD controller is shown in Figure 1, and its trajectory is illustrated in Figure 2. The final folded state of the corner cube is also guaranteed to be stable for a stress actuation method since the stiffness matrix is positive definite.

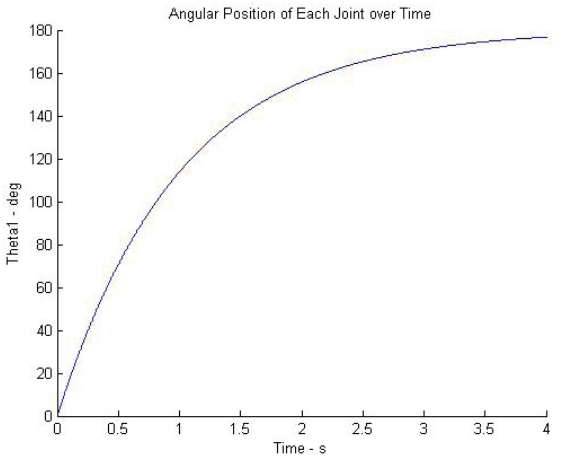

▲ Figure 1: Dynamic response of driving joint of corner cube when subject to an input torque following the PD control law.

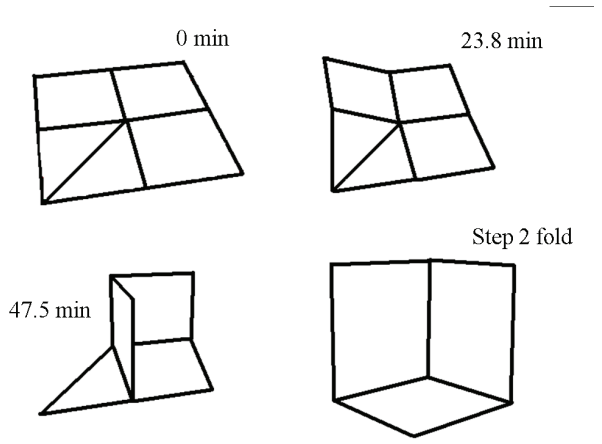

▲ Figure 2: Trajectory of corner cube as it folds from the flat to the folded state.

REFERENCES

[1] R.M. Murray, Z.Li, and S.S. Sastry, *A Mathematical Introduction to Robotic Manipulation*. Boca Raton, FL: CRC Press, 1994, Ch. 2-5.

[2] P. Stellman and G. Barbastathis, "Design and Control of Nanostructured Origami," in *Proc. of 3rd Annual Int'l. Symp. on Nanomanufacturing*, Limassol, Cyprus, November 2005.

Tomographic Interferometry for Detection of Nafion® Membrane Degradation in PEM Fuel Cells

L. Waller, J. Kim, G. Barbastathis, Y. Shao-Horn
Sponsorship: DuPont-MIT Alliance

At present, membrane degradation and failure are the main limitations on the lifetime of proton exchange membrane (PEM) fuel cell systems [1]. Nafion® membranes, produced by DuPont, have excellent proton conductivity and relatively good chemical stability. However, fundamental studies of the degradation mechanisms of Nafion membranes are needed in order to optimize membrane design. Our goal is to correlate indirect and *ex-situ* measurements with *in situ* monitoring of membrane microstructural changes in order to better understand how the membrane thins or forms pinholes and voids.

We are conducting atomic force microscopy (AFM) studies of both fresh and degraded *ex-situ* Nafion samples to study the changes in the microstructure of the Nafion as it degrades. These studies will be used to guide optical characterization of the Nafion® membrane *in situ*. The goal of the *in situ* optical studies is to construct a refractive index profile of the membrane while the fuel cell is in use. We place the fuel cell system inside one leg of a Mach-Zehnder interferometer (Figure 1). The membrane, which has an average refractive index of 1.35 (room temperature, 20%RH) [2], will act as a phase object, and the phase delay at any point in the x-y plane is proportional to the refractive index at that point. Thus, a 2D map of the refractive index in the membrane can be constructed from the interference pattern, which is recorded on a CCD camera (Figure 2). The refractive index is related to membrane density at each point by the Lorentz-Lorentz relation. We focus on density changes due to temperature, pressure, and humidity, which occur on different orders of magnitude. Simulations are used to solve the forward problem through the optical system and to compute the inverse problem, which can then be used to estimate the refractive-index profile of the membrane from the measured interference pattern.

In situ profiling of the Nafion membrane will allow us to observe exactly where and how the membrane degrades. Our approach is non-invasive and provides a 2D distribution of water uptake, stresses, and micropores in the membrane. The technique can be extended to 3D with tomographic techniques. A better understanding of the mechanisms of membrane failure will give insight into membrane and fuel cell design.

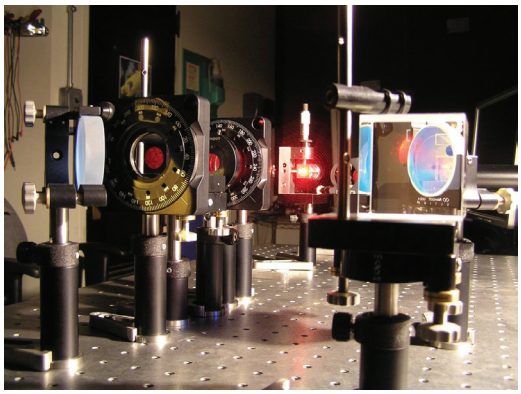

▲ Figure 1: Experimental set-up of PEM fuel cell within a Mach-Zehnder interferometer. Fringe patterns yield a map of the refractive index of the fuel cell membrane.

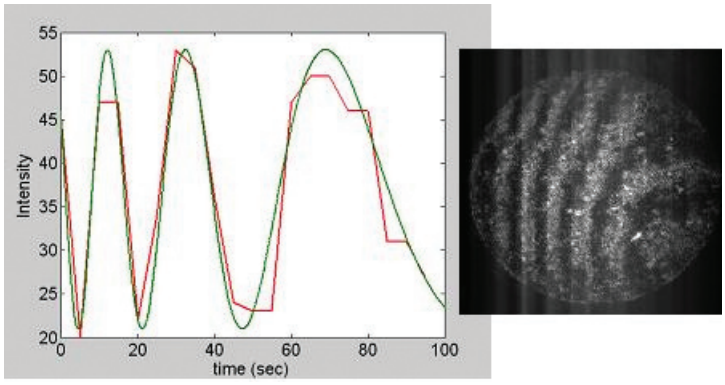

▲ Figure 2: Measured fringe pattern (right) and the corresponding intensity vs. time plot for several specific points (left) for a Nafion® membrane as it cools. Chirped sinusoid is a result of decreasing temperature.

REFERENCES

[1] A.B. LaConti, M. Hamilton, and R.C. McDonald, "Mechanisms of membrane degradation," *Handbook of Fuel Cells – Fundamentals, Technology, and Applications, vol. 3.* New York: John Wiley & Sons, Inc., 2003.

[2] M.N. Weiss, R. Srivastava, and H. Groer, "Experimental investigation of a surface plasmon-based integrated-optic humidity sensor," *Electronics Letters*, vol. 32, no. 9, pp. 842-843, Apr. 1996.

Modelling the Optical Properties of Superconducting Nanowire Single-photon Detectors

V. Anant, A.J. Kerman, J.K. Yang, E.A. Dauler, K.M. Rosfjord, K.K. Berggren
Sponsorship: United States Air Force

Polarization-sensitive single-photon detectors can be useful for high-speed optical and quantum communication where one can encode information in the polarization of the photon. We have observed that superconducting nanowire single-photon detectors (SNSPD) fabricated at MIT exhibit sensitivity to polarization. For this project, we will investigate the polarization sensitivity for devices with various geometries and conduct numerical simulations that explain the sensitivity. Our SNSPDs consist of a nanowire in a meandering pattern that acts as an optical wire-grid polarizer. In order to corroborate our model with experimental results, we approximated the meander geometry with wire arrays characterized by two parameters: pitch (periodicity) and fill-factor (the ratio of wire-width to pitch). We conducted finite-element-method (FEM) simulations of the absorptance of polarized radiation to wire grids. The simulations show that meanders with small pitch and small fill-factors will exhibit larger sensitivity to photon polarization than meanders with large pitch and fill-factors. We intend to use our results to design SNSPDs that are optimized for enhanced sensitivity to polarization. The FEM simulations also show this sensitivity of SNSPDs with integrated optical cavities that have been reported to exhibit detection efficiencies of 57% at 1550 nm wavelength and 67% at 1064 nm [1].

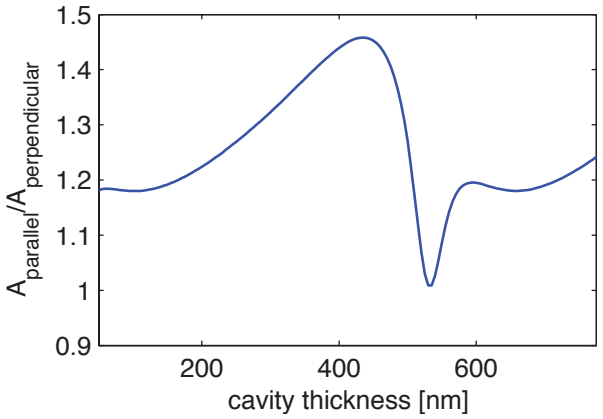

▲ Figure 1: Plot showing the expected ratio of absoptances for electric fields polarized parallel and perpendicular to the nanowires as a function of cavity thickness for a SNSPD with an integrated optical cavity. The nanowire detector is modelled as an array of 100-nm-wide parallel wires at a 200 nm pitch. The material set and relavent optical constants are given in [1].

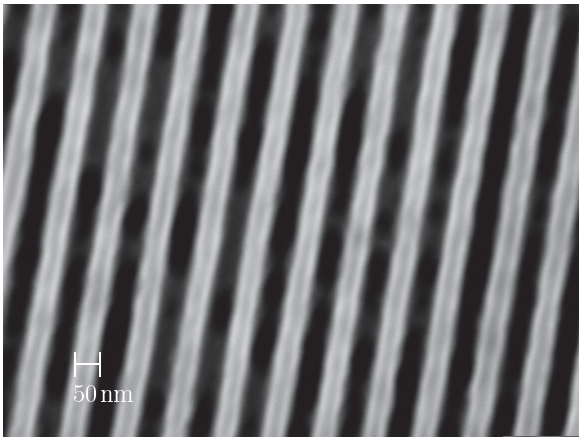

▲ Figure 2: Scanning electron micrograph of a microfabricated structure on a sapphire substrate. The structure is composed of 50-nm-wide wires at a pitch of 100 nm. After the underlying NbN is etched, this structure (and others with different fill-factors and wire widths) can be used to measure the dependence of polarization on absorptance.

REFERENCES

[1] K.M. Rosfjord, J.K.W. Yang, E.A. Dauler, A.J. Kerman, V. Anant, B.M. Voronov, G.N. Gol'tsman, and K.K. Berggren, "Nanowire single-photon detector with an integrated optical cavity and anti-reflection coating," *Optics Express*, vol. 14, no. 2, pp. 527-534, Jan. 2006.

Using Optical Mixtures of Materials to Control Index, Speed of Light, and Transparency

V. Anant, A.F. Abouraddy, K.K. Berggren
Sponsorship: United States Air Force

Recent achievements in optical physics have dramatically redefined the limits of attainable optical properties in materials. Novel optical phenomena, including electromagnetically induced transparency [1], slow light [2], and superluminal speed [3] have been demonstrated in diverse physical implementations. Building on our previous work [4], we have developed a unified approach to engineering optical materials that exhibit these phenomena by using mixtures of simple optical materials near resonances. In addition, this approach can be used to realize large and small (much less than 1) indices of refraction and negative permittivity ($\varepsilon < 0$), all while maintaining transparency and without relying on quantum coherence.

Previous work in this field has largely been associated with exploiting quantum-optical effects in a single carefully chosen atomic species. In many cases the complexities of this implementation has prevented further application of these effects. Additionally, the strong association with quantum-coherence has suggested that these optical effects are somehow achievable only using multi-level atomic interactions. Finally, the lack of robustness of these methods has meant that, while these effects may be interesting, they are of little practical utility to robust, real-world devices.

All of the interesting optical effects mentioned above can be produced using a simple mixture of materials composed of population-inverted ("active") and conventional ("passive") resonances. By using the fact that an incoherent mixture of materials with different optical properties exhibits an optical characteristic that is a superposition of the characteristics of its components, we propose materials that exhibit a number of optical effects, e.g., large refractive index or a large change in index with respect to frequency, without absorption or amplification. Additionally, this approach is independent of the underlying physical origin of the resonances in the system, so may be applied in a variety of atomic, optical, and nonlinear optical systems.

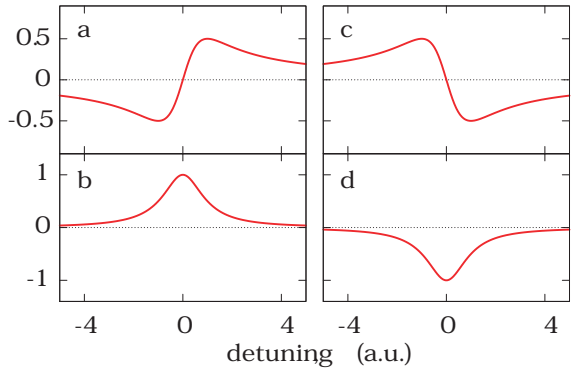

▲ Figure 1: Plot of real (χ') and imaginary (χ'') components of susceptibility as a function of detuning frequency, Δ for active and passive resonances. Plots (a) and (b) are spectra for a passive resonance, while (c) and (d) show an active resonance.

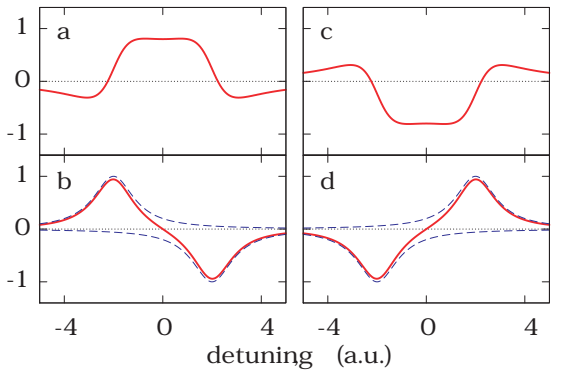

▲ Figure 2: Plot of real (χ') and imaginary (χ'') components of susceptibility as a function of detuning frequency for mixtures of active and passive resonances shown in Figure 1. Plots (a) and (b) depict a material with an equal mixture of passive and active resonances chosen so that one gets a positive χ', zero $d\chi'/d\omega$, accompanied with transparency ($\chi''=0$). Plots (c) and (d) depict a material where $\chi' < 0$ and $d\chi'/d\omega = 0$ at the transparency point. The dashed lines in (b) and (d) show χ'' for the constituent active and passive resonances.

REFERENCES

[1] M. Fleischhauer, A. Imamoglu, and J.P. Marangos, "Electromagnetically induced transparency," *Rev. Mod. Phys.*, vol. 77, no. 2, pp. 633-673, 2005.

[2] L.V. Hau, Z. Dutton, C.H. Behroozi, and S.E. Harris, "Light speed reduction to 17 meters per second in an ultracold atomic gas," *Nature*, vol. 397, no. 6720, p. 594, Feb. 1999.

[3] L.J. Wang, A. Kuzmich, and A. Dogariu, "Gain-assisted superluminal light propagation," *Nature*, vol. 406, no. 6793, p. 277, July 2000.

[4] V. Anant, M. Rådmark, A.F. Abouraddy, T.C. Killian, and K.K. Berggren, "Pumped quantum systems: Immersion fluids of the future?", *J. Vac. Sci. Technol. B*, vol. 23, no. 6, pp. 2662-2667, Nov. 2005.

Increasing Detection Efficiency of Superconducting Nanowire Single-photon Detectors

K.M. Rosfjord, J.K.W. Yang, E.A. Dauler, A.J. Kerman, V. Anant, K.K. Berggren
Sponsorship: United States Air Force

Superconducting NbN-nanowire single-photon detectors (SNSPDs) [1] are an enabling technology for high-performance single-photon optical systems. Examples of these systems include ultra-long range communications [2], integrated circuit testing [3] and quantum cryptography [4]. These systems require the detectors to have high detection efficiency and photon-counting rates, and low dark-count rates and jitter. This work has aimed to increase the detection efficiency of SNSPDs.

The SNSPDs are limited in their efficiency of detection due to transmission through and reflection from the device. To combat these losses we integrated optical enhancements in the form of an anti-reflection coating and optical cavity. These enhancements enabled us to achieve a detection efficiency of 57% at 1550 nm wavelength [5]. This detection efficiency contrasts with previously reported detection efficiencies of 17% at 1550 nm wavelength [6]. A schematic cross-section and transmission electron micrograph of the detector integrated with an optical cavity are shown in Figure 1.

The SNSPDs are also limited in their efficiency of detection by the dimensions of the nanowire they employ. We are currently developing a process, utilizing slant evaporation, which will enable us to lower the width of the nanowire and increase the fill factor of the meander. By changing these physical properties of the meander and coupling this process with our now established optical enhancements, we aim to again increase the detection efficiency of these devices.

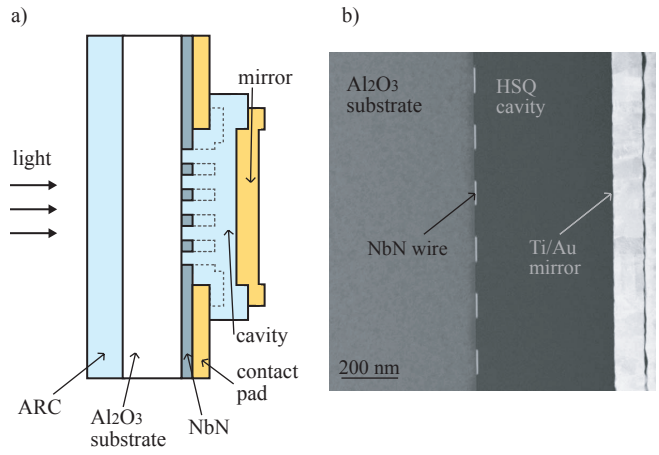

◀ Figure 1: a) Schematic cross-section of photodetector (not to scale) integrated with an optical cavity and anti-reflection coating to reduce loss of photons from reflection and transmission. b) Transmission electron micrograph of cross-section of fabricated device with optical cavity. The cavity shown here was fabricated for calibration purposes and was thicker than those used to increase the detection efficiency.

REFERENCES

[1] G.N. Gol'tsman, O. Okunev, G. Chulkova, A. Lipatov, A. Semenov, K. Smirnov, B. Voronov, A. Dzardanov, C. Williams, and R. Sobolewski, "Picosecond superconducting single-photon optical detector," *App Phys Lett*, vol. 79, no. 6, pp. 705-707, Aug. 2001.

[2] D.M. Boroson, R.S. Bondurant, and J.J. Scozzafava, "Overview of high rate deep space laser communications options," in *Free-Space Laser Communication Technologies XVI, Proc. SPIE* 5338, pp. 37-49, 2004.

[3] S. Somani, S. Kasapi, K. Wilsher, W. Lo, R. Sobolewski, and G. Gol'tsman, "New photon detector for device analysis: Superconducting single-photon detector based on a hot electron effect," *J. of Vacuum Science and Technology B,* vol. 19, no. 6, pp. 2766-2769, Dec. 2001.

[4] C.H. Bennett and G. Brassard, "Quantum cryptography: Public key distribution and coin tossing," in *Proc. IEEE Int. Conf. Computers, Systems and Signal Processing* (Insitute of Electrical and Electronics Engineers, India, 1984) pp. 175–179.

[5] K.M. Rosfjord, J.K.W. Yang, E.A. Dauler, A.J. Kerman, V. Anant, B.M. Voronov, G.N. Gol'tsman, and K.K. Berggren, "Nanowire single-photon detector with an integrated optical cavity and anti-reflection coating," *Optics Express*, vol. 14, no. 2, pp. 527-534, Jan. 2006.

[6] A. Korneev, V. Matvienko, O. Minaeva, I. Milostnaya, I. Rubtsova, G. Chulkova, K. Smirnov, V. Voronov, G. Goltsman, W. Slysz, A. Pearlman, A. Verevkin, and R. Sobolewski, "Quantum efficiency and noise equivalent power of nanostructured, NbN, single-photon detectors in the wavelength range from visible to infrared," *IEEE Transactions on App Superconductivity*, vol. 15, no. 2, pp. 571-574, June 2005.

Enhancing Etch Resistance of Nanostructured Spin-on-Glass Electron Resist via Post-Develop Electron Curing

J.K.W. Yang, V. Anant, K.K. Berggren
Sponsorship: Lincoln Laboratory

Hydrogen silsesquioxane (HSQ) has been used recently as a high-resolution, negative-tone, electron-beam resist[1]. Although HSQ is a good etch mask in chlorine reactive-ion etching (RIE), its poor etch resistance in fluorine RIE makes it undesirable as a mask for etching materials that etch only in fluorine. In this work, we increased the etch-resistance of hydrogen silsesquioxane (HSQ) in CF_4 chemistry via electron-beam curing at high doses. We observed a decrease in the HSQ etch rate by as much as 40% after resist exposure to electron doses of 85 mC/cm^2 (Figure 1). This property of the resist was exploited to fabricate 15-nm-wide superconducting NbN nanowires. We achieved this result by subjecting HSQ to an exposure-develop-exposure step prior to pattern transfer into NbN. The first electron beam exposure defined the nanowires at doses of ~400 μC/cm^2. This step was followed by resist development in Shipley Microposit MF CD-26, resulting in 15-nm-wide HSQ structures. The nanostructures were then re-exposed at 50 mC/cm^2 before RIE to toughen the resist, which would otherwise not survive the etch. Electron exposures were performed at 30-kV acceleration voltage using a Raith 150 electron-beam lithography tool. We demonstrated that the second electron exposure does not decrease the resolution of the nanostructures by comparing images of 15-nm-diameter HSQ nano-pillars before and after re-exposure (Figure 2). This process will enable nanofabrication with thinner resist, therefore avoiding problems such as resist collapse and reduced resolution that are associated with thicker resist layers.

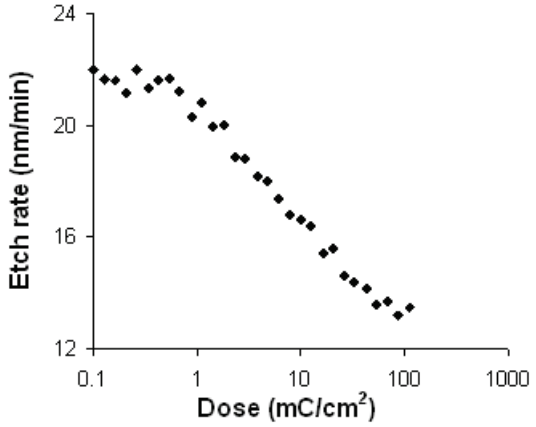

▲ Figure 1: Plot of HSQ etch rate with respect to electron exposure dose. We successfully decreased the etch rate of HSQ by exposing the resist to high doses of electrons. Reactive-ion etch (RIE) conditions were 100-W rf power, 15-V DC self-bias potential, and 15 mT with 15 sccm CF_4.

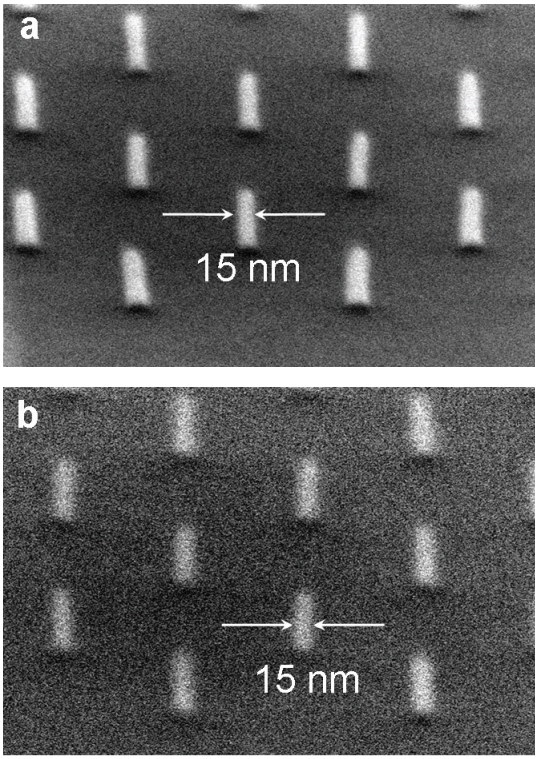

▲ Figure 2: Scanning electron micrograph (SEM) images of HSQ nano-pillars arranged in a hexagonal close-packed structure on Si substrate before (a) and after (b) curing with 50-mC/cm^2 electron dose. There was no observable degradation in the resist shape or dimension due to the second exposure at these dimensions.

REFERENCES

[1] H. Namatsu, Y. Takahashi, K. Yamazaki, T. Yamaguchi, M. Nagase, and K. Kurihara, "Three-dimensional siloxane resist for the formation of nanopatterns with minimum linewidth fluctuations," *J. Vac. Sci. Technol. B*, vol. 16, no. 1, pp. 69-76, Jan. 1998.

Robust Shadow-Mask Evaporation via Lithography-Controlled Undercut

B. Cord, C. Dames, J. Aumentado (NIST), K.K. Berggren
Sponsorship: QuaCGR Fellowship, AFOSR

Suspended shadow-mask evaporation is a simple, robust technique for fabricating Josephson junctions using electron-beam lithography. The basic process entails the fabrication of an undercut structure in a resist bilayer to form a suspended "bridge," followed by two angle evaporations of superconducting material with a brief oxidation step in between, resulting in two overlapping wires separated by a thin oxide layer. Josephson junctions with sub-20-nm diameters are of particular interest in a variety of superconductive devices, including quantum bits. Unfortunately, standard shadow-mask fabrication techniques are unreliable at line widths below 100 nm.

While most previous processes used PMMA for the top (imaging) layer and a PMMA/MAA copolymer for the bottom (support) layer, our process uses a PMMA/PMGI bilayer. This resist system allows the two layers to be developed separately, ensuring that the imaging layer is not biased during development of the undercut and allowing the process to achieve the full resolution of the PMMA layer. Additionally, the extent of the undercut in the support layer can be precisely controlled by defining it lithographically, making it possible to repeatedly fabricate undercut regions as large as 600 nm.

Extensive modeling of both the exposure and development processes was used to verify our results. Using Monte Carlo and mass transfer simulations, we produced a model that closely matches experimental data. With the process fully characterized, it is possible to produce a wide range of line width/undercut combinations. This robustness, combined with the high resolution of PMMA, will allow the reliable fabrication of sub-20-nm Josephson junctions.

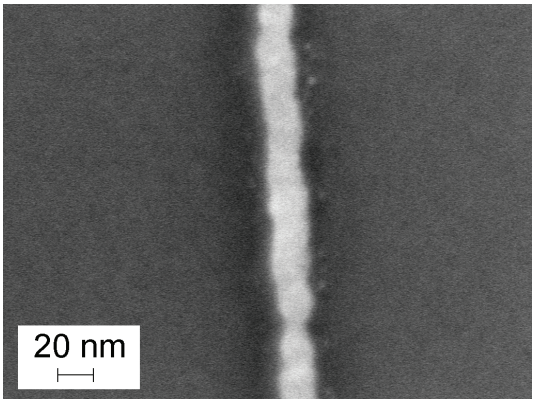

▲ Figure 1: Scanning electron micrograph of a 16-nm-wide, 10-nm-thick evaporated titanium-gold line fabricated using the PMMA/PMGI process.

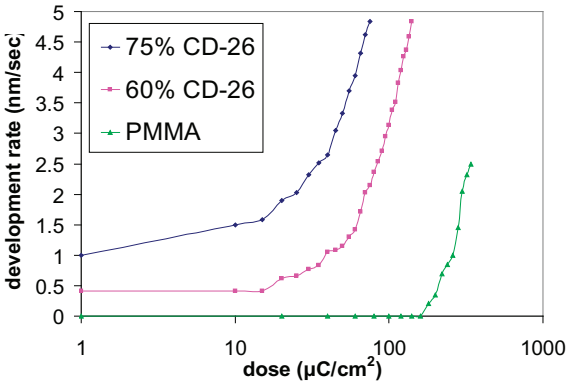

▲ Figure 2: Contrast curve plots for PMGI using two different dilutions of CD-26 developer. Contrast data for PMMA developed in a 3:1 IPA:MIBK solution is shown for reference.

Pattern Generation Using Multi-Step Room-Temperature Nanoimprint Lithography

S. Harrer (Technische Universität München, Munich, Germany), J.K.W. Yang, F. Ilievski, C.A. Ross, K.K. Berggren
Sponsorship: AFOSR, Karl Chang Innovation Fund at MIT

We have demonstrated multi-step room-temperature nanoimprint lithography (RTNIL) using polystyrene (PS, average molecular weight 97 kg/mol) as the polymer layer for imprinting complex patterns. Our motivation in pursuing multi-step RTNIL is to create a new pattern-generation method, able to create complex and arbitrary patterns without requiring a custom template for each new pattern. A variety of different forms of NIL have been demonstrated in the past: thermal NIL [1], UV-cured NIL [2], and room-temperature NIL (RTNIL) [3-6]. All of these existing techniques focus on pattern replication using one, or at most two, imprint steps. In our approach, the extent of each of the starting templates is only a fraction of the extent of the desired final pattern (i.e., each template is much smaller than the final pattern). In separate experiments, single, double, and multiple (up to 10) sequential imprint steps were performed at imprint pressures between 3 to 30 MPa. To accomplish this demonstration, we designed and built a tool that controllably and repeatedly translated and pressed a sample into a stationary mold. The demonstrated inter-step alignment accuracy of this tool was ~ 500 nm. To illustrate this capability, we imprinted the letters "MIT" by using ten sequential imprint steps, translating the sample a programmable distance along a single direction in between steps (Figure 1). The molds used in these experiments consisted of rectangular structures of varying aspect ratios, ranging from 150 to 300 nm wide. Before this technique can be used as it is ultimately intended, as a method for the generation of complex patterns across a wide variety of length scales using only a simple set of generic template structures, the imprint polymer distortion and deformation must be minimized and inter-step alignment must be optimized. However, the work suggests that RTNIL may be a useful pattern-generation tool. This development can be thought of as analogous to the development of the typewriter after the printing press. While a printing press can replicate large-scale molds (entire pages of books) at high rates, in the typewriter, the smallest mold unit was a single letter. The typewriter sacrificed throughput in return for flexibility and low cost. Similarly, by removing the difficult and slow step of custom-template manufacturing from the process, our work represents a shift in the way some nanoimprint work might be performed in the future.

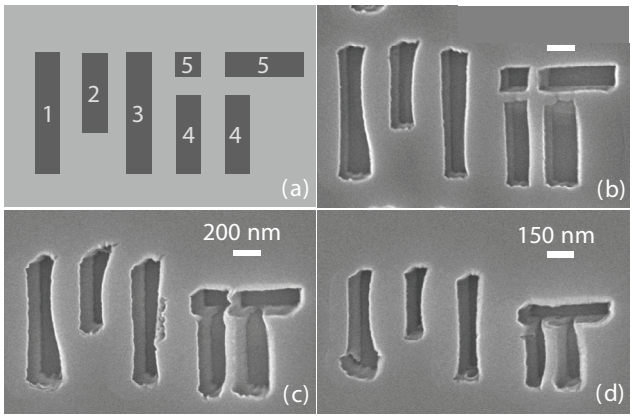

◀ Figure 1: Results of a 10-step RTNIL imprint cycle for different mold dimensions: (a) graphical representation of desired final pattern to be printed out. The numbers indicate the order in which parts of the final pattern are imprinted. After the 5th imprint step the pattern is complete; steps 6-10 create further identical patterns, yielding a total number of 6 completed patterns after the 10th imprint step. We performed several 10-step RTNIL cycles using molds with different feature sizes: The linewidth of the imprinted pattern in (b) is 300nm, the linewidth in (c) is 200 nm, and (d) shows an imprint result for a pattern composing a linewidth of 150 nm. The observed vertical and horizontal misalignment was ~ 500 nm.

REFERENCES

[1] S.Y. Chou, P.R. Krauss, and P.J. Renstrom, "Imprint lithography with 25-nanometer resolution," *Science*, vol. 272, no. 5258, pp. 85-87, 1996.

[2] M. Colburn, S. Johnson, M. Stewart, S. Damle, T. Bailey, B. Choi, M. Wedlake, T. Michaelson, S.V. Sreenivasan, J. Ekerdt, and C.G. Willson, Step-and-flash imprint lithography: a new approach to high-resolution patterning," *SPIE Conf. on Emerging Lithographic Technologies III*, vol. 3676, pp. 379-389, 1999.

[3] D.-Y. Khang, H. Yoon, and H.H. Lee, "Room-temperature imprint lithography," *Adv. Mater.*, vol. 13, no. 10, pp. 749-752, 2001.

[4] D. Pisignano, L. Persano, P. Visconti, R. Cingolani, G. Gigli, G. Barbarella, and L. Favaretto, "Oligomer-based organic distributed feedback lasers by room-temperature nanoimprint lithography," *Appl. Phys. Lett.*, vol. 83, no. 13, pp. 2545-2547, 2003.

[5] E. Mele, D. Pisignano, M. Mazzeo, L. Persano, and G. Gigli, "Room-temperature nanoimprinting on metallo-organic complexes," *J. Vac.Sci. Technol. B*, vol. 22, no. 3, pp. 981-984, 2004.

[6] E. Mele, F. Di Benedetto, L. Persano, R. Cingolani, and D. Pisignano, "Multilevel, room-temperature nanoimprint lithography for conjugated polymer-based photonics," *Nano Letts*, vol. 5, no. 10,pp. 1915-1919, 2005.

Modeling of Electrical and Thermal Response of Superconducting Nanowire Single Photon Detectors (SNSPD)

J.K. Yang, K.K. Berggren
Sponsorship: Lincoln Laboratory

The response time of superconducting nanowire single-photon detectors (SNSPD) is in the order of several nanoseconds [1-2]. This detector works by the formation of a photon-induced resistive barrier across a superconducting nanowire that is biased close to its critical current. Detected photons result in measurable voltage pulses with very fast rise times and a slower decay. We modeled the full electrical and thermal response of a NbN SNSPD to the absorption of a single photon. The thermal response was modeled by a one-dimensional, time-dependent heat equation incorporating power dissipated by Joule heating in the resistive segment of the wire and heat conduction along the wire and into a sapphire substrate. The electrical model consists of the SNSPD, modeled as an inductor in series with a time-varying resistor shunted by a 50 ohm transmission line and a current bias. This model predicts the growth of the normal region leading to the increase in the total electrical resistance with time as more of the wire heats up and switches into the normal state as shown in Figure 1. However, the resistance does not build up indefinitely since the current flowing through the wire drops as it is diverted into the transmission line once resistance develops in the wire as shown in Figure 2. The model will also enable us to predict performances of devices made of different materials.

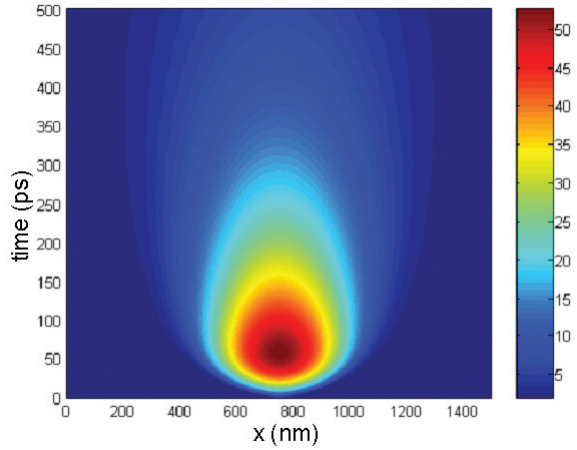

▲ Figure 1: Plot of simulation data showing the temperature evolution in a short segment (1.5 μm) of a longer nanowire (with a total kinetic inductance of 200 nH) after a photon-induced resistive barrier forms across the nanowire at t = 0, x = 750 nm. Temperature information is depicted in the color with a corresponding color-map shown on the right in units of Kelvin. The temperature increases quickly and reaches a maximum at about ~50 ps after photon absorption.

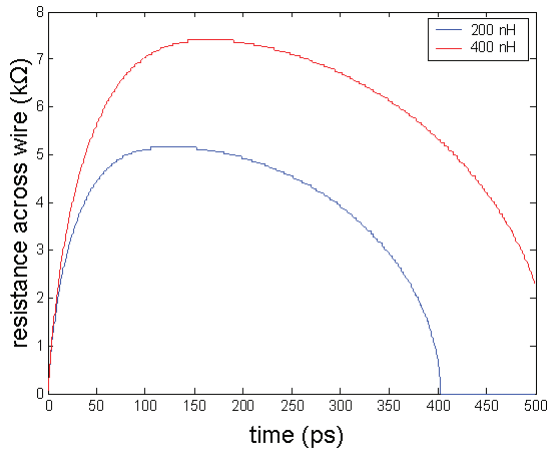

▲ Figure 2: Plot of simulation data showing the total resistance built up across a superconducting nanowire after the formation of a resistive barrier for wires of different total kinetic inductances.

REFERENCES:

[1] A.J. Kerman, E.A. Dauler, W.E. Keicher, J.K.W. Yang, K.K. Berggren, G. Gol'tsman, and B. Voronov, "Kinetic-inductance-limited reset time of superconducting nanowire photon counters," *Appl. Phys. Lett.*, vol. 88, pp. 111116-111119, 2006.

[2] K.M. Rosfjord, J.K.W. Yang, E.A. Dauler, A.J. Kerman, V. Anant, B.M. Voronov, G.N. Gol'tsman, and K.K. Berggren, "Nanowire Single-photon detector with an integrated optical cavity and anti- reflection coating," *Optics Express*, vol. 14, pp. 527-534, 2006.

Quantum Dot Photodetectors Deposited via Microcontact Printing

A.C. Arango, D.C. Oertel, M.G. Bawendi, V. Bulović
Sponsorship: ISN

Solution processable colloidal quantum dot systems exhibit many of the special optical and electronic properties associated with epitaxially grown quantum confined systems. Their tunable band gap and higher absorption relative to the bulk make quantum dots particularly attractive as photogeneration materials. At the same time, colloidal quantum dots offer greater material system flexibility than epitaxial quantum dots because deposition on any substrate is possible. The prevailing deposition method, however, is spin casting [1], which introduces limitations such as solvent incompatibility with underlying films and the inability to pattern side-by-side pixels for multispectral photodetector arrays. We employ a non-destructive microcontact printing method that allows for deposition of a thin (20 nm) quantum dot film onto a wide band gap organic hole transport layer, N,N'-bis-(3-methylphenyl)-N,N'-bis-(phenyl)-benzidine (TPD), thus producing an inorganic/organic heterojunction which serves to enhance charge separation in the device. The use of ITO electrodes provides the top and bottom contacts, allowing for near-transparency.

Current-voltage characteristics show low dark currents in reverse bias and good rectification. Excitation of the quantum dots yields a strong, saturated photoresponse; open circuit voltages of +0.5V; and a fill factor of 0.4. Measurement of the locked-in photocurrent under bias reveals a strong photocurrent signal extending out to +1.4V (Figure 2), in excess of the built-in acceptor-donor energy level offset of approximately 0.8V. We attribute the photocurrent voltage dependence to efficient charge extraction and low recombination rates at the heterojunction and top ITO contact. Changing the size and material properties of the quantum dots can tune the response spectrum of the device across the visible and near infrared spectrum. The present focus is on improving the device performance and optimizing the photodetection response in the 1 μm to 2 μm wavelength region by using different quantum dot film chemistries.

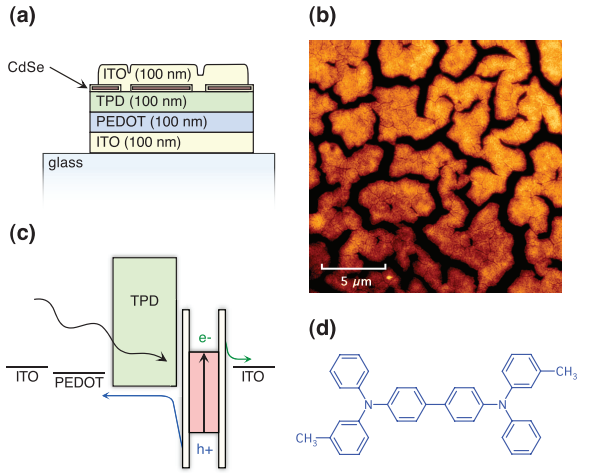

▲ Figure 1: Schematic of photodetector device structure (a). An AFM of the surface of the printed quantum-dot film demonstrates that the film is not continuous (b). The energy band diagram (c) illustrates the photogeneration process. The molecular structure of the hole- transport material, TPD, is shown in (d).

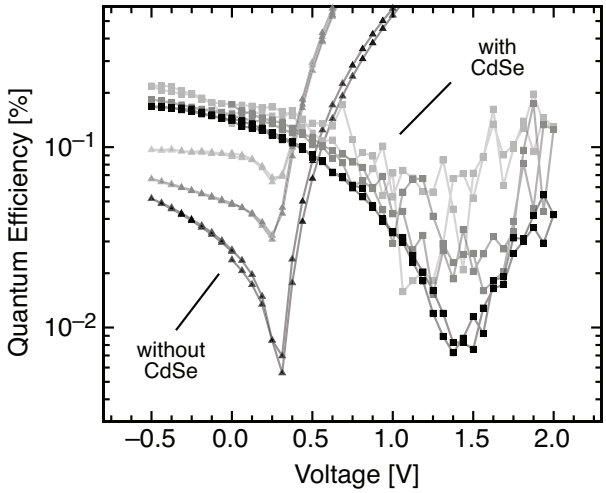

▲ Figure 2: Plot of the quantum efficiency versus applied bias for the photodetector and a control device without quantum dots. The CdSe device is measured with a 532-nm laser at 2, 20 and 200 uW/cm2 (light grey, grey, and black squares, respectively). The TPD control device is measured at 408 nm at 2, 20 and 200 uW/cm2 (light grey, grey, and black triangles, respectively).

REFERENCES:

[1] D.C. Oertel, M.G. Bawendi, A.C. Arango, and V. Bulovic. "Photodetectors based on treated CdSe quantum-dot films," *Appl. Phys. Lett.*, vol. 87, no. 21, pp. 213505:1-3, Nov. 2005.

Microcontact Printing of J-Aggregate Thin Films for Photonic Devices

M.S. Bradley, J.R. Tischler, V. Bulović
Sponsorship: DARPA, NDSEG, MIT NSF MRSEC

Thin-film J-aggregates of cyanine dyes enable the observation of strong coupling between light and matter at room temperature, potentially allowing for the development of an entirely new class of optoelectronic devices [1]. Previously, J-aggregate deposition methods have required the exposure of a device in fabrication to the solvents of a J-aggregate solution that can potentially damage other optically or electrically active materials and restrict the steps involved in fabricating devices. In this work, we demonstrate a new stamping technique for depositing J-aggregate thin films that decouples the formation of J-aggregates from the placement of J-aggregate thin films into device structures.

Combining research in polyelectrolyte layer-by-layer deposition of J-aggregates [2] with stamping of polyelectrolyte thin films, we show how to form thin films of J-aggregates on a stamp and then stamp those films into device structures [3]. We show the optical and morphological properties of stamped J-aggregate films and calculate the optical constants of the films (Figure 1), which we use to determine the density of J-aggregated dye molecules in the final thin film. Additionally, we investigate device structures enabled by stamping of J-aggregate thin films, including J-aggregate organic light-emitting devices and patterned J-aggregate devices made via stamp pattern transfer (Figure 2). Lastly, we explore the extension of J-aggregate thin-film stamping to other methods of depositing J-aggregate thin films, including Langmuir-Blodgett-type deposition methods.

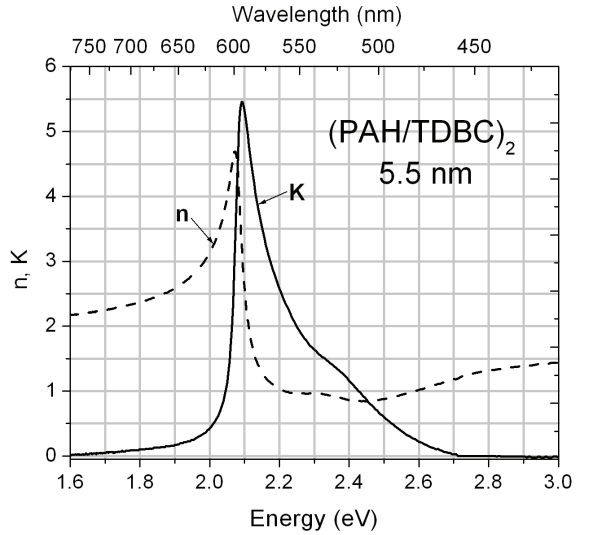

▲ Figure 1: Complex index of refraction of PAH (polyallylamine hydrochloride)/TDBC (J-aggregating cyanine dye) film formed on a PDMS (polydimethylsiloxane) stamp and deposited on glass using microcontact printing, calculated from reflectance measurements using Kramers-Kronig regression and a thin film dielectric model. The peak extinction coefficient corresponds to an absorption constant of 1.2 x 10^6 cm^{-1}.

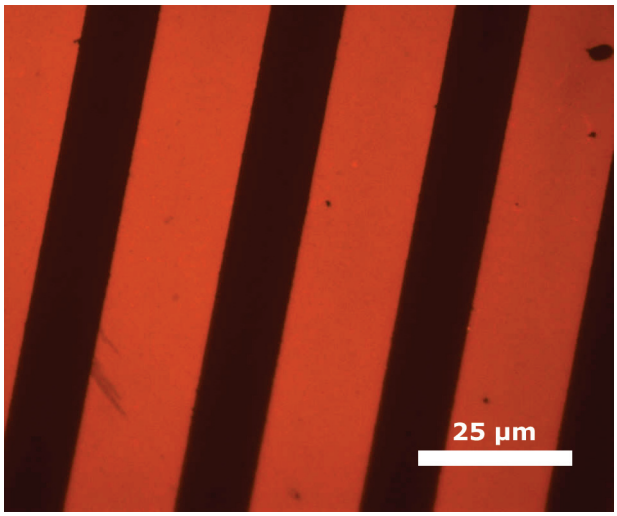

▲ Figure 2: Photoluminescence of patterned PAH/TDBC film using green light excitation. Patterned PDMS stamps were made by curing PDMS on a silicon mold. The J-aggregate thin films were grown on patterned PDMS stamps, and in the microcontact printing process only the raised portions of the film were transferred to the glass substrate.

REFERENCES

[1] J.R. Tischler, M.S. Bradley, V. Bulović, J.H. Song, and A. Nurmikko, "Strong coupling in a microcavity LED," *Phys. Rev. Lett.*, vol. 95, no. 3, pp. 036401-036404, 2005.

[2] M.S. Bradley, J.R. Tischler, and V. Bulović, "Layer-by-layer J-aggregate fhin films with a peak absorption constant of 10^6 cm^{-1}," *Advanced Materials*, vol. 17, no. 15, pp. 1881-1886, 2005.

[3] M.S. Bradley, J.R. Tischler, S.K. LaiHing, and V. Bulović, "Deposition of J-aggregate thin films via stamping for use in optoelectronic devices," presented at the *Materials Research Society Fall Meeting*, 2005.

Measuring Thermal and Thermoelectric Properties of Single Nanowires and Carbon Nanotubes

C. Dames, C.T. Harris, A. Muto, G. Chen (in coll. with M.S. Dresselhaus, MIT, Z.F. Ren, Boston College)
Sponsorship: JPL, NSF

Knowledge of nanowire and carbon nanotube thermal and thermoelectric properties will be important for the thermal management of nanoscale devices that have recently been demonstrated (optoelectronic, sensing, and computing) and essential for the design of nanostructured thermoelectric materials. For nanowire diameters smaller than the bulk mean-free path of heat carriers (electrons and/or phonons), theory predicts that the thermal conductivity of these structures will be reduced when compared to similar bulk materials [1]. In order to experimentally verify these predictions, we are exploring several systems to measure the properties of single nanowires and carbon nanotubes.

Current work includes a basic platform to measure the thermal conductivity and specific heat of electrically conductive nanowires, such as the silicon nanowire shown below. Electron-beam lithography was used to pattern the leads of a four-point probe aligned to the ends of the nanowire. Joule heating of a suspended nanowire with thermally clamped ends results in a temperature rise of the nanowire due to its finite thermal resistance. This temperature rise can be measured by resistance thermometry (again using the nanowire) and used to calculate its thermal conductivity and specific heat. This technique is being adapted for an *in situ* TEM measurement, to enable high-throughput physical property measurements of many nanowires of various geometries and morphologies, and allow correlations with their atomic structure as determined by TEM.

Microfabricated metal lines can also be employed to measure electrically insulating nanowires. Using electron beam lithography, a metal heater line is fabricated such that a target nanowire crosses the center of the line. With the ends of the nanowire and heater thermally anchored, the nanowire removes a fraction of heat from the heater line, reducing the heater's temperature rise, and thus making it possible to calculate the thermal resistance of the nanowire.

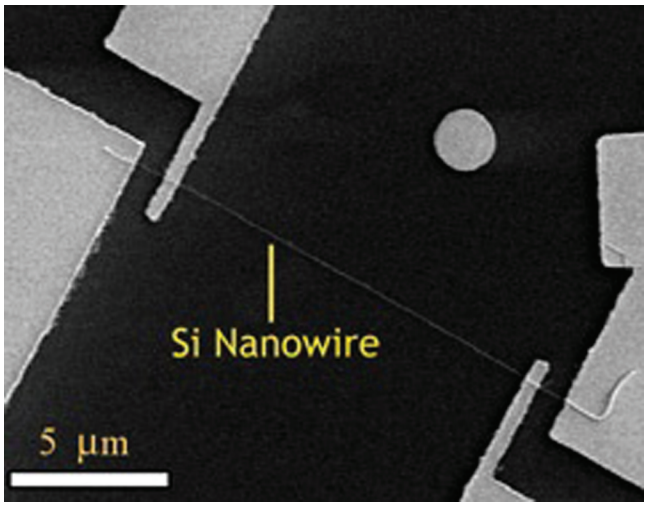

▲ Figure 1: Contacts for a four-point probe measurement of a single silicon nanowire.

REFERENCES

[1] G. Chen, *Nanoscale Energy Transport and Conversion: A Parallel Treatment of Electrons, Molecules, Phonons, and Photons*, New York: Oxford University Press USA, 2005.

Nanocomposites as Thermoelectric Materials

H. Lee, Q. Hao, M. Tang, M.S. Dresselhaus, G. Chen (in coll. with Z.F. Ren, Boston College, J.-P. Fluerial, JPL, P. Gogna, JPL)
Sponsorship: NASA, Intel, Nanolab SBIR

Direct energy conversion between thermal and electrical energy based on thermoelectric effects is attractive for potential applications in waste heat recovery and environmentally-friendly refrigeration [1-2]. The energy conversion efficiency depends on the dimensionless figure of merit of the thermoelectric materials, ZT, which is proportional to electrical conductivity, square of the Seebeck coefficient, inverse of the thermal conductivity, and absolute temperature. At the current stage, the low ZT values of available materials restrict the efficient applications of this technology. Recently, significant enhancements in ZT were presented through the use of nanostructures such as superlattices. Previous works done by our group show that such improvement in superlattices is mainly attributed to the increased interfacial diffuse phonon scattering [3-4]. These studies lead us to pursuing the nanocomposite approach as a cost-effective alternative in developing high ZT materials.

Previously, we reported thermal conductivity reduction in SiGe nanocomposites. Through collaboration with Boston College group and Jet Propulsion Lab, we realized significant improvement in the ZT over that of SiGe used in the past NASA flights (Figure 1). We are also working on Bi_2Te_3 and PbTe nanocomposites. Our preliminary results on Bi_2Te_3 nanocomposites also show reduced thermal conductivities. Work is in progress to optimize the structures for further improving the ZT values.

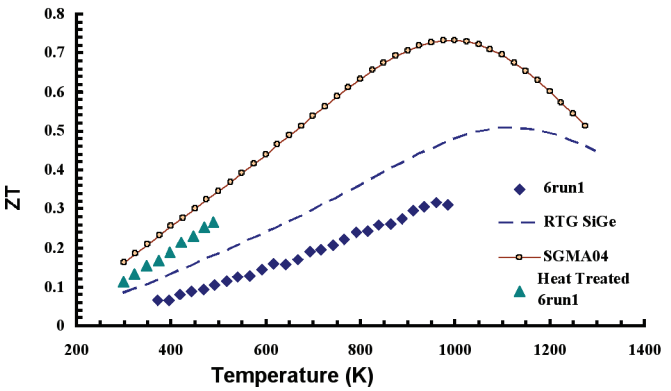

▲ Figure 1: Measurements of temperature-dependent ZT. Nanostructured sample SGMA04 shows higher ZT than typical bulk alloy, "RTG SiGe."

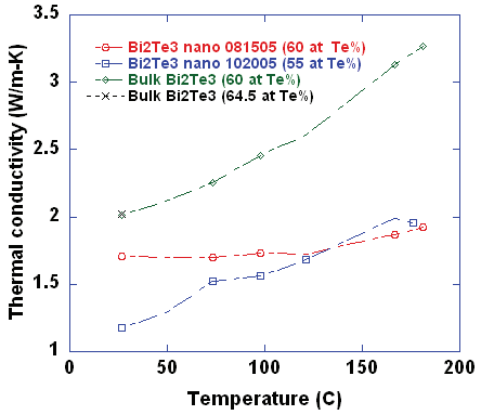

▲ Figure 2: Temperature-dependent thermal conductivities of Bi_2Te_3 nanocomposite samples. Data of bulk materials are plotted for comparison.

REFERENCES

[1] G.S. Nolas, J. Sharp, and H.J. Goldsmid, *Thermoelectrics: Basic Principles and New Materials Developments*. New York: Springer-Verlag Berlin Heidelburg, 2001.

[2] D.M. Rowe, Ed., *CRC Handbook of Thermoelectrics*. Boca Raton, FL: CRC Press LLC, 1995.

[3] G. Chen, "Thermal conductivity and ballistic-phonon transport in the cross-plane direction of superlattices," *Phys. Rev. B*, vol. 57, no. 23 pp. 14958-14973, June 1998.

[4] G. Chen, M.S. Dresselhaus, G. Dresselhaus, J.-P. Fleurial and T. Caillat, "Recent developments in thermoelectric materials," *International Materials Reviews*, vol. 48, no. 1, pp. 45-62, Feb. 2003.

Flux and Force due to Near-field Thermal Radiation

D. Chen, L. Hu, A. Narayanaswamy, G. Chen (in coll. with J.D. Joannopoulos)
Sponsorship: ONR, MURI (through UC Berkeley)

Fluctuating electromagnetic fields of thermal origin lead to surprising results in the near-field. For instance, the radiative energy transfer between bodies that can support surface polaritons can be increased by a few orders of magnitude compared to far-field thermal radiation predicted by Planck's law. These fluctuating fields, even at absolute zero temperature, also lead to the Casimir force between objects. We have previously shown that the enhancement in radiative transfer can be used to improve the performance of thermophotovoltaic (TPV) [1] as well as thermoelectric devices [2].

Surface polaritons, which are involved in enhancing out-of-plane radiative transfer, can also lead to significant increase in in-plane thermal "conductivity." We model the in-plane energy transfer due to these surface polaritons as a diffusive process in an absorbing medium. Due to the well-known very long propagation length of the anti-symmetric mode, we find that the surface polaritons can make a significant contribution to the effective thermal conductivity along thin films. In particular, for a 40 nm thick film of amorphous silicon dioxide, we calculate a total thermal conductivity of 4 W m^{-1} K^{-1} at 500 K, which is an increase of ~100% over the intrinsic phonon thermal conductivity [3], as shown in Figure 1. In addition to thermal in-plane transport, we are in the process of measuring near-field thermal radiation transfer and forces between two spherical micro-particles as well as between spheres and planar substrates.

We are developing a 2-D structure that features micro-sized interdigitized hot and cold fingers, as shown in Figure 2. The objective is to increase both power density and efficiency of TPV devices by exploiting the increased radiative surface/volume ratio, photon recycling, and photonic band gap in one compact device structure. We have fabricated the finger structures and successfully aligned the two mating structures. Thermal characterization of the device is in progress.

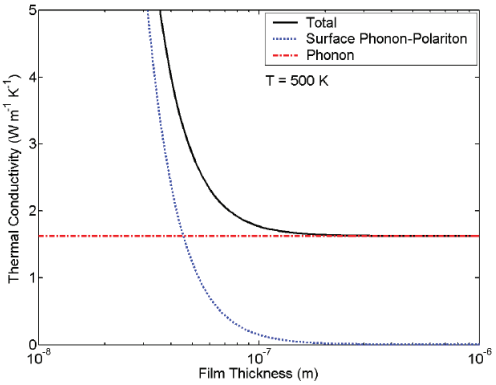

▲ Figure 1: Amorphous silicon dioxide (glass) thermal conductivity due to phonons and surface phonon polaritons as a function of film thickness at 500 K.

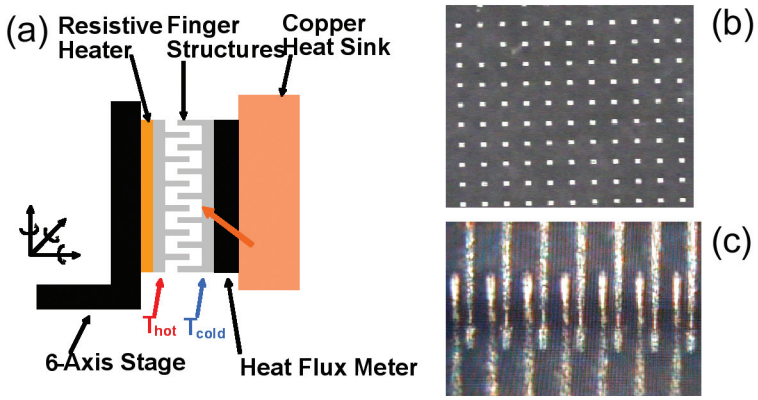

▲ Figure 2: (a) Illustration of the testing rig for the interdigitized thermophotovoltaic device structure. (b) Top-view of one set of the finger structures. (c) Aligned finger structures.

REFERENCES

[1] A. Narayanaswamy and G. Chen, "Surface modes for near-field thermophotovoltaics," *Appl. Phys. Lett.*, vol. 82, no. 20, pp. 3544-3546, May 2003.

[2] R. Yang, A. Narayanaswamy, and G. Chen, "Surface plasmon coupled nonequilibrium thermoelectric refrigerators and power generators," *J. of Computational and Theoretical Nanoscience*, vol. 2, no. 1, pp. 75-87, Mar. 2005.

[3] D.-Z. Chen, A. Narayanaswamy, and G. Chen, "Surface phonon-polariton mediated thermal conductivity enhancement of amorphous thin films," *Phys. Rev. B*, vol. 72, no. 15, p. 155435:1-4, Oct. 2005.

CNT Assembly by Nanopelleting

S.D. Gouda, S. Kim, S.-G. Kim
Sponsorship: Intelligent Microsystems Center

We have developed a novel method of manufacturing and assembling process termed nano-pelleting [1-2], which refers to large-scale handling and long-range order assembly of individual carbon nanotubes (CNTs). The nano-pelleting concept overcomes the limitation of very small-scale order by embedding carbon nanotubes into micro-scale pellets. This technique includes vertically growing single strand CNTs, embedding a CNT into a polymeric pellet, separating a pellet, and transplanting a CNT. The CNTs are grown vertically, both individually and in bunches, on the patterned catalytic metal using a plasma enhanced chemical vapor deposition (PECVD) machine (Figure 1) built by us at MIT. The machine's key feature is the control of the substrate temperature during the growth process. At the bottom of the ceramic heater, three thermocouples are connected to measure the temperature, which is controlled by the heater controller. Plasma is formed between anode and cathode by applying a DC voltage, which then decomposes acetylene into carbon that deposits below the Ni catalyst and leads to the formation of carbon nanotubes. The process sequence to make pellets is the following: coating PMMA on the silicon wafer, exposing the photo-resists using Raith 150 to obtain the desired patterns by varying the aperture size, dose, electric field, developing the photo-resist, depositing Ti/Ni (25nm), and lifting-off the resist to obtain Ni-catalyst nano-dots. Single stranded CNTs are grown in the PECVD machine with optimized process conditions as shown in Figure 2. On these isolated CNTs, SU-8 is spin-coated to form a thickness of 25 micro-meter. This SU-8 layer is exposed to UV light using an appropriate mask and then developed to form nano-pellets. The nano-pellets are released from the silicon substrate by manually breaking them with a spark needle. We are developing an in-plane AFM probe [3] with mechanically assembled CNT tips.

▲ Figure 1: The PECVD machine for growing CNTs at MIT.

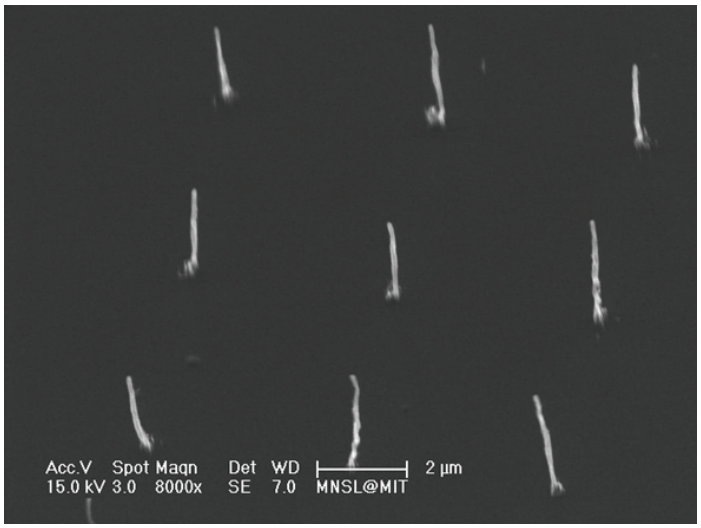

▲ Figure 2: Single strand CNTs grown by the PECVD machine.

REFERENCES

[1] T. El-Aguizy and S.-G. Kim, "Large-scale assembly of carbon nanotubes," in *Proc. of ASME Integrated Nanosystems Conf: Design, Synthesis & Applications*, Pasadena, California, 2004.

[2] T. El-Aguizy, J.-H. Jeong, Y.B. Jeon, W.Z. Li, Z.F. Ren, and S.-G. Kim, "Transplanting carbon nanotubes," *App. Phys. Lett.*, vol. 85, no. 25, pp. 5995-5997, Dec. 2004.

[3] C. Mueller-Falcke, S.D. Gouda, S. Kim, and S.-G. Kim, "A nano-scanning platform for bio-engineering: an in-plane probe with switchable stiffness," *Nanotechnology,* vol. 17, no. 4, pp. S69–S76, Feb. 2006.

Integrated Carbon Nanotube Sensors

K.-J. Lee, T.S. Cho, A.P. Chandrakasan, J. Kong
Sponsorship: Intel, MARCO IFC

Single-walled carbon nanotubes (SWNT) exhibit unique mechanical and electrical properties that make them attractive for nanoelectronic applications. In particular, the conductance of a semiconducting SWNT is known to change significantly when exposed to certain gases [1]. The high sensitivity and fast response time make carbon nanotubes (CNT) very attractive for chemical sensing applications. However, the underlying sensing mechanism of CNT sensors is quite different from Si-based chemical transistors, and fabrication methods generally yield devices with large variations. Device variations and technology integration issues must be resolved before any CNT sensor devices can become practical [2].

In this project, we grow carbon nanotubes through chemical vapor deposition (CVD) and fabricate devices for an ultra low-power wireless sensing system. This work is done in collaboration with T. S. Cho in Professor A. Chandrakasan's group from the Department of Electrical Engineering and Computer Science at MIT, whose back-end circuitry will provide an interface to our CNT sensor array. The main goals of this project are to build a CNT sensor array with high yield of semiconducting SWNTs, high sensitivity and selectivity of gases, and low variability in the performance of the device. Through statistical characterization of the device, we attempt to get a better grasp of the underlying CNT sensing mechanism and find enhanced fabrication methods to reduce performance variability. In addition, chemical functionalization of CNT sensors will allow the target application to detect different types of toxic gases for environmental and industrial applications.

REFERENCES

[1] J. Kong, N.R. Franklin, C. Zhou, M.G. Chapline, S. Peng, K.J. Cho, and H. Dai, "Nanotube molecular wires as chemical sensors," *Science*, vol. 287, pp. 622-625, Jan. 2000.

[2] Y.C. Tseng, P. Xuan, A. Javey, R. Malloy, Q. Wang, J. Bojor, and H. Dai, "Monolithic integration of carbon nanotube devices with silicon MOS technology," *Nano Lett.*, vol. 4, no. 1, pp. 123-127, Dec. 2004.

[3] P. Qi, O. Vermesh, M. Grecu, A. Javey, Q. Wang, H. Dai, S. Pend, and K.J. Cho, "Toward large arrays of multiplex functionalized carbon nanotube sensors for highly sensitive and selective molecular detection," *Nano Lett.*, vol. 3, no. 3, pp. 347-351, Feb. 2003.

Templated Assembly by Selective Removal

S. Jung, F. Eid, C. Livermore
Sponsorship: NSF, 3M Corporation

In this project, an effective technique for site-selective, multicomponent assembly at the nano- and micro-scale has been created and quantitatively modeled. This approach offers great promise for assembling arbitrary (not necessarily periodic) systems of multiple different types of nanoscale components, such as electronics (memory, logic, interconnects, displays) and sensor systems.

The key elements of the approach follow. First, the topography of the substrate is modified to match the components' 3D shapes. Then the substrate and components are coated with an adhesion promoter, such as a hydrophobic SAM for adhesion in a water-based environment. The components and substrate are placed in a fluid environment for the assembly process, and megahertz frequency ultrasound is applied to the fluid bath. Components contact the substrate randomly and adhere wherever they land; however, components that are not in shape-matched sites are removed by fluid forces initiated by the high frequency ultrasound. Components in shape-matched sites are selectively retained because their adhesive force is stronger than the removal forces. Figure 1 is an optical micrograph showing the successful assembly of 600 nm and 2 μm diameter silica microspheres into designated sites on the substrate. Figure 2 shows how measured assembly yield of spheres into holes of slightly different sizes increases with the contact area between spheres and substrate.

This approach to assembly is inherently selective; since each component will adhere only in a shape- and size-matched site, geometrically distinct components will assemble only into their designated assembly sites. This allows the organizing information to be stored in the template initially, and permits components that may not be compatible with top-down manufacturing techniques to be added to the system later, with high positional precision. Work is underway to demonstrate this approach at smaller size scales and to create practical systems using this technology.

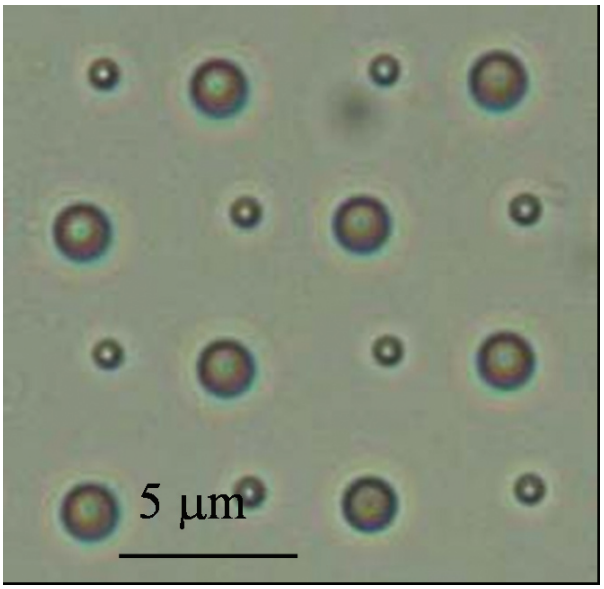

▲ Figure 1: Optical micrograph of 600 nm and 2 μm spheres assembled into designated sites on a surfaces.

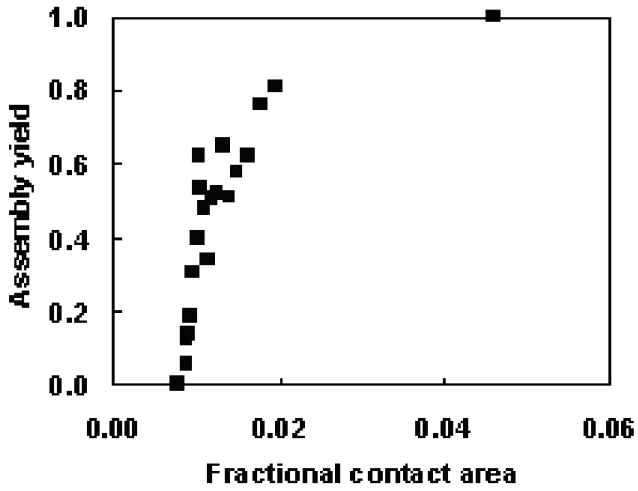

▲ Figure 2: Plot of assembly yield (number of filled holes/total number of holes) vs. contact area between sphere and hole. Assembly yield increases from 0% to 100% as quality of the shape match improves.

Vibrational, Thermodynamic, and Transport Properties of Carbon Nanotubes from Density-functional Perturbation Theory

N. Bonini, N. Marzari
Sponsorship: MARCO IFC, ISN

Carbon nanotubes present unique physical properties, which make them promising materials for applications in high-performance nanoscale devices. Indeed, because of their high thermal and electrical conductivities, carbon nanotubes are excellent candidates both as interconnects in integrated circuits and as heat-management materials in silicon chips. Unfortunately, due to the challenge in nanoscale experiments, the thermodynamics of these materials as well as the origin and the limits of their transport properties are still unclear. In this project we use a combination of density-functional theory and density-functional perturbation theory to study the vibrational properties of carbon nanotubes. In particular we investigate anharmonic effects, such as thermal expansion and phonon lifetimes, which are key quantities to understanding the thermodynamical and transport properties of these systems. The thermal expansion coefficients are calculated from the minimization of the vibrational free energy in the quasi-harmonic approximation. This same approach provides excellent agreement with experimental data for the case, e.g., of graphite. Our results show that carbon nanotubes contract both in the axial and radial directions at low and room temperature, while they expand at higher temperatures. Anharmonic phonon lifetimes are evaluated from the cubic terms in the interatomic potential, using density-functional perturbation theory and the 2n+1 theorem. We plan to use these quantities to predict the transport properties of carbon nanotubes using the Boltzmann transport equation– in particular how inelastic excitation of phonons further reduces the ballistic transport of electrons.

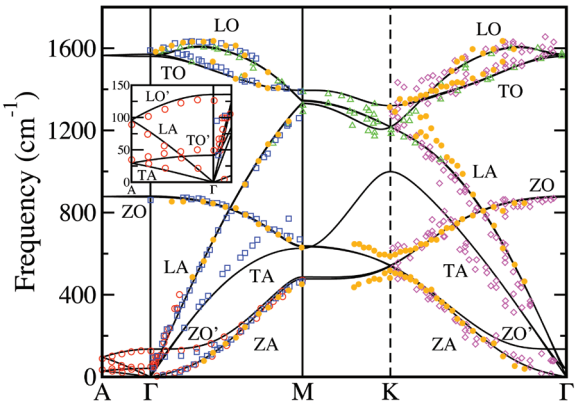

▲ Figure 1: The *ab initio* phonon dispersion of graphite (solid lines). The inset shows an enlargement of the low-frequency Γ-A region. The experimental data are also shown (color marks).

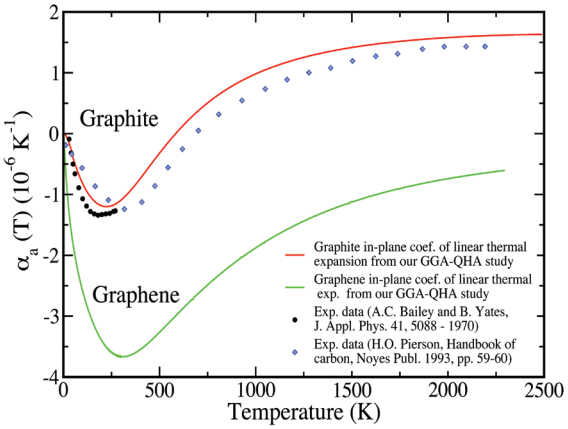

▲ Figure 2: In-plane coefficient of thermal expansion as a function of temperature for graphite and graphene.

Static Dielectric Response of Single-wall and Multi-wall Carbon Nanotubes from First-principles

B. Kozinsky, N. Marzari
Sponsorship: MARCO IFC, NSF

We characterize the response of isolated single-wall (SWNT) and multi-wall (MWNT) carbon nanotubes and bundles to static electric fields using first-principles calculations and density-functional theory. The longitudinal polarizability of semiconducting SWNTs scales as the inverse square of the band gap (Figure 1). Because of the absence of depolarization effects in the longitudinal direction, nearby parallel tubes have very weak dielectric interaction, so in MWNTs and bundles the longitudinal polarizability is given by the sum of polarizabilities of the constituent tubes.

The transverse polarizability of SWNTs is insensitive to band gaps and chiralities and is proportional to the square of the radius (Figure 2). The electric field applied perpendicular to a SWNT is screened by a universal factor of about 4.5, independent of the nanotube's radius. This property is inherited from the anomalous scale-invariant in-plane response of a sheet of graphene. The transverse response is thus intermediate between metallic and insulating. We construct a simple electrostatic model based on a scale-invariance relation that captures accurately the first-principles results for transverse response of SWNTs and MWNTs. Because of strong screening and radius dependence of polarizability, the outer few layers dominate the response in MWNTs.

Using the results of our calculations, we analyze the feasibility of separating semiconducting and metallic nanotubes using uniform and non-uniform static electric fields in vacuum and in solutions. We also find that the dielectric response of non-chiral SWNTs in both directions remains linear up to very high values of the applied field.

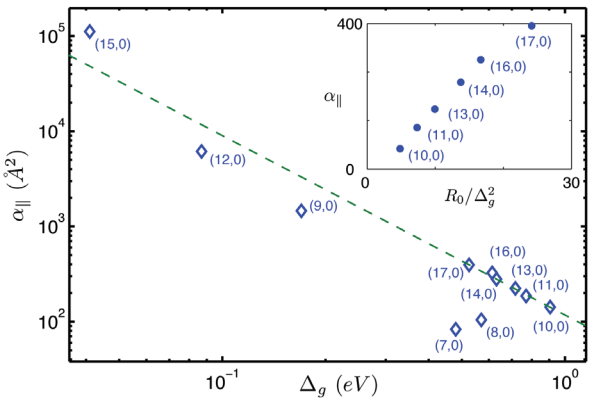

▲ Figure 1: Log scale plot of the longitudinal polarizability (per unit length) of zigzag semiconducting SWNTs as a function of the band gap. The dashed line has slope –2. The inset shows the values for large-gap zigzag SWNTs as a function of radius divided by band gap squared.

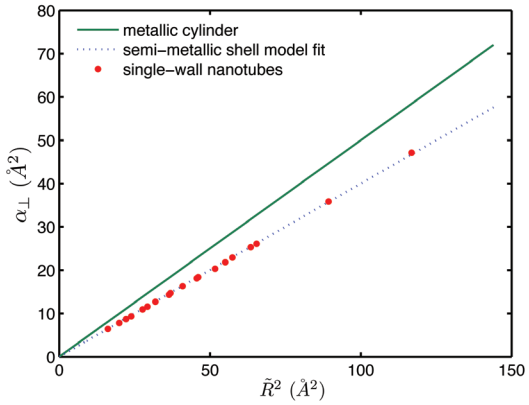

▲ Figure 2: Transverse polarizabilities (per unit length) of armchair and zigzag nanotubes as a function of radius squared. The solid line corresponds to an ideal metallic cylinder, and the dashed line is the best fit of the first-principles results. This figure shows that transverse polarizabilities of SWNTs of different band gaps and chiralities lie on the same line.

REFERENCES

[1] B. Kozinsky and N. Marzari, "Static dielectric properties of carbon nanotubes from first principles," *Phys. Rev. Lett.*, May 2006, to be published.

Niobium Superconducting Persistent-Current Qubits with Deep Submicron Josephson Junctions

D.M. Berns, W.D. Oliver, S.O. Valenzuela, T.P. Orlando, V. Bolkhovsky, E. Macedo

Quantum computation holds the potential to solve problems currently intractable with current computers. The basic component of a quantum computer is the "qubit," the quantum analog to today's bits. Any two-level quantum system could serve as a qubit; however, the qubit must satisfy two major criteria for practical quantum computing: long coherence times and the ability to scale to thousands of qubits. Persistent-current (PC) qubits are promising candidates for realizing such a large-scale quantum computer. The PC qubit is a superconducting circuit with Josephson junction (JJ) elements that can be effectively operated as a two-level quantum system [1].

With a tri-layer process using optical lithography, we can create the deep-submicron JJs required to realize large qubit tunnel-couplings, which allow improved immunity to dielectric-induced decoherence, and there is no foreseeable barrier to large-scale integration. We have recently begun measuring and characterizing the PC qubits designed with these deep-submicron JJs fabricated with the Nb-Al/AlOx-Nb trilayers. Initital testing of the JJs shows excellent performance down to sizes necessary for long decoherence times (Figure 1), and first studies of how the ground state of the new qubits changes as the applied DC flux is swept show the large tunnel-couplings we were aiming for (Figure 2).

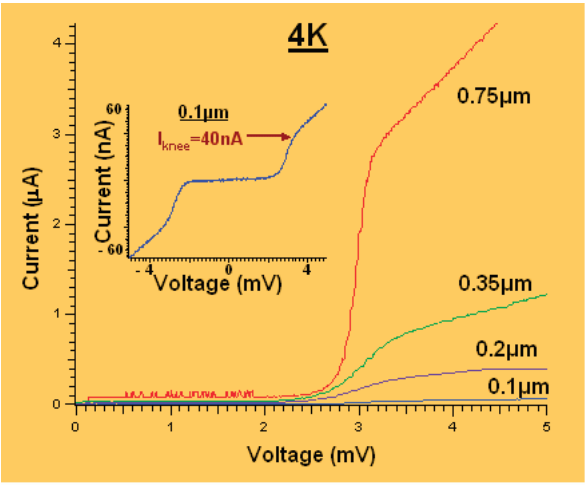

▲ Figure 1: IV traces taken at 4K for a few different test junctions, from 0.75 um down to 0.1um. Blown up in the inset is the 0.1 um junction IV and we see a knee current of 40 nA and a very large subgap resistance.

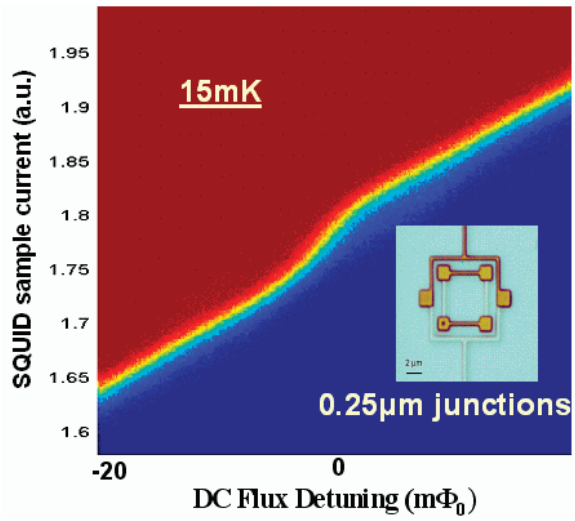

▲ Figure 2: Qubit step taken at dilution refrigerator temperatures with the device seen in the inset, where the larger junctions are 250 nm on a side. One can clearly see that as the applied dc magnetic flux is changed, the ground state changes from one circulating current state to the other.

REFERENCES

[1] T.P. Orlando, J.E. Mooij. L. Tian, C.H. van der Wal, L.S. Levitov, S. Lloyd, J.J. Mazo, "Superconducting persistent-current qubit," *Phys. Rev. B: Condensed Matter and Materials Physics*, vol. 60, no. 22, pp. 15398-15413, December 1999.

Mach-Zehnder Interferometry in a Persistent-Current Qubit

W.D. Oliver, Y. Yu, J.C. Lee, K.K. Berggren, L.S. Levitov, T.P. Orlando

We have demonstrated Mach-Zehnder (MZ)-type interferometry with a niobium superconducting persistent-current qubit. These experiments exhibit remarkable agreement with theory, and they will find application to non-adiabatic qubit control methods. The qubit is an artificial atom, the ground and first-excited states of which exhibit an avoided crossing. Driving the qubit with a large-amplitude harmonic excitation sweeps it through this avoided crossing two times per period. The induced Landau-Zener (LZ) transitions at the avoided crossing cause coherent population transfer between the eigenstates, and the accumulated phase between LZ transitions varies with the driving amplitude. This is analogous to a MZ interferometer, in which the LZ transition is the beamsplitter and the relative phase accumulated between LZ transitions is the optical path-length difference between the arms of the interferometer. Over the entire length of the microwave driving pulse, we have a sequence of MZ interferometers. We have observed MZ quantum interference fringes as a function of the driving amplitude for single- and multi-photon excitations.

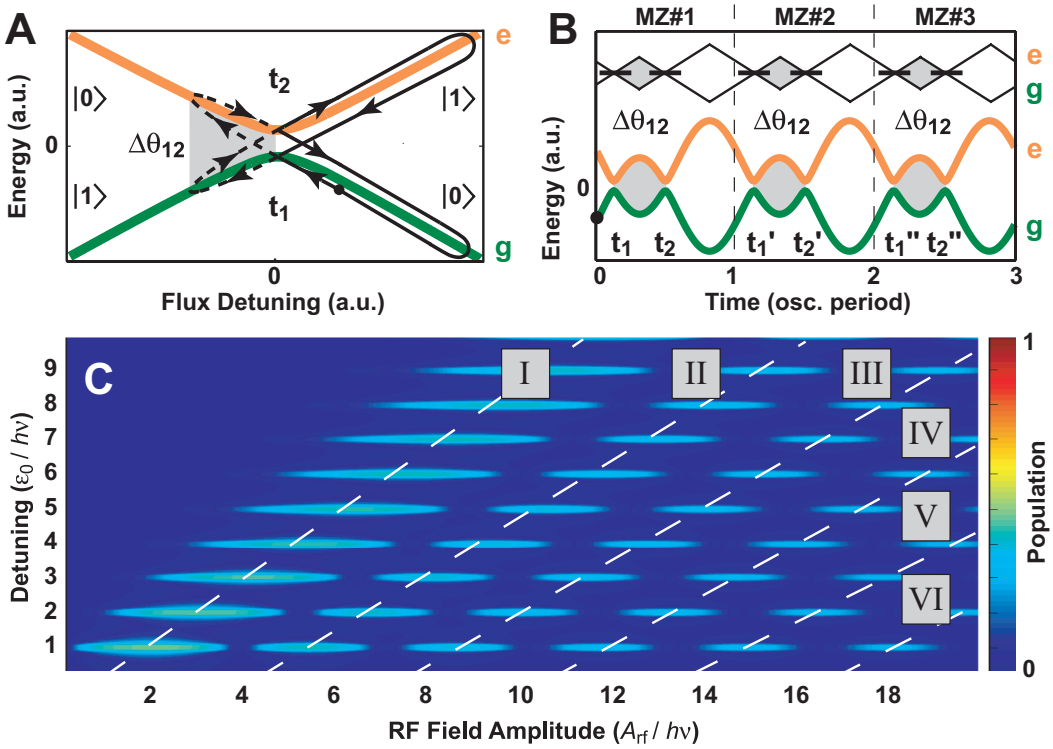

▲ Figure 1: (a) Energy of the two-level system. Starting at the marker, the qubit state is swept through the avoided crossing twice, accumulating a phase between the LZ transitions that occur. (b) The corresponding energy variation over a few pulse periods. The sequence of LZ transitions and phase accumulation are analogous to a sequence of Mach-Zehnder interferometers. (c) Qubit population as a function of driving amplitude. We see the Bessel dependence to the Mach-Zehnder-like quantum interference for n-photon transitions.

REFERENCES

[1] W.D. Oliver, Y. Yu, J.C. Lee, K.K. Berggren, L.S. Levitov, T.P. Orlando, "Mach-Zehnder interferometry in a strongly driven superconducting qubit," *Science*, vol. 310, no. 5754, pp. 1653 - 1657, Dec. 2005.

Coherent Quasi-classical Dynamics of a Niobium Persistent-Current Qubit

D.M. Berns, S.O. Valenzuela, W.D. Oliver, L.S. Levitov, T.P. Orlando

We have recently demonstrated Mach-Zehnder-type interferometry in the persistent-current qubit, in the strong driving limit [1]. We have now extended this work to much lower driving frequencies. By driving our system at frequencies smaller than our linewidth, we have observed a new regime of quasi-classical dynamics within the strong driving limit. Now a transition at a DC flux detuning resonant with n photons is assisted by neighboring resonances. In this regime we find remarkable agreement with theory by assuming the population transfer rate for the n^{th} photon resonance is the sum of rates from all other resonances.

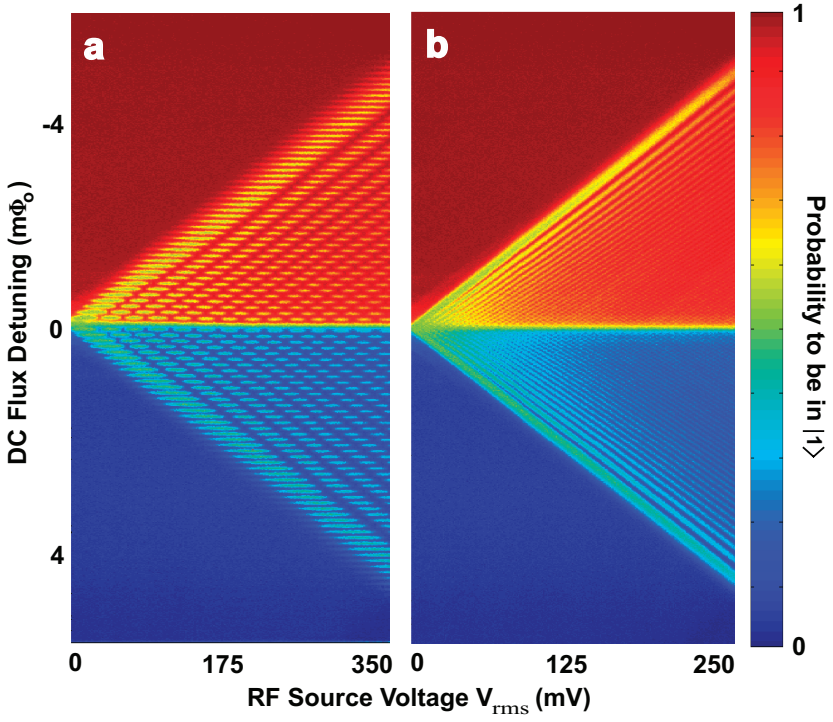

◀ Figure 1 : Qubit population as a function of driving amplitude. (a) Driving frequency = 270 MHz. We see the Bessel dependence to the Mach-Zehnder-like quantum interference for n-photon transitions. (b) Driving frequency = 90 MHz. Individual resonances are no longer distinguishable but we still see coherent quantum interference.

REFERENCES

[1] W.D. Oliver, Y.G. Yu, J.C. Lee, K.K. Berggren, L.S. Levitov, and T.P. Orlando, "Mach-Zehnder interferometry in a strongly driven superconducting qubit," *Science*, vol. 310, no. 5754, pp. 1653-1657, Dec. 2005.

Resonant Readout of a Persistent Current Qubit

J.C. Lee, W.D. Oliver, T.P. Orlando
Sponsorship: DURINT, ARDA, NSF

The two logical states of a persistent current (PC) qubit correspond to oppositely circulating currents in the qubit loop. The induced magnetic flux associated with the current either adds to or subtracts from the background flux. The state of the qubit can thus be detected by a DC SQUID magnetometer inductively coupled to the qubit.

We have implemented a resonant technique that uses a SQUID as a flux-sensitive Josephson inductor for qubit readout. This approach keeps the readout SQUID biased at low currents along the supercurrent branch and is more desired for quantum computing applications in reducing the level of decoherence on the qubit. By incorporating the SQUID inductor in a high-Q on-chip resonant circuit, we can distinguish the two flux states of a niobium PC qubit by observing a shift in the resonant frequency of the readout circuit. The nonlinear nature of the SQUID Josephson inductance, as well as its effect on the resonant spectra of the readout circuit, was also characterized.

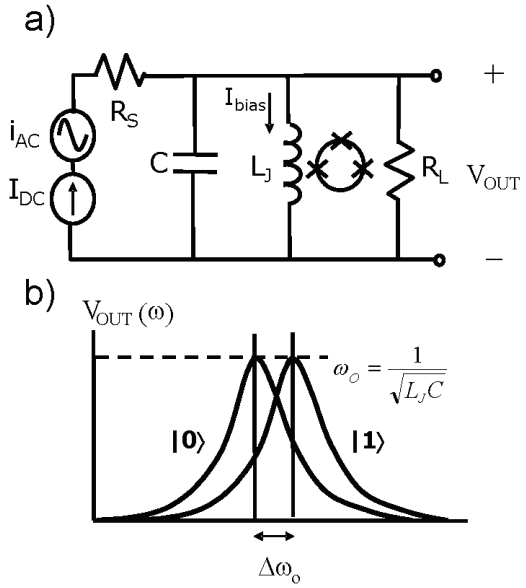

▲ Figure 1: a) The SQUID inductor is incorporated in a resonant readout circuit. It is inductively coupled to a PC qubit to detect its state. b) A transition of the qubit state changes the Josephson inductance of the SQUID and can be sensed as a shift in the resonant frequency of the readout circuit.

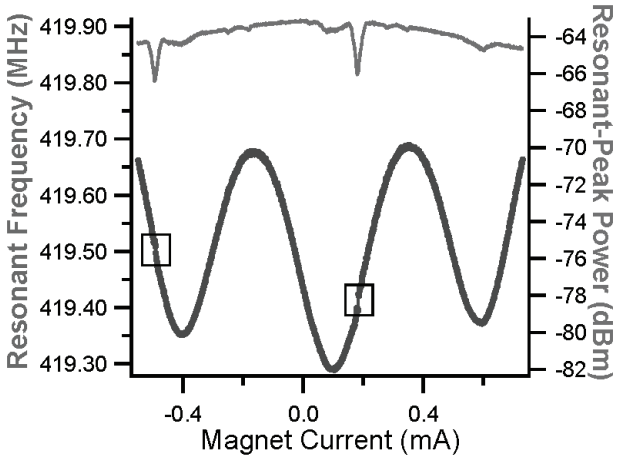

▲ Figure 2: Experimental results at 300 mK: the lower plot (left axis) shows the modulation of the resonant frequency with external magnetic field. Qubit steps corresponding to transitions between opposite flux states were observed at every 1.3 periods of the SQUID lobe. The upper plot (right axis) shows the corresponding peak amplitude of the resonant spectrum. The dip in peak power coincides with the qubit step.

REFERENCES

[1] J.C. Lee, W.D. Oliver, T.P. Orlando, and K.K. Berggren, "Resonant readout of a persistent current qubit," *IEEE Transactions on App. Superconductivity*, vol. 15, no. 2, pp. 841-844, June 2005.

[2] J.C. Lee, "Magnetic flux measurement of superconducting qubits with Josephson inductors," Master's thesis, Massachusetts Institute of Technology, Cambridge, 2002.

Type-II Quantum Computing Using Superconducting Qubits

D. Berns, W.M. Kaminsky, B. Cord, K.K. Berggren, W.D. Oliver, T.P. Orlando (in coll. with J. Yepez, Air Force Laboratories)
Sponsorship: AFOSR, Fannie and John Hertz Foundation

Most algorithms designed for quantum computers will not best their classical counterparts until they are implemented with thousands of qubits. For example, the factoring of binary numbers with a quantum computer is estimated to be faster than a classical computer only when the length of the number is greater than about 500 digits [1]. In contrast, the factorized quantum lattice-gas algorithm (FQLGA) [2] for fluid dynamics simulation, even when run on a quantum computer significantly smaller than the one just discussed, has significant advantages over its classical counterparts.

The FQLGA is the quantum version of classical lattice-gases (CLG) [3]. CLGs are an extension of classical cellular automata with the goal of simulating fluid dynamics without reference to specific microscopic interactions. The binary nature of the CLG lattice variables is replaced for the FQLGA by the Hilbert space of a two-level quantum system. The results of this replacement are similar to that of the lattice-Boltzmann model, but with a few significant differences [4]. The first is the exponential decrease in required memory. The second is the ability to simulate arbitrarily small viscosities.

We have recently developed two implementations of the algorithm for the 1D diffusion equation using the PC Qubit [5]. The first consists of initializing the qubits while keeping them in their ground state, and then performing the collision by quickly changing their flux bias points and then performing a single $\pi/2$ pulse (Figure 1). This initialization technique could prove quite useful, since relaxation effects are avoided, but the way we have implemented the collision is not easily generalized to other collisions. A more general collision implementation was then developed by decomposing the unitary collision matrix into a sequence of single qubit rotations and coupled free evolution. The single qubit rotations then also serve to initialize the fluid's mass density.

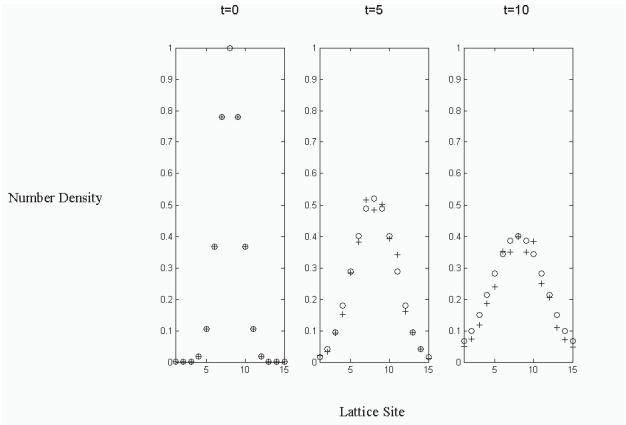

▲ Figure 1: Simulation of the FQLGA for 1D diffusion is pictured(o) alongside simulation of the first proposed implementation(+). The expected diffusion of a gaussian is observed.

REFERENCES

[1] K.K. Berggren, "Quantum computing with superconductors," i*Proc. of the IEEE*, vol. 92, no. 10, pp. 1630-1638, Oct. 2004.
[2] J. Yepez, "Quantum computation of fluid dynamics," *Lecture Notes in Computer Science*, vol. 1509, p. 34, Feb. 1998.
[3] D.A. Wolf-Gladrow, *Lattice-Gas Cellular Automata and Lattice-boltzmann Models– An Introduction*. Berlin: Springer, 2000.
[4] J. Yepez, "An efficient quantum algorithm for the ne-dimensional Burgers equation," *quant-ph*\ 0210092, Oct. 2002.
[5] D.M. Berns and T.P. Orlando, "Implementation schemes for the factorized quantum lattice-gas algorithm for the one- dimensional diffusion equation using persistent-current qubits," *Quantum Information Processing*, vol. 4, no. 4, p. 265, 2005.

Scalable Superconducting Architecture for Adiabatic Quantum Computation

W.M. Kaminsky, S. Lloyd, T.P. Orlando
Sponsorship: Fannie and John Hertz Foundation

Adiabatic quantum computation (AQC) is an approach to universal quantum computation in which the entire computation is performed in the ground state of a suitably chosen Hamiltonian [1]. As such, AQC offers intrinsic protection against dephasing and dissipation [2,3]. Moreover, AQC naturally suggests a novel quantum approach to the classically intractable constrained minimization problems of the complexity class NP. Namely, by exploiting the ability of coherent quantum systems to follow adiabatically the ground state of a slowly changing Hamiltonian, AQC promises to bypass automatically the many separated local minima occurring in difficult constrained minimization problems that are responsible for the inefficiency of classical minimization algorithms. To date, most research on AQC [4-8] has focused on determining the precise extent to which it could outperform classical minimization algorithms. The tantalizing possibility remains that–at least for all practical purposes–AQC offers at least a large polynomial, and often an exponential, speedup over classical algorithms. However, it may be the case that in the same way the efficiency of many practical classical algorithms for NP problems can be established only empirically, the efficiency of AQC on large instances of classically intractable problems can be established only by building a large-scale AQC experiment.

To make feasible such a large-scale AQC experiment, we have proposed a scalable architecture for AQC based on the superconducting persistent-current (PC) qubits [9, 10] already under development here at MIT. As first proposed in [11], the architecture naturally incorporates the terms present in the PC qubit Hamiltonian by exploiting the isomorphism [12] between antiferromagnetic Ising models in applied magnetic fields and the canonical NP-complete graph theory problem Max Independent Set. Such a design notably removes any need for the interqubit couplings to be varied during the computation. Moreover, since Max Independent Set remains NP-complete even when restricted to planar graphs where each vertex is connected to no more than 3 others by edges, a scalable programmable architecture capable of posing any problem in the class NP may simply take the form of a 2D, hexagonal, square, or triangular lattice of qubits. Finally, the latest version of the architecture [13] permits interqubit couplings to be limited to nearest-neighbors and qubit measurements to be inefficient.

REFERENCES

[1] D. Aharonov, W. van Dam, J. Kempe, Z. Landau, S. Lloyd, and O. Regev, "Adiabatic quantum computation is equivalent to standard quantum computation," *The Quantum Physics E-Print Archive*, no. 0405098, Mar. 2005; available: http://arxiv.org/abs/quant-ph/0405098.

[2] A.M. Childs, E. Farhi, and J. Preskill, "Robustness of adiabatic quantum computation," *Physical Review A: Atomic, Molecular, and Optical Physics*, vol. 65, no. 1, pp. 012322:1-10, Jan. 2002.

[3] J. Roland and N.J. Cerf, "Noise resistance of adiabatic quantum computation using random matrix theory," *Physical Review A: Atomic, Molecular, and Optical Physics*, vol. 71, no. 3, p. 032330:1-9, Mar. 2005.

[4] E. Farhi, J. Goldstone, S. Gutmann, J. Lapan, A. Lundgren, and D. Preda, "A quantum adiabatic evolution algorithm applied to random instances of an NP complete problem," *Science*, vol. 292, pp. 472-475, Apr. 2001.

[5] A.M. Childs, E. Farhi, J. Goldstone, and S. Gutmann, "Finding cliques by quantum adiabatic evolution," *Quantum Information and Computation*, vol. 2, no. 3, pp. 181-191, May 2002.

[6] W. van Dam, M. Mosca, and U. Vazirani, "How powerful is adiabatic quantum computation?" *42nd Annual Symposium on Foundations of Computer Science* , Las Vegas, NV, pp. 279–287, Oct. 2001.

[7] E. Farhi, J. Goldstone, and S. Gutmann, "Quantum adiabatic evolution algorithms versus simulated annealing," *The Quantum Physics E-Print Archive*, no. 0201031, Jan. 2002; available: http://arxiv.org/abs/quant-ph/0201031.

[8] G.E. Santoro *et al.*, "Theory of quantum annealing of an Ising spin glass," *Science*, vol. 295, pp. 2427-2430, March 2002.

[9] E.J. Mooij *et al.*, "Josephson persistent-current qubit," *Science*, vol. 285, pp. 1036-1039, Aug. 1999.

[10] T.P. Orlando *et al.* "Superconducting persistent-current qubit," *Physical Review B: Condensed Matter and Materials Physics*, vol. 60, no. 22, pp. 15398-15413, Dec. 1999.

[11] W.M. Kaminsky, and S. Lloyd, "Scalable architecture for adiabatic auantum computing of NP-hard problems," in *Quantum Computing and Quantum Bits in Mesoscopic Systems*, eds. A.J. Leggett, B. Ruggiero, and P. Silvestrini, (New York: Kluwer Academic, 2004), pp. 229-236.

[12] F. Barahona, "On the computational complexity of Ising spin glass models," *J. of Physics A: Mathematical and General*, vol. 15, no. 10, pp. 3241-3253, Oct. 1982.

[13] W.M. Kaminsky, S. Lloyd, and T.P. Orlando, "Scalable superconducting architecture for adiabatic quantum computation," *The Quantum Physics E-Print Archive*, no. 0403090, Mar. 2004; available: http://arxiv.org/abs/quant-ph/0403090.

Fabrication Methods for Adiabatic Quantum Computing Devices

B. Cord, W. Kaminsky, T.P. Orlando, K.K. Berggren
Sponsorship: Quantum Computing Graduate Research Fellowship, AFOSR

Adiabatic quantum computing devices (AQCs) have been implemented successfully in several types of systems, including ion traps, nuclear spins, and photon cavities. However, we find implementing AQCs in superconductive circuits offers several key advantages. Primarily, using standard techniques adapted from the semiconductor industry, we can fabricate very large numbers of superconductor-based qubits in CMOS-compatible materials [1]

The stringent resolution and uniformity requirements for AQC devices present an interesting fabrication challenge. In order to perform certain AQC experiments, Josephson junctions with diameters of ~50 nm are useful. While previous quantum computing experiments at MIT used devices fabricated using optical projection lithography, sub-100-nm dimensions require alternate techniques, such as electron-beam lithography and suspended shadow-mask evaporation. Additionally, the uniformity of these nanoscale junctions must be high and the areas of the Josephson junctions within a single device must exhibit very low variation.

No readily available lithographic technology meets these requirements, so research is being conducted on methods of defining arbitrary features as small as 50 nm with the precision required for adiabatic quantum computing. Current experiments have focused on improving the resolution and uniformity of the scanning electron-beam lithography (SEBL) system in the Nanostructures Laboratory, particularly in investigating the effects of different pattern geometries on the uniformity of very small features. Parallel work is also being done on a reliable, automated method of measuring the dimensions of very small structures for the purposes of determining uniformity, using scanning electron microscope (SEM) images and image-processing software.

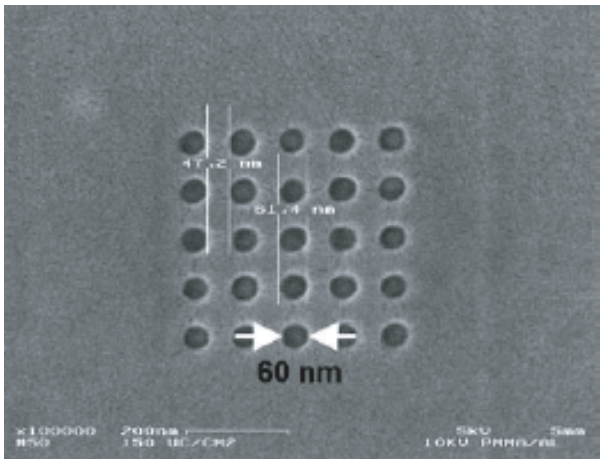

▲ Figure 1: An SEM of an array of 60-nm-diameter features in photoresist.

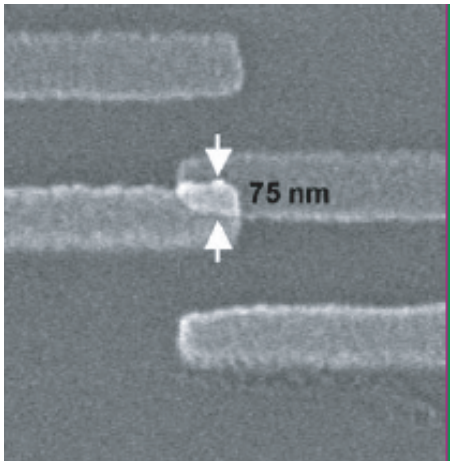

▲ Figure 2: An SEM of an 0.007-μm^2 Al/AlOx/Al Josephson junction fabricated via shadow-mask evaporation.

REFERENCES

[1] K.K. Berggren, "Quantum computing with superconductors," *Proceedings of the IEEE*, vol. 92, no. 10, pp. 1630-1638, October 2004.

Probing Decoherence with Electromagnetically Induced Transparency in Superconductive Quantum Circuits

K. Murali, W.D. Oliver, T.P. Orlando (in coll. with Z. Dutton, Naval Research Laboratory)
Sponsorship: DURINT, ARDA

Superconductive quantum circuits (SQCs) comprising mesoscopic Josephson junctions, quantized flux, and/or charge states are analogous to the quantized internal levels of an atom [1]. This SQC-atom analogy can be extended to the quantum optical effects associated with atoms, such as electromagnetically induced transparency (EIT) [2, 6].

The three-level Λ-system for our S-EIT system (Figure 1a) is a standard energy-level structure utilized in atomic EIT. It comprises two meta-stable states $|1\rangle$ and $|2\rangle$, each of which may be coupled to a third excited state $|3\rangle$. In an atomic EIT scheme, a strong "control" laser couples the $|2\rangle \rightarrow |3\rangle$ transition, and a weak resonant "probe" laser couples the $|1\rangle \rightarrow |3\rangle$ transition. By itself, the probe laser light is readily absorbed by the atoms and thus the transmittance of the laser light through the atoms is very low. However, when the control and probe laser are applied simultaneously, destructive quantum interference between the atomic states involved in the two driven transitions causes the atom to become "transparent" to both the probe and control laser light [2-4]. Thus, the light passes through the atoms with virtually no absorption. In this work, we propose to use EIT in SQCs to sensitively probe decoherence.

The SQC (Figure 1b) can be biased to result in an asymmetric double-well potential as shown in Figure 2. The three states in the left well constitute the superconductive analog to the atomic Λ-system [5]. States $|1\rangle$ and $|2\rangle$ are "meta-stable" qubit states, with a tunneling and coherence time much longer than the excited "readout" state $|3\rangle$. State $|3\rangle$ has a strong inter-well transition when tuned on-resonance to state $|4\rangle$. Thus, a particle reaching state $|3\rangle$ will tend to tunnel quickly to state $|4\rangle$, causing the circulating current to switch to the other direction, an event that is detected with a SQUID. Knowing how long the SQC remains transparent, i.e., does not reach state $|3\rangle$, in the S-EIT experiment provides an estimate of the decoherence time.

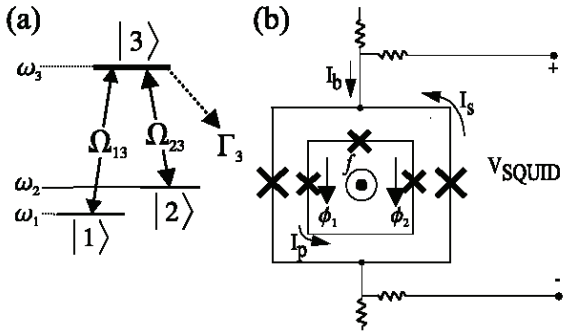

▲ Figure 1: a. Energy level diagram of a three-level Λ system. EIT can occur in atoms possessing two long-lived states |1>, |2>, each of which is coupled via resonant laser light fields to a radiatively decaying state |3>. b. Circuit schematic of the persistent –current qubit and its readout SQUID.

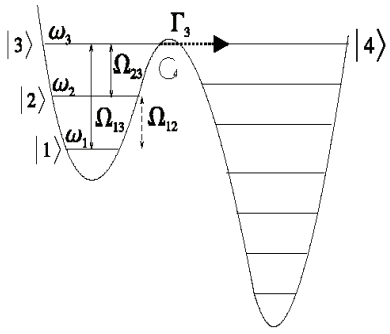

▲ Figure 2: One-dimensional double-well potential and energy-level diagram for a three-level SQC.

REFERENCES

[1] A.J. Leggettand A. Garg, "Quantum mechanics versus macroscopic realism: Is the flux there when nobody looks?" *Phys. Rev. Lett.*, vol. 54, no. 9, pp. 857-860, Mar. 1985.

[2] L.V. Hau, S.E. Harris, Z. Dutton, and C.H. Behroozi, "Light speed reduction to 17 meters per second in an ultracold atomic gas," *Nature*, vol. 397, no. 6720, pp. 594-598, 1999.

[3] K.J. Boller, A. Imamoglu, and S.E. Harris, "Observation of electromagnetically induced transparency," *Phys. Rev. Lett.*, vol. 66, no. 20, pp. 2593-2596, May 1991.

[4] C.J. Cohen-Tannoudji, J. Dupont-Roc, and G. Grynberg, *Atom-photon intereactions*, New York: John Wiley & Sons, Inc., 1992.

[5] J.E. Mooij, T.P. Orlando, L. Levitov, L. Tian, C.H. van der Wal, and S. Lloyd, "Josephson persistent-current qubit," *Science*, vol. 285, no. 5430, pp. 1036-1039, Aug. 1999.

[6] K.V.R.M. Murali, Z. Dutton, W.D. Oliver, D.S. Crankshaw, and T.P. Orlando, "Probing decoherence with electromagnetically induced transparency in superconductive quantum circuits," *Phys. Rev. Lett.*,vol. 93, no 8, 087003 Aug. 2004.

Magnetoelastic Behavior of Magnetic Nanostructures

E. Friend, C.A. Ross, R.C. O'Handley
Sponsorship: NSF

Previous researchers have investigated the magnetic properties of multilayer thin-film sandwiches of copper/ nickel/ copper epitaxially grown on silicon [1]. In this system, the magnetic properties of the nickel layer change drastically as the thickness (and therefore the amount of strain) of the nickel layer varies, and it does so over a thickness range that is uniquely broad. This effect is due to both the large magnetoelastic energy and to the surface magnetocrystalline anisotropy energy of the nickel film.

Our research focuses on understanding the effects of patterning these Cu/Ni/Cu films into nanoscale lines. Once patterned, the strained films can relax at the edges, with the strain relief being a function of line width and thickness. The ultimate aims are to elucidate the relationship between stress and magnetic properties in nanoscale features, to understand and control the effects of stress on magnetic nanostructures, and to exploit this effect to achieve desired magnetic properties. Understanding this relationship is a key part of the development of future magnetic recording technologies such as patterned recording media and read/ write heads.

Magnetic characterization of Cu/Ni/Cu nanolines (Figure 2) has shown that, contrary to the expectations from shape anisotropy, the preferred magnetization direction is transverse to the line direction in the sample plane [2]. This preference is due to strain relief in the nanoline across its width. Simulations of strain in these structures (Figure 1) have shed further light on the relation between the nanoline cross-section aspect ratio and strain relief, showing that strain is relaxed at the edges of the lines over a distance of about 1.5 times the film thickness. Therefore narrower lines show a greater magnetic anisotropy parallel to their width. Strain relief is even greater in the case of overetch into the copper substrate. Magnetic anisotropy data is being analyzed to understand how the net anisotropy of the nanolines agrees with theoretical models.

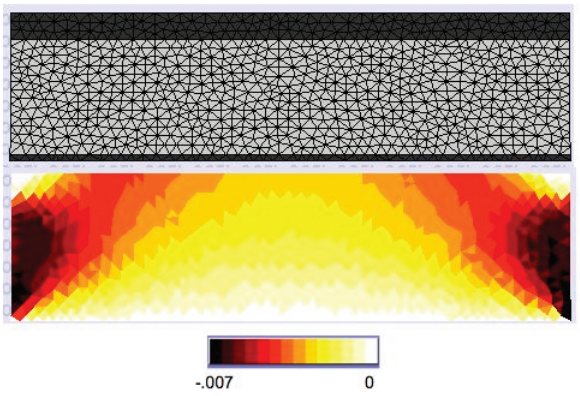

▲ Figure 1: Strain relief simulation for 100-nm-wide stripe of epitaxial Cu (50 Å)/Ni (206 Å)/Cu (20.6 Å) on Cu (~2000 Å)/Si. The top panel shows the mesh of the model while the lower panel shows the amount of strain relaxation, which is greater at the edges of the stripe.

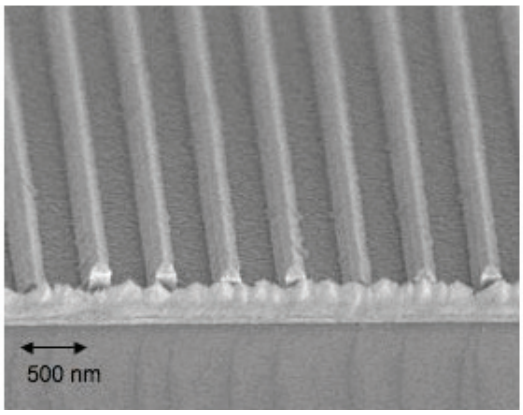

▲ Figure 2: An SEM image of Cu (50 Å)/Ni (206 Å)/Cu (2000 Å)/Si nanolines with 500-nm-period. The facetted layer on the lines is the remains of the hard-etch mask.

REFERENCES

[1] G. Bochi, C.A. Ballentine, H.E. Inglefield, C.V. Thompson, and R.C. O'Handley, "Evidence for strong surface magnetoelastic anisotropy in epitaxial Cu/Ni/Cu(001) sandwiches," *Phys. Rev. B.*, vol. 53, no. 4, pp. R1729-R1732, Jan. 1996.

[2] E.S. Lyons, R.C. O'Handley and C.A. Ross, "Magnetic anisotropy of epitaxial Cu/Ni/Cu nanolines," *J. Appl. Phys.* vol. 95, no. 11, p. 6711-6713, June 2004.

[3] E.S. Lyons, R.C. O'Handley and C.A. Ross, "Effect of nano-patterning on anisotropy of Cu/Ni/Cu nanolines" *J. Appl. Phys.* vol. 99, p. 08R105, Apr. 2006.

Templated Self-assembly of Block Copolymers for Nanolithography

C.A. Ross, H.I. Smith, F. Ilievski, V. Chuang, Y.S. Jung
Sponsorship: NSF, CMSE, Singapore-MIT Alliance, SRC

Large-area, periodic nanoscale structures are interesting for understanding fundamental material properties as well as for developing novel applications, such as the fabrication of magnetic media or contacts to nano-sized devices. Self-organizing systems provide a simple and low-cost method of fast fabrication of periodic nanoscale structures. One such system is the family of compounds called block-copolymers that we have been using. Block copolymers consist of two covalently bound polymer chains of chemically distinct polymer materials. The chains can self-assemble to form small-scale domains whose size and geometry depend on the molecular weights of the two types of polymer and their interaction[1]. The domains have a very uniform distribution of sizes and shapes. We have been using block copolymers as templates for the formation of structures such as magnetic particles, by selectively removing one type of domain and using the resulting template to pattern a nanostructured magnetic film. We have successfully applied this patterning process to the fabrication of magnetic dots from Co, NiFe[2] and multilayer CoFe/Cu/NiFe[2] films. One drawback of this technique is that the as-cast block copolymer forms a short-range ordered structure, whereas many applications require long-range ordered structures. It is therefore necessary to guide the microphase separation of the block copolymer by a process called templating. This can be done by using a substrate with shallow grooves as guides for a single layer of spheres[3] or cylinders that could be utilized in fabrication of nanorods and nanowires. Deep v-shaped grooves provide an interesting model for analyzing the ordering in 3 dimensions (Figure 1). Lastly, by combining this technique with nanoimprint lithography (Figure 2), we can achieve large-scale alignment and avoid additional steps for removal of the guiding template.

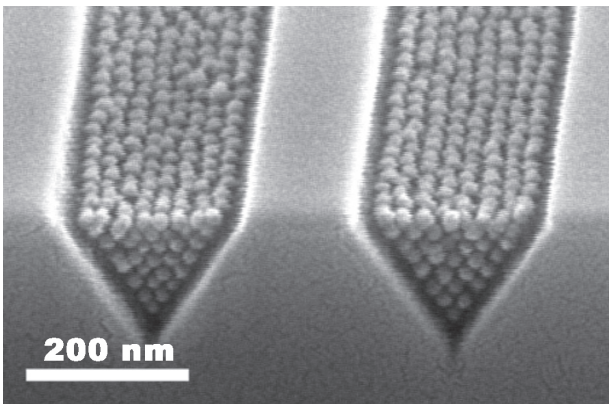

▲ Figure 1: Self-assembled block copolymer in a v-shaped groove. For imaging, one of the blocks was removed by oxygen plasma etching to reveal the structure of the other block. The number of rows of spheres increases in a quantized manner from the bottom up (one row of spheres, then two, etc.) Half-spheres and other transitions do not form.

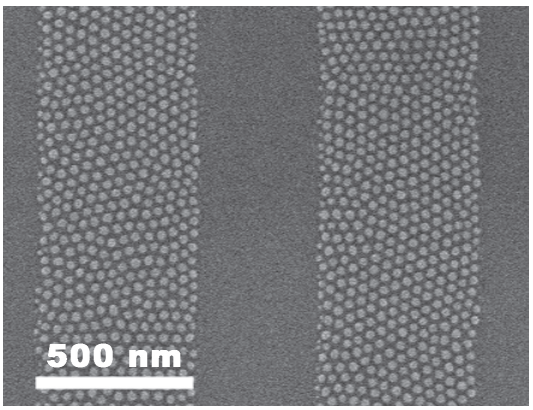

▲ Figure 2: Initial results in templated block copolymers using nanoimprint lithography. A 1-μm- period mold was pressed into a thin layer of block copolymer on a flat substrate and both were annealed to induce the phase separation. The polymer was pushed out of regions where the mold was in contact with the substrate. If transferred into a magnetic layer, similar dots could be used as storage units for single bits in magnetic media. We are currently working on methods of improving the long-range order.

REFERENCES

[1] E.L. Thomas and R.L. Lescanec, "Phase morphology in block copolymer systems," *Phil. Trans. R. Soc. Lond. A*, vol. 348, pp. 146-164, 1994.

[2] J.Y. Cheng and C.A. Ross, "Magnetic nanostructures from block copolymer lithography: Hysteresis, thermal stability and magnetoresistance," *Phys. Rev. B*, vol.70, pp. 064417, 2004.

[3] J. Cheng, C.A. Ross, and A. Mayes, "Nanostructure engineering by templated self-assembly," *Nature Materials* 3, pp. 823-828, 2004.

Scanning Beam Interference Lithography

M. Ahn, C.-H. Chang, R. Heilmann, J. Montoya, Y. Zhao, M.L. Schattenburg
Sponsorship: NASA, Plymouth Grating Laboratory

Traditional methods of fabricating gratings, such as diamond tip ruling, electron and laser beam scanning, or holography, are generally very slow and expensive and result in gratings with poor control of phase and period. More complex periodic patterns, such as gratings with chirped or curved lines, or 2D and 3D photonic patterns, are even more difficult to pattern. This research program seeks to develop advanced interference lithography tools and techniques to enable the rapid patterning of general periodic patterns with much lower cost and higher fidelity than current technology.

Interference lithography (IL) is a maskless lithography technique based on the interference of coherent beams. Interfering beams from an ultra-violet laser generates interference fringes which are captured in a photo-sensitive polymer resist. Much of the technology used in modern IL practice is borrowed from technology used to fabricate computer chips. Traditional IL methods result in gratings with large phase and period errors. We are developing new technology based on interference of phase-locked scanning beams, called scanning beam interference lithography (SBIL). The SBIL technique has been realized in a tool called the MIT Nanoruler, which recently won an R&D 100 award (Figure 1). Large gratings can be patterned in a matter of minutes with a grating phase precision of only a few nanometers and a period error in the ppb range (Figure 2).

Current research efforts seek to generalize the SBIL concept to pattern more complex periodic patterns, such as variable period (chirped) gratings, 2D metrology grids, and photonic patterns [1]. Important applications of large, high fidelity gratings are for high-resolution x-ray spectroscopes on NASA x-ray astronomy missions, high energy laser pulse compression optics, and length metrology standards. We are in the process of a major upgrade of the Nanoruler optical and mechanical system which will allow rapid variation and control of grating pitch and fringe orientation, which will enable a new mode of operation of the Nanoruler that we call variable-period SBIL.

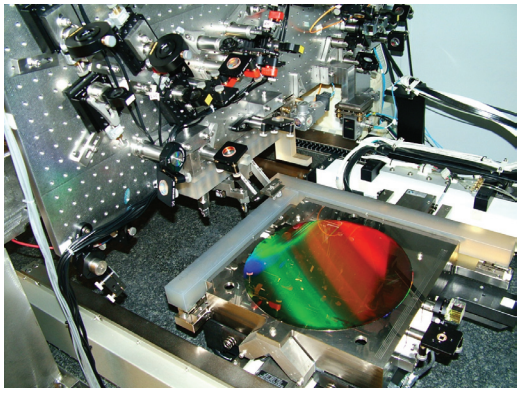

▲ Figure 1: Photograph of the Nanoruler lithography and metrology system built by MIT students. This unique tool is the most precise grating patterning and metrology system in the world.

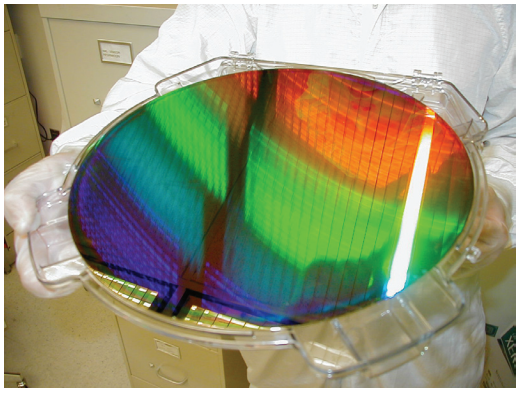

▲ Figure 2: A 300mm-diameter silicon wafer patterned with a 400-nm-period grating by the Nanoruler. The grating is diffracting light from the overhead fluorescent bulbs.

REFERENCES

[1] G.S. Pati, R.K. Heilmann, P.T. Konkola, C. Joo, C.G. Chen, E. Murphy, and M.L. Schattenburg,"A generalized scanning beam interference lithography system for patterning gratings with variable period progressions," *J. Vac. Sci. Technol.* B, vol. 20, pp. 2617-2621, 2002.

[2] P. Konkola, C. Chen, R.K. Heilmann, C. Joo, J. Montoya, C.-H. Chang, and M.L. Schattenburg, "Nanometer-level repeatable metrology using the Nanoruler," *J. Vac. Sci. Technol.* B, vol. 21, pp. 3097-3101, 2003.

[3] J. Montoya, C.-H. Chang, R.K. Heilmann, and M.L. Schattenburg, "Doppler writing and linewidth control for scanning beam interference lithography," *J. Vac. Sci. Technol. B,* vol. 23, pp. 2640-2645, 2005.

[4] C.-H. Chang, R.K Heilmann, and M.L. Schattenburg, "Advanced heterodyne fringe-locking system using multiple frequency shifts," *Proc. of the 20th Annual Meeting of the Am. Soc. for Precision Eng.*, vol. 37, pp. 375-378, 2005.

Nanofabricated Reflection and Transmission Gratings

M. Ahn, C.-H Chang, R. Heilmann, J. Montoya, Y. Zhao, M.L. Schattenburg
Sponsorship: NASA

Diffraction gratings and other periodic patterns have long been important tools in research and manufacturing. Diffraction is due to the coherent superposition of waves—a phenomena with many useful properties and applications. Waves of many types can be diffracted, including visible and ultraviolet light, x-rays, electrons and even atom beams. Periodic patterns have many useful applications in fields such as optics and spectroscopy, filtering of beams and media, metrology, high-power lasers, optical communications, semiconductor manufacturing, and nanotechnology research in nanophonics, nanomagnetics and nanobiology.

The performance of a grating is critically dependant on the geometry of individual grating lines. Lines can have rectangular, triangular or other geometries, depending on the application. High efficiency requires control of the geometric parameters which define individual lines, e.g., width, height, smoothness, sidewall angle, etc., in the nanometer or even sub-nanometer range. For some applications control of grating period in the picometer to femtometer range is critical. Traditional methods of fabricating gratings, such as diamond tip ruling, electron and laser beam scanning, or holography, generally result in gratings which fall far below theoretical performance limits due to imperfections in the grating line geometry. The main goal of our research is to develop new technology for the rapid generation of general periodic patterns with control of geometry measured in the nanometer to sub-nanometer range in order to achieve near-theoretical performance and high yields.

Fabrication of gratings is generally accomplished in two main steps, (1) lithographic patterning into a photosensitive polymer resist, followed by (2) pattern transfer. A companion research program in this report entitled "Scanning Beam Interference Lithography" (previous page) describes progress in advanced grating patterning. In this abstract we report on research in pattern transfer technology. Development of a variety of grating geometries and materials is ongoing. Advanced gratings have been fabricated for 10 NASA missions, and further advances are sought for future missions [1]. Figure 1 depicts a gold wire-grid transmission grating designed for filtering deep-UV radiation for atom telescopes, while Figure 2 depicts a nano-imprinted sawtooth reflection grating for x-ray spectroscopy.

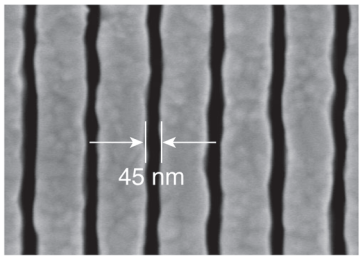

▲ Figure 1: Scanning electron micrograph of a deep-UV blocking grating used in atom telescopes on the NASA *IMAGE* and *TWINS* missions. The grating blocks deep-UV radiation while passing energetic neutral atoms.

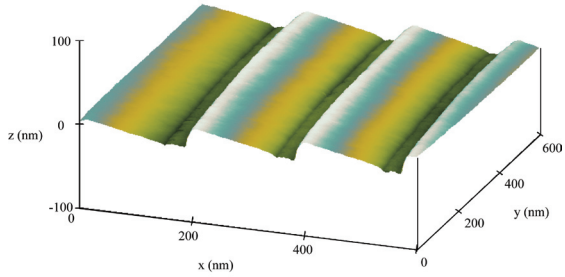

▲ Figure 2: AFM image of 200-nm-period nano-imprint grating with 7° blaze angle developed for the NASA *Constellation X* mission. The groove surfaces are extremely smooth with a RMS surface roughness of <0.2 nm.

REFERENCES

[1] M.L. Schattenburg, "From nanometers to gigaparsecs: the role of nanostructures in unraveling the mysteries of the cosmos," *J. Vacuum Sci. Technol. B,* vol. 19, pp. 2319-2328, 2001.

[2] C.-H. Chang, R.K. Heilmann, R.C. Fleming, J. Carter, E. Murphy, M.L. Schattenburg, T.C. Bailey, R.D. Frankel and R. Voisin, "Fabrication of saw-tooth diffraction gratings using nanoimprint lithography," *J. Vac. Sci. Technol. B,* vol. 21, pp. 2755-2759, 2003.

[3] C.-H. Chang, J.C. Montoya, M. Akilian, A. Lapsa, R.K. Heilmann, M.L. Schattenburg, M. Li, K.A. Flanagan, A.P. Rasmussen, J.F. Seely, J.M. Laming, B. Kjornrattanawanich and L.I. Goray, "High fidelity blazed grating replication using nanoimprint lithography," *J. Vac. Sci. Technol. B,* vol. 22, pp. 3260- 3264, 2004.

[4] M.P. Kowalski, R.K. Heilmann, M.L. Schattenburg, C.-H. Chang, F.B. Berendse and W.R. Hunter, "Near-normal-incidence extreme-ultraviolet efficiency of a flat crystalline anisotropically etched blazed grating," *App. Opt.,* vol. 45, pp. 1676-1679, 2006.

Nanometrology

R. Heilmann, J. Montoya, Y. Zhao, D. Trumper, M.L. Schattenburg
Sponsorship: NSF

Manufacturing of future nanodevices and systems will require accurate means to pattern, assemble, image and measure nanostructures. Unfortunately, the current state-of-the-art of dimensional metrology, based on the laser interferometer, is grossly inadequate for these tasks. While it is true that when used in carefully-controlled conditions interferometers can be very precise, they typically have an accuracy measured in microns rather than nanometers. Achieving high accuracy requires extraordinarily tight control of the environment and thus high cost. Manufacturing at the nanoscale will require new technology for dimensional metrology which enables sub-1 nm precision and accuracy in realistic factory environments.

A recently formed MIT-UNC–Charlotte team is developing new metrology technology based on large-area grating patterns that have long-range spatial-phase coherence and ultra-high accuracy. Our goal is to reduce errors in gratings by 10-100 times over the best available today. These improved gratings can be used to replace interferometers with positional encoders to measure stage motion in a new nanomanufacturing tools, and to calibrate the dimensional scales of existing nanofabrication tools. This increased precision and accuracy will enable the manufacturing of nanodevices and systems that are impossible to produce today. Improved dimensional accuracy at the nano-to-picometer scale will have a large impact in many nanotechnology disciplines including semiconductor manufacturing, integrated optics, precision machine tools and space research.

As part of this effort, we will utilize a unique and powerful tool recently developed at MIT called the nanoruler that can rapidly pattern large gratings with a precision well beyond other methods. Another unique high-precision tool, the UNCC-MIT-built sub-atomic measuring machine (SAMM), is being brought to bear to research new ways to quantify and reduce errors in the gratings.

Recent work at MIT is focused on improving the thermal controls in the Nanoruler lithography enclosure and developing an improved interferometer system to reduce errors in the stage metrology frame. At UNCC the SAMM is undergoing extensive refurbishment and improvements designed to boost interferometer accuracy.

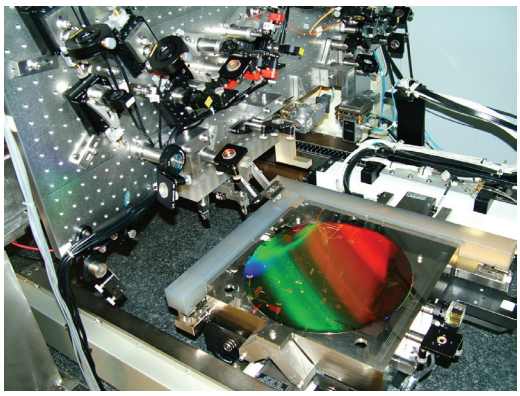

▲ Figure 1: Photograph of the Nanoruler lithography and metrology system built by MIT students. This unique tool is the most precise grating patterning and metrology system in the world.

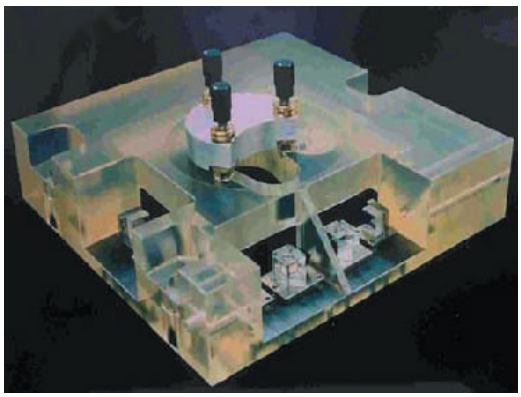

▲ Figure 2: Photograph of reference block/sample holder for the Sub-Atomic Measuring Machine at the University of North Carolina – Charlotte.

REFERENCES

[1] P. Konkola, C. Chen, R.K. Heilmann, C. Joo, J. Montoya, C.-H. Chang, and M.L. Schattenburg, "Nanometer-level repeatable metrology using the Nanoruler," *J. Vac. Sci. Technol. B,* vol. 21, pp. 3097-3101, 2003.

[2] R.K. Heilmann, C.G. Chen, P.T. Konkola and M.L. Schattenburg, "Dimensional metrology for nanometer-scale science and engineering: towards sub-nanometer accurate encoders," *Nanotechnology,* vol. 15, pp. S504-S511, 2004.

[3] J. Montoya, R.K. Heilmann and M.L. Schattenburg, "Measuring two-axis stage mirror non-flatness using linear/angular interferometers," *Proc. of the 19th Annual Meeting of the Am. Soc. for Precision Eng.*, vol. 34, pp. 382-385, 2004.

[4] Y. Zhao, C.-H. Chang, J. Montoya, R.K. Heilmann and M.L. Schattenburg, "Measurement of milli-degree temperature gradients in environmental enclosures," *Proc. of the 20th Annual Meeting of the Am. Soc. for Precision Eng.*, vol. 37, pp. 226-229, 2005.

Building Three-dimensional Nanostructures via Membrane Folding

W.J. Arora, A.J. Nichol, G. Barbastathis, H.I. Smith
Sponsorship: ISN

Nanostructured Origami™ describes a method of manufacturing three-dimensional (3D) nanostructures on a silicon wafer. Nanometer-scale structures are best fabricated with various two-dimensional (2D) lithography techniques. This project addresses the problem of building 3D structures using only 2D lithography. The general method of the Nanostructured Origami™ approach involves three steps: lithographically define micrometer-scale membranes and hinges; lithographically pattern nanostructures on these membranes; and release the membranes and actuate the hinges to fold into a 3D shape. Presently, we envision this technology to be well suited for fabrication of 3D photonic crystals and 3D diffractive optical devices.

We have developed a process to fold thin membranes of silicon nitride using stressed chromium hinges [1]. To date, these membranes have been patterned with gratings prior to being folded into 3D. However, arbitrary nanoscale features can be etched into or deposited onto the membranes. Experimental results are shown in Figures 1 and 2.

Current work focuses on reducing the radius of the folds. With the stressed chromium metal approach, we have demonstrated 30-μm-radius folds and by thinning the membrane at the hinge area, we predict that it is possible to achieve 5-μm-radius folds. However, it is desirable to have fold radii on the order of the membrane thickness, usually 1μm or less. We are developing a new folding approach that uses the stress gradient created by ion implantation. The maximum strain generated is proportional to the implanted ion concentration, which can be much larger than that generated by the stressed chromium. Additionally, as the ion implantation takes place, the hinge area is sputtered and can be controllably thinned. The combination of these effects results in a much smaller radius. Preliminary experimental results are shown in Figure 2.

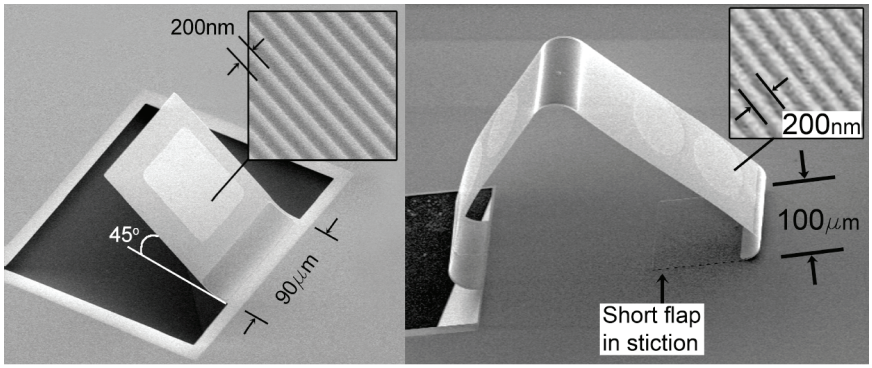

▲ Figure 1: a) A 200-nmSiN_x membrane folded to 45° with a grating etched into the center. The grating was patterned by interference lithography and the period is 200 nm. The membrane is folded near the base by a strip of chromium. The fold radius is 34 μm. b) Three identical hinges (63-μm long) each folded to 120^0 to form a triangular shape out of a long SiN_x strip. The membranes are patterned with interference lithography inside the circular regions. The fold radius is 32 μm.

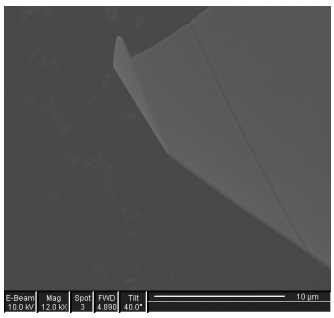

▲ Figure 2: Single pixel lines written with a focused ion beam source (Ga^+ ions, 30keV) folded a 200-nm-thick SiN membrane with a 500-nm radius. The folding strongly depends on the implanted dose; the line on the right had half the dose of the folded line on the left.

REFERENCES

[1] W.J. Arora, A.J. Nichol, H.I. Smith, and G. Barbastathis. "Membrane-folding to achieve three-dimensional nanostructures," *Appl. Phys. Lett., vol.* 88, p. 053108, 2006.

Fabrication of Nanostructured Optical Fiber-to-Chip Couplers

R. Barreto, M. Defosseux, T. Barwicz, A.M. Khilo, M. Fan, M.A. Popovic, P.T. Rakich, M. Dahlem, E.P. Ippen, F.X. Kaertner, H.I. Smith
Sponsorship: Pirelli S.p.A

Efficient fiber-to-chip coupling is a significant problem for high-index contrast micro-photonics due to the large difference in size and refractive index between the core of an optical fiber (several microns in diameter) and the core of a high-index-contrast waveguide (less than a micron wide). An efficient fiber-to-chip coupler is thus needed to match the mode of the fiber and transform it to a propagation mode inside the chip waveguide while minimizing signal loss. Our research simultaneously investigates and fabricates two different designs to accomplish the coupling. In the first design, called a horizontal coupler, a large polymer waveguide sits on a small silicon waveguide whose width tapers from 30 to 450 nm. This way, light is gradually transferred from the polymer waveguide to the silicon waveguide over the length of the tapered region. Figure 1 shows a cross-sectional area of the horizontal coupler. Fabrication is done on silicon-on-insulator wafers, so that the buried oxide functions as an under-cladding and prevents optical modes from reaching into the substrate. An over-cladding layer is also added to the structure to make the coupler compatible with other photonic devices, such as micro-ring-based reconfigurable optical add-drop filters. The second design, the vertical coupler, is based on a grating array composed of nanoscale tooth-sets that allow coupling from a vertically oriented fiber to a horizontally oriented waveguide. We are now demonstrating this concept using silicon-rich silicon nitride waveguides. Figure 2 shows a sketch of the vertical coupler design under fabrication. The minimum feature size reaches ~ 100 nm.

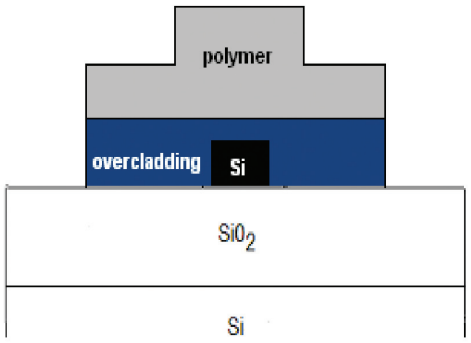

▲ Figure 1: Cross section of horizontal coupler.

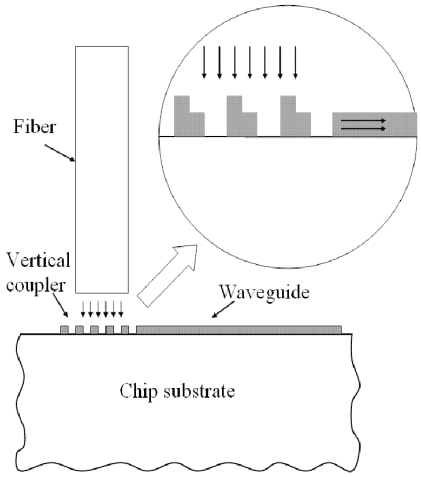

▲ Figure 2: Sketch of vertical coupler.

Polarization-insensitive Optical Add-drop Multiplexers in Silicon Nitride

T. Barwicz, M.R. Watts, M.A. Popovic, P.T. Rakich, E.P. Ippen, F.X. Kaertner, H.I. Smith
Sponsorship: Pirelli S.p.A

Microphotonics promises to revolutionize optics through miniaturization and dense integration of optical elements on planar surfaces. Of particular interest are microphotonic devices that employ high refractive-index contrast (HIC). These devices have dimensions on the order of the optical wavelength and functionality often not achievable with macro-scale devices. A long-standing criticism of HIC microphotonic devices, however, is their inherent sensitivity to polarization: they respond differently to light polarized along different axes. Since the polarization state changes randomly in optical fibers, HIC microphotonic devices are incompatible with the optical fibers necessary to connect them to the outside world.

In the Nanostructures Laboratory, we have developed nanofabrication techniques that allow the realization of microphotonic devices with unprecedented accuracy [1]. These techniques are based on scanning e-beam lithography and allow us to fabricate microring filters of unprecedented optical performance. Here, we overcome another major obstacle: sensitivity to polarization. We apply an integrated polarization-diversity scheme to render the optical response of microring filters insensitive to polarization. An optical add-drop multiplexer was realized and the polarization-dependent loss reduced to a remarkable average of 1 dB. Figure 1 presents the optical circuit diagram implemented and electron micrographs of the structure . The waveguides are based on silicon-rich silicon nitride and the critical dimensions vary from 70 to 3000 nm across the structure. The average waveguide widths of the 18 microrings forming the add-drop multiplexer are matched to 0.15 nm. The aspect ratio of the tallest and thinnest structures reaches 12 to 1.

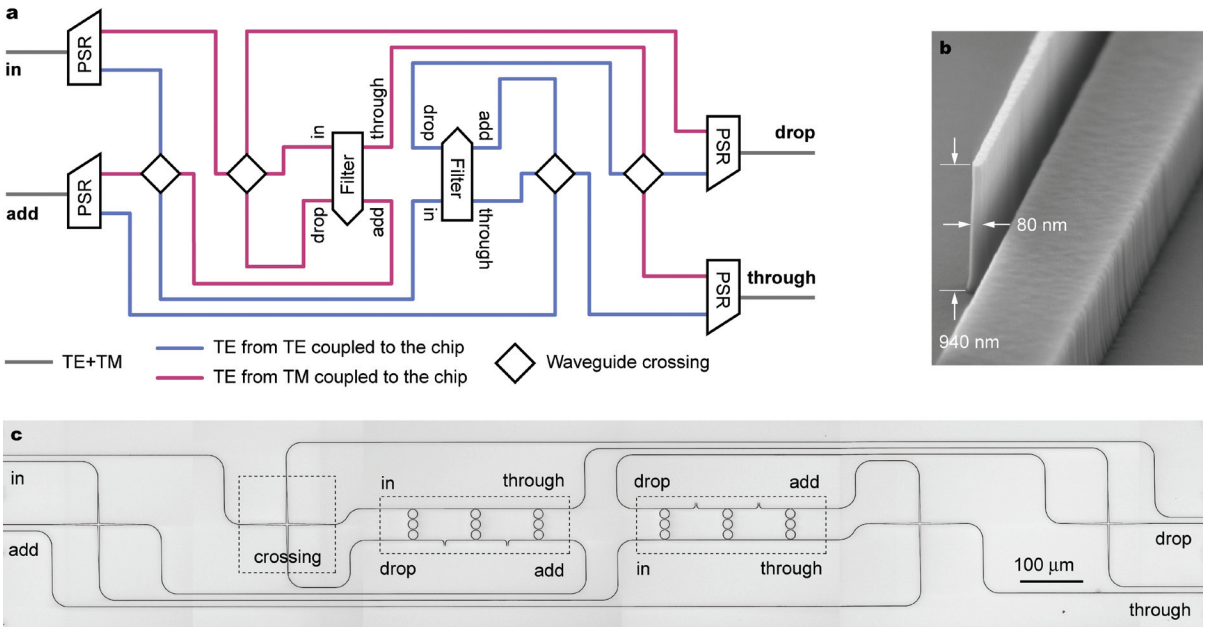

▲ Figure 1: (a) Optical circuit required to obtain a polarization insensitive optical response from polarization sensitive components. The acronym PSR stands for polarization splitter and rotator. The two filters shown in the schematic are identical. (b) Electron micrograph of the onset of the polarization splitter and rotator. (c) Electron micrograph of the middle part of the circuit. The polarization splitters and rotators are not shown and extend to the right and the left of the micrograph. The grayscale was inverted to allow the fine lines to be readable when printed.

REFERENCES

[1] T. Barwicz, M.A. Popovic, M.R. Watts, P.T. Rakich, E.P. Ippen, and H.I. Smith, "Fabrication of add-drop filters based on frequency-matched microring-resonators," *J. of Lightwave Technol.*, vol 24, pp. 2207-2218, 2006.

Nanofabrication of Reconfigurable Optical Add-drop Multiplexers in Silicon

T. Barwicz, M.A. Popovic, F. Gan, P.T. Rakich, M. Dahlem, E.P. Ippen, F.X. Kaertner, H.I. Smith
Sponsorship: Pirelli S.p.A

Reconfigurable optical add-drop multiplexers (ROADMs) are key components of modern optical networks. Data in optical fibers is carried at numerous wavelengths, which are also called channels. The ROADMs allow the rerouting (drop) of a subset of the data channels traveling in an optical fiber and replacing these with new data streams (add) that will be carried in the fiber at the previously rerouted wavelengths. "Reconfigurable" in ROADM indicates that the subset of dropped channels can be changed on the fly while the ROADM is in operation.

In our previous work, we developed nanofabrication techniques of unprecedented accuracy that allowed us to demonstrate in silicon-rich silicon nitride the most advanced microring filters reported [1-2]. In this work, we employ silicon microrings to take advantage of the high thermo-optical coefficient of silicon, allowing wide tuning of the wavelengths of operation of the ROADM with integrated heaters. Figure 2 presents a cross-sectional diagram of our implementation of a silicon waveguide with an integrated heater. Line-edge roughness is of critical concern in silicon waveguides as it translates into significant optical propagation loss via scattering of the guided mode. We found that the smoothest waveguides are obtained using hydrogen silsesquioxane (HSQ) as an e-beam resist and an etch-mask. Figure 1 presents an electron micrograph of a coupling region between a microring and a bus waveguide defined in HSQ. The patterning is based on scanning electron-beam lithography.

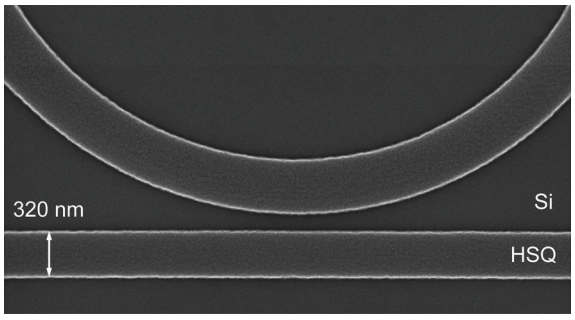

▲ Figure 1: Top-view electron micrograph of a coupling region defined in HSQ. Line-edge smoothness is critical for Si waveguides. The patterning is based on scanning electron beam lithography. The minimum feature size required is ~100 nm and must be controlled to ~ 5 nm.

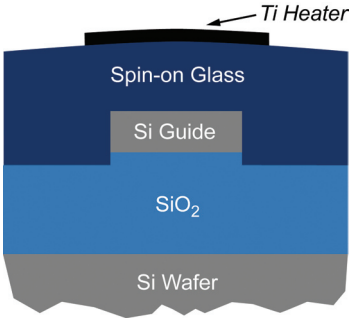

▲ Figure 2: Cross-sectional schematic of a silicon waveguide with an integrated titanium heater. Spin-on glass is used for the upper cladding of the waveguide to allow self-planarization and to avoid filling problems in narrow gaps.

REFERENCES

[1] M.A. Popovic, T. Barwicz, M.R. Watts, P.T. Rakich, L. Socci, E.P. Ippen, F.X. Kaertner, and H.I. Smith, "Multistage high-order microring-resonator add-drop filters," accepted for publication in *Optics Letters*.

[2] T. Barwicz, M.R. Watts, M.A. Popovic, P.T. Rakich, E.P. Ippen, F.X. Kaertner, and H.I. Smith, "Polarization-insensitive optical add-drop multiplexers in silicon nitride," Massachusetts Institute of Technology, Cambridge, MA, Microsystems Technology Laboratories Annual Research Report, 2006.

Nanofabrication of Optical Microring Filter Banks for Ultra-fast Analog-to-Digital Converters

C.W. Holzwarth, T. Barwicz, M.A. Popović, P.T. Rakich, E.P. Ippen, F.X. Kärtner, H.I. Smith
Sponsorship: DARPA

Microphotonic filter banks are an essential part of many proposed integrated photonic systems including ultra-fast analog-to-digital converters. Recent progress in designs and nanofabrication techniques for microring-resonators in high-index-contrast (HIC) materials have made possible the wide spectral spacing between resonances and low loss required for real world applications [1]. Achieving accurate resonant-frequency spacing of microring-filters is critical for these devices. In the NanoStructures Laboratory we have developed fabrication techniques based on scanning electron beam lithography (SEBL), that enables accurate control of the resonant-frequency spacing of HIC microring-resonator filter banks.

The resonant wavelength of a microring-resonator filter is given by $m*\lambda=n_{eff}*2\pi*R$, where λ is the resonant wavelength, n_{eff} is the effective index of refraction, R is the ring radius, and m is an integer. The effective index is controlled lithographically by controlling the width of the ring waveguide. Although it is simple to change both the width and the radius of the ring in the SEBL layout, this change is limited to discrete jumps corresponding to the step size of the SEBL system. In order to have 1 GHz control of the resonant frequency for the designed filters, the SEBL systems would need a step size of 30 pm. In our process this limitation of discrete step size is overcome by modulating the electron-beam dose to precisely control the width of the ring waveguide [2].

In our experiments second-order microring-resonator filters fabricated in silicon-rich silicon nitride were used in the microring filter banks (Figure 1a). Using dose modulation, eight-channel filter banks with channel spacing ranging from 90 to 180 GHz were fabricated and tested (Figure 1b). The results demonstrate that we can accurately control a 2.7 nm change in average width of the ring waveguide to 0.11 nm, despite a 6 nm step size in the SEBL system.

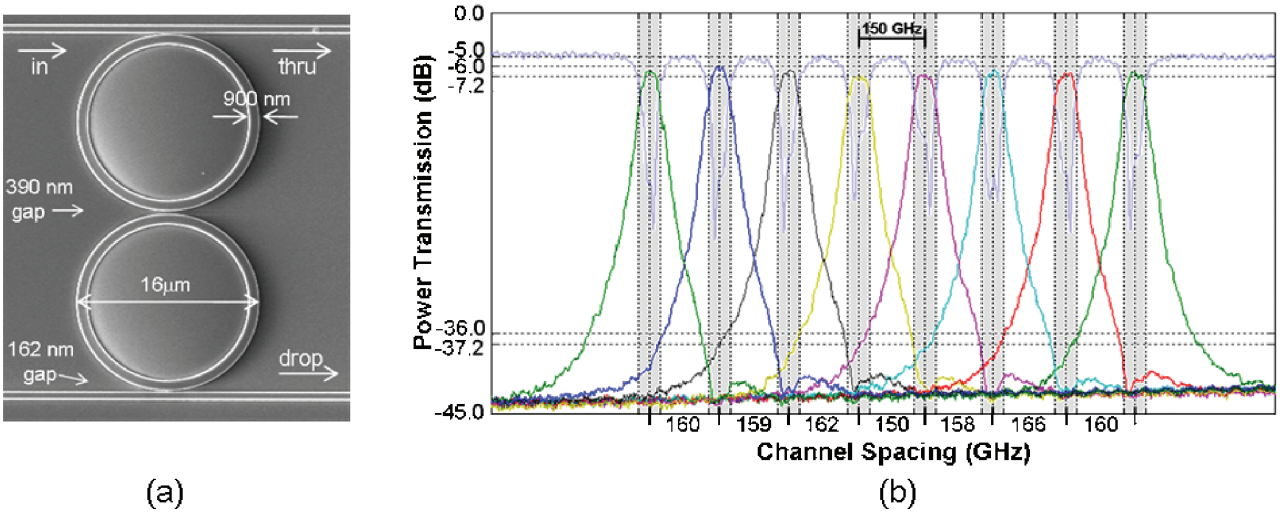

▲ Figure 1: a) Scanning electron micrograph of a fabricated second-order microring-resonator filter that has a 20 nm free spectral range, 50 GHz bandwidth and 1.5 ± 0.5 dB drop loss. b) Measured response of an eight-channel filter bank based on second-order microring-resonators with a target channel spacing for 150 GHz. The actual average channel spacing measured is 159 GHz (σ=5 GHz) and channel crosstalk is less than 30 dB.

REFERENCES

[1] T. Barwicz, M.A. Popović, P.T. Rakich, M.R. Watts, H.A. Haus, E.P. Ippen, H.I. Smith, "Microring-resonator-based add-drop filters in SiN: fabrication and analysis," *Optics Express*, vol. 12, no. 7, 2004.

[2] T. Barwicz, M.A. Popović, P.T. Rakich, M.R. Watts, F.X. Kaertner, E.P. Ippen, H.I. Smith, "Resonance-frequency control of high-index-contrast microphotonic cavities at fabrication," *Integrated Photonics Research and Applications 2006*, invited paper JWA3.

Imprint Lithography with Multilevel Alignment via Interferometric-Spatial-Phase Imaging

E.E. Moon, H.I. Smith
Sponsorship: Molecular Imprints, Inc.

A critical obstacle to widespread industrial acceptance of imprint lithography is the lack of capability for multilevel, nanometer-scale overlay. In journal articles [1-2] we described an alignment detection scheme, called interferometric-spatial-phase imaging (ISPI), which encodes alignment in the spatial phase disparity of complementary interference fringes, observed with oblique-incidence, long-working-distance, darkfield optical microscopes. We have applied ISPI to step-and-flash imprint lithography (S-FIL), in which alignment is actively measured and corrected with imprint fluid filling the template-substrate gap.

In S-FIL, it is desirable to use a shallow phase grating as the alignment mark, which raises the issue of ISPI fringe contrast. Fringe contrast with a fused silica phase grating in an imprint fluid is reduced to 12% of the fringe contrast with air in the template-substrate gap, as predicted by two-dimensional finite-difference time-domain (FDTD) simulations and confirmed by experiment. Despite the low fringe contrast, experimental data (Figure 1) indicate the ability of ISPI to achieve sub-nanometer alignment detectivity under such conditions, the most stringent typically encountered in imprint lithography.

Figure 2 illustrates the ability of ISPI to effect dynamic alignment control throughout the S-FIL imprint process. The data shows an initial condition with alignment well below 1 nm. Alignment is disturbed by a mechanical impulse from opening of the UV shutter, but ISPI can observe and correct such disturbances, which would usually pass unnoticed. We believe these experiments, among others, indicate that ISPI is uniquely advantaged for application to S-FIL and other forms of imprint lithography.

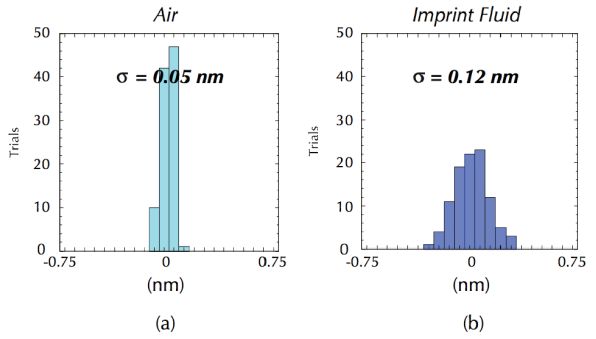

▲ Figure 1: Alignment detectivity of ISPI with (a) air in the template-substrate gap (σ = 0.05 nm), and (b) imprint fluid in the gap (σ = 0.12 nm). Detectivity is reduced in the stringent case of phase gratings on the template, used with an imprint fluid of similar index of refraction, but remains within the sub-nanometer range. The template-substrate gap was mechanically locked during the experiment.

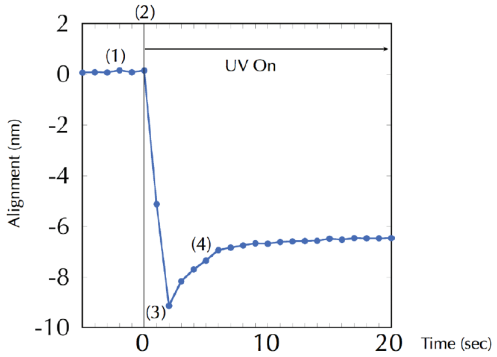

▲ Figure 2: Plot of ISPI alignment data (1) before exposure, (2) at the instant the shutter to the UV lamp opens, (3) during misalignment caused by a mechanical shock transmitted from the UV lamp to the template, and (4) during correction of misalignment, until crosslinking solidifies the imprint material. The experiment demonstrates the ability of ISPI to detect and identify sources of misalignment on the nanometer level, as well as a limited ability to re-align during crosslinking of the imprint material. Improvements are readily achievable with increased feedback bandwidth.

REFERENCES

[1] E.E. Moon, L. Chen, P.N. Everett, M.K. Mondol, and H.I. Smith, "Interferometric-spatial-phase imaging for six-axis mask control," *J. Vac. Sci. Technol. B*, vol. 21, p. 3112, 2003.

[2] E.E. Moon, M.K. Mondol, P.N. Everett, and H.I. Smith, "Dynamic alignment control for fluid-immersion lithographies using interferometric-spatial-phase imaging," *J. Vac. Sci. Technol. B*, vol. 23, p. 2607, 2005.

Interference Lithography

T.B. O'Reilly, T. Savas, H.I. Smith
Sponsorship: Internal funds

Interference lithography (IL) is a means to produce periodic structures using the coherent interference of light. Typically, light from a source is divided and recombined, forming a periodic intensity pattern that can be used to expose a photosensitive substrate. The NanoStructures Lab (NSL) has been developing interference lithography systems since the mid 1970s, and operates a range of tools capable of writing gratings, grids, and other periodic structures with periods as fine as 100 nm; these structures are used in a wide variety of research areas.

Two of the NSL's IL systems use 325 nm wavelength HeCd lasers. The most flexible and widely used of these systems is known as the Lloyd's mirror. This system is a half Mach-Zehnder interferometer that is easily configured to write patterns with periods from 170 nm to several microns. A second system at the same wavelength in a full Mach-Zehnder configuration can write gratings over larger areas than the Lloyd's mirror system, but is less flexible. Finally, the NSL operates an achromatic interference lithography (AIL) system. This system uses a 193 nm excimer laser and can write patterns with periods of 100 nm, as shown in Figure 1. This AIL system uses phase gratings to split and recombine the light, and can form high-contrast fringe patterns whose area is not dependent on the spatial or temporal coherence of the source.

Gratings produced by the Lloyd's mirror have been used to cut carbon nanotubes, guide the assembly of nanoparticles for templated self-assembly, study the behavior of strained-silicon wafers, fabricate templates for imprint lithography, and more. The full Mach-Zehnder system has been used to study in-plane distortion of silicon nitride membranes and to create super-prisms and super-collimators based on 2D photonic crystals. The AIL system has been used to create free-standing gratings used in atom-beam interference experiments and EUV spectroscopy.

In addition, the NSL collaborates with the Space Nanotechnology Laboratory, which operates a Mach-Zehnder IL system and the Nanoruler, an IL system that can write high-quality gratings over areas larger than 300 mm in diameter.

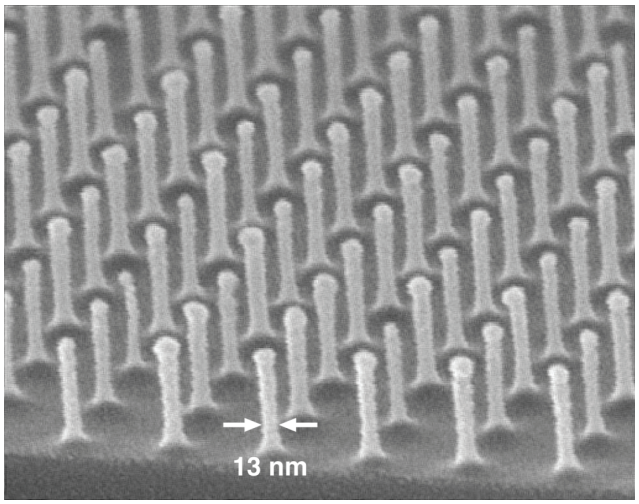

▲ Figure 1: Scanning electron micrograph of a 100 nm-period grid, exposed in PMMA on top of an antireflection coating and transferred into Si by reactive ion etching.

Immersion-Achromatic-Interference Lithography

T.B. O'Reilly, M. Walsh, T. Savas, H.I. Smith
Sponsorship: Singapore-MIT Alliance

Interference lithography is a means of using the coherent interference of light to create periodic structures. The period of the pattern written is determined by the interference angle, θ, and the wavelength, λ, according to the equation $P = \lambda/2n\sin(\theta)$. Since an upper limit exists for the interference angle (90°), to reduce the period below half the wavelength it is necessary to use an immersion fluid to reduce the effective wavelength of the light. The NanoStructures Lab is developing an immersion interference lithography system that will be capable of writing gratings with periods of 70 nm or even smaller.

The system under development, shown in Figure 1, is an achromatic grating interferometer similar to an existing system that is used to write 100 nm period gratings. In this system, diffraction gratings split and recombine light. The gratings are configured in such a way that contrast of the fringe pattern formed is not dependent on the spatial or temporal coherence of the source. Analysis of the proposed system has shown that it will be capable of writing gratings with periods as fine as 70 nm, over areas as large as the parent gratings, using water as the immersion fluid. Using higher-index immersion fluids, it should be possible to write patterns as fine as 60 nm.

Gratings produced by this system are likely to find application in areas such as atom interferometers and templated self-assembly. In addition, the system will be used to study the performance of photoresists and immersion fluids at very high numerical apertures.

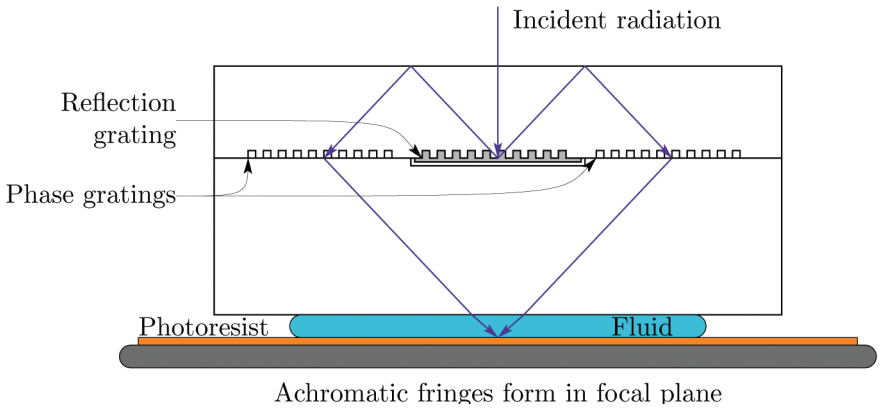

▲ Figure 1: Immersion grating-interference lithography system.

Three-dimensional Photonic Crystals by Membrane Assembly

A. Patel, J.D. Joannopoulos, H.I. Smith
Sponsorship: NSF

A three-dimensional photonic crystal is a periodic structure in which back-diffraction prevents light within a given wavelength band (the bandgap) from propagating in any direction. A local deviation from perfect periodicity (a "defect") such as some missing material, i.e., a hole, or a local change in dimensions, can produce a photon trap or resonant cavity. Light cannot propagate through the photonic crystal but it can remain localized around the defect, leading to resonators of extraordinarily high Q. This phenomenon promises many practical applications, including single-photon sources and highly sensitive chemical detection. A line defect, such as a row of missing material, can serve as a lossless waveguide, leading to highly complex and functional photonic systems. Figure 1 [1] depicts a 3D photonic crystal with a very large omni-directional bandgap. In the past, we fabricated this type of structure using a layer-by-layer process composed of e-beam lithography followed by deposition and etch back [2]. We are replacing this tedious and error-prone process with layer-by-layer assembly of membranes that are pre-patterned using interference lithography, as depicted in Figure 2. Although this technique will require the development of entirely new membrane fabrication and assembly techniques, it should reduce the probability of error since the membranes are separately fabricated and inspected and assembled only at the final step.

Large area SiN membranes (1 cm x 1 cm), 350-nm thick, have been patterned with the appropriate 2D periodic structure. We are developing techniques for assembling such membranes with ~10 nm alignment accuracy. In the future Si membranes will be investigated. Ultimately we plan to assemble more than 20 layers in a 3D photonic crystal structure.

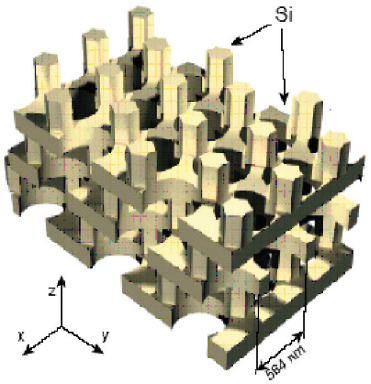

▲ Figure 1: A 3-D rendering of the photonic crystal structure to be fabricated. The picture depicts a crystal with 6 layers. Ultimately, we will assemble 20+ layers.

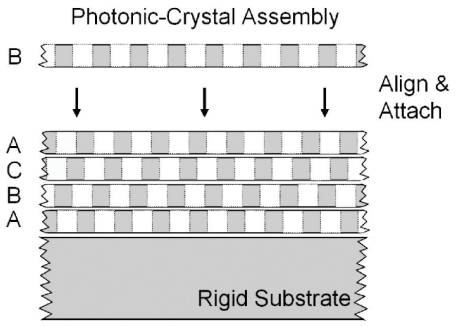

▲ Figure 2: Proposed membrane-assembly process for fabricating 3D photonic crystals.

REFERENCES

[1] S.G. Johnson and J.D. Joannopoulos, "Three-dimensional period dielectric layered structure with omni-directional photonic band gap," *App. Phys. Lett*, vol. 77, p. 3490, 2000.

[2] M.Qi, E. Lidorikis, P.T. Rakich, S.G. Johnson, J.D. Joannopoulos, E.P. Ippen, and H.I. Smith, "A three-dimensional optical photonic crystal with designed point defects," *Nature*, vol. 429, pp. 538-542, 2004.

Absorbance-Modulation Optical Lithography

R. Menon, S. Tsai, H.I. Smith
Sponsorship: Internal funds

In the NanoStructures laboratory, we are developing an optical nano patterning technology that can push the resolution limits to sub-diffraction-limited regimes using photochromic molecules. Photochromic molecules are those that reversibly change their absorbance spectra upon irradiation [1]. By placing a thin photochromic layer on top of a traditional photoresist, coupled with a two-wavelength illumination, one can pattern sub-diffraction-limited features (~ $\lambda/13$) [2]. The first wavelength, λ_1, bleaches the photochromic layer, turning it transparent, while the second longer wavelength, λ_2, reverses this bleaching process. The two-wavelength scheme, which we call absorbance-modulation-optical lithography (AMOL), uses a focused beam at λ_1 and a ring-shaped beam at λ_2. As a result, the beam transmitted through the photochromic layer is compressed laterally.

Thus, AMOL has the potential to pattern 30 nm features at λ_1 = 400 nm. Compared to scanning electron beam lithography (SEBL), AMOL has the advantages of higher accuracy, higher throughput (via parallel beams [3]), non-damaging effects (for organic and other sensitive substrates), and a fundamentally simpler configuration.

Furthermore, it can be shown that if both isomers of the photochromic molecule are stable, the compression of the transmitted beam is dependent on the ratio of the intensities at λ_1 and λ_2, not on either one alone. This has the important practical implication that highly compressed beams may be created at low power densities. The scale of the compression of the transmitted beam is determined by the initial absorbance of the photochromic layer as well as the difference between the initial and final absorbances, i.e., the contrast of the absorbance modulation. Figure 1 shows the predicted resolution improvement achievable with AMOL.

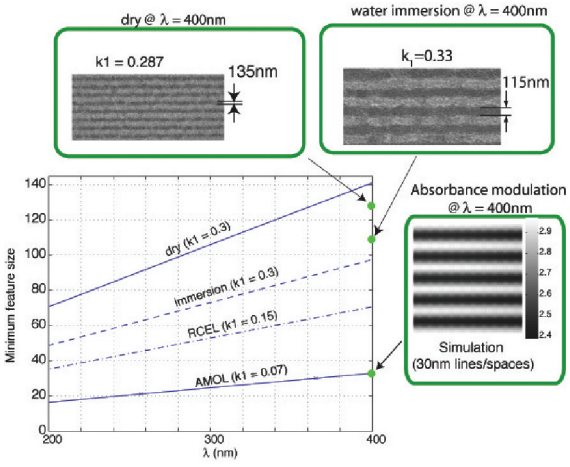

◀ Figure 1: Resolution scaling with wavelength for different technologies. Note that AMOL has the potential to extend optical nano patterning to the sub-30-nm regime.

REFERENCES

[1] J.C. Crano and R.J. Guglielmetti, Eds., *Organic Photochromic and Thermochromic Compounds*. New York: Plenum Press, 1999.
[2] R. Menon and H.I. Smith, "Absorbance-modulation-optical lithography (AMOL)," *J. Opt. Soc. Am. A*, to be published.
[3] R. Menon, A. Patel, D. Gil and H.I. Smith, "Maskless lithography," *Materials Today*, vol. 8, no. 2, pp. 26-33, Feb. 2005.

Zone-Plate-Array Lithography (ZPAL)

R. Menon, S. Tsai, H.I. Smith
Sponsorship: DARPA, NSF

Optical projection lithography (OPL) has been the key element in the technological progress of the semiconductor industry. In OPL, a fixed pattern on a photomask is imaged onto a photoresist-coated substrate by means of a complex and expensive optical system. Resolution-enhancement techniques used to print at the diffraction-limit often constrain the geometries of these patterns. Furthermore, OPL is inherently inflexible since the patterns once defined in the photomask cannot be changed. Obtaining a new set of photomasks is an expensive and time-consuming proposition. This requirement is a significant impediment in emerging applications, in which frequent experimentation and changes to pattern geometries are often essential to achieving the optimum design.

In order to address these issues, in the NanoStructures laboratory at MIT, we have developed an optical-maskless lithography called zone-plate-array lithography (ZPAL) [1] that uses a massively parallel array of tightly focused laser beamlets to create patterns of complex geometries in a dot-matrix fashion. The array of beamlets is created by an array of high-numerical aperture zone plates. The illumination of each zone plate is controlled by one pixel on an upstream spatial-light modulator. This technology is currently being commercialized by LumArray Inc. [2].

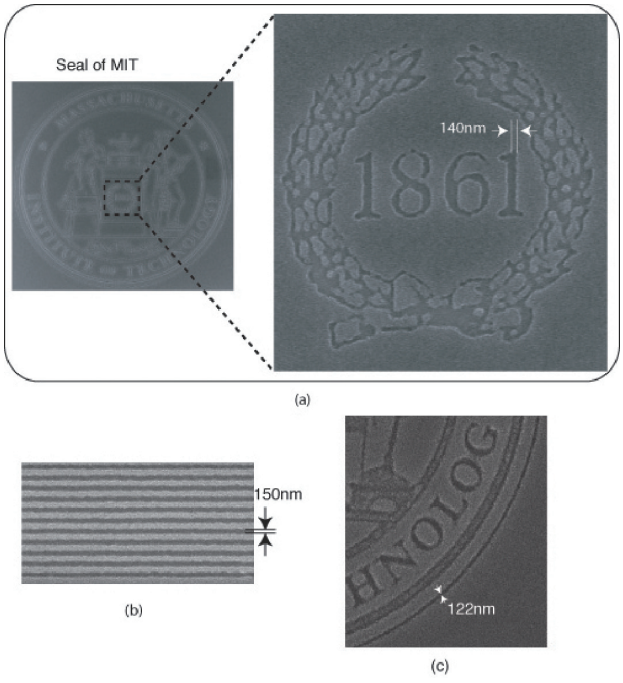

▲ Figure 1: Scanning electron micrographs of patterns created using ZPAL at an exposure wavelength of l = 400 nm.

REFERENCES:

[1] R. Menon, A. Patel, D. Gil, and H.I. Smith, "Maskless Lithography," *Materials Today*, pp. 26-33, Feb. 2005.
[2] LumArray [Online]. Available: http://www.lumarray.com

Spatial-phase-locked E-beam Lithography

H.I. Smith, F. Zhang, M. Mondol
Sponsorship: No external sponsor

Our research in spatial-phase-locked electron-beam lithography (SPLEBL) is aimed at reducing pattern-placement errors in electron-beam-lithography systems to the 1nm level. Such high precision is essential for a variety of future lithographic applications. SPLEBL is currently the only approach capable of achieving such accuracy. As shown in Figure 1, SPLEBL uses a periodic signal, derived from the interaction of the scanning e-beam with a fiducial grid on the substrate, to continuously track the position of the beam while patterns are being written. Any deviation of the beam from its intended location on the substrate is sensed, and corrections are fed back to the beam-control electronics to cancel errors in the beam's position. In this manner, the locations of patterns are directly registered to the fiducial grid on the substrate.

The research effort focuses on developing the three critical components of SPLEBL: 1) the beam-position-detection algorithm [1], 2) a user-friendly-fabrication process for the fiducial grid [2], and 3) a beam-current-modulation scheme [3]. The last component is necessary for the SPLEBL-enabled tool to discriminate between non-exposed and exposed areas while enjoying a continuous feedback signal.

SPLEBL in its continuous-feedback mode has been implemented on a Raith150 scanning e-beam lithography system (an inexpensive system that provides sub-20-nm patterning resolution). In this implementation, a thin (<10 nm) metallic fiducial grid is placed on top of the e-beam resist. During exposure, a periodically varying secondary-electron (SE) signal is produced as a result of the interaction between the electron beam and the metal reference grid. Its limited thickness makes the grid layer essentially transparent to the primary electron-beam. The beam position is determined in real time by a detection algorithm based on Fourier technique. This implementation allowed the beam position to be monitored constantlyand corrected during exposure. Experimental results [1] shown in Figure 2 indicate that 1-nm-level placement accuracy is achievable with this technology.

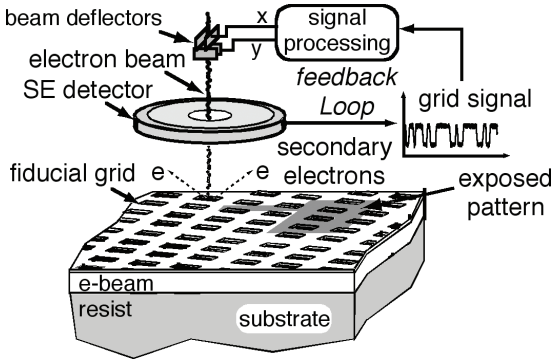

▲ Figure 1: Schematic of the global-fiducial-grid mode of spatial-phase-locked electron-beam lithography. The periodic signal detected from the fiducial grid, which includes both X and Y components, is used to measure placement error, and a correction signal is fed back to the beam-deflection system.

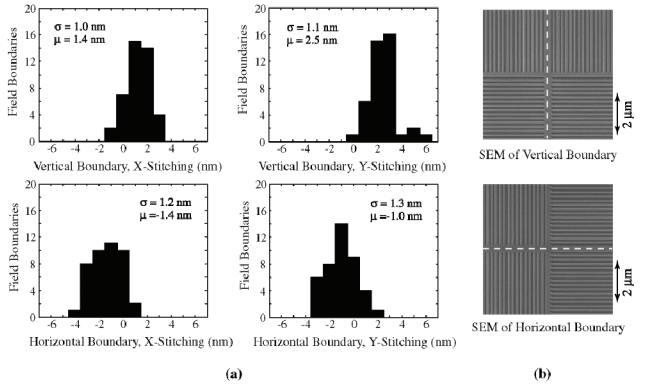

▲ Figure 2: (a) Histograms showing x- and y-stitching measurements at all 84 field boundaries of 49 stitched fields. Spatial-phase locking has reduced the standard deviation of the stitching errors to below 1.3 nm. (b) Sample 200-nm period stitched grating patterns. The dashed line indicates the field boundary.

REFERENCES

[1] J.T. Hastings, F. Zhang, and H.I. Smith, "Nanometer-level stitching in raster-scanning e-beam lithography using spatial-phase locking," *J. Vac. Sci. Technol. B*, vol. 21, no. 6, pp. 2650-2656, Nov/Dec 2003.

[2] F. Zhang, H.I. Smith and J.F. Dai, "Fabrication of high-secondary-electron-yield grids for spatial-phase-locked electron-beam lithography," *J. Vac. Sci. Technol. B*, vol. 23, no. 6, pp. 3061-3064, Nov/Dec 2005.

[3] F. Zhang and H.I. Smith, "Partial blanking of an electron beam using a quadrupole lens," in *J. Vac. Sci. Technol. B*, vol. 23, no. 1, pp. 133-137, Jan/Feb 2005.

Controlled Assembly of 20-nm-diameter Gold Nanoparticles into Nanogaps using AC Dielectrophoresis

R. Barsotti, M. Vahey, R. Wartena, J. Voldman, Y. Chiang, F. Stellacci
Sponsorship: Singapore-MIT Alliance, NDSEG Fellowship

The directed assembly of nano-objects into specific locations will allow for the fabrication of electronic devices that utilize the unique properties of the nano-objects. One method to assemble nano-objects into gaps uses the dielectrophorectic (DEP) force via the application of an alternating field [1-2]. Here, we demonstrate the assembly of gold nanoparticles into nanogaps (15-100 nm in width) that are fabricated by electron beam lithography. Nanoparticle assembly is achieved by applying an AC field across the nanogaps after a drop of an aqueous solution of gold nanoparticles has been placed over the device. The assembly is characterized by SEM, AFM, and post-assembly electrical measurements. The number of nanoparticles that assemble in the gap is studied as a function of the applied AC field, the concentration of the nanoparticle solution, and assembly time with a goal of the assembly of a single particle in a gap. Pre-assembly modification of the gold surfaces using a dithiol self-assembled monolayer results in a significant increase in DEP assembly as the surface-bound thiol groups bind the gold particles to the substrate. Theoretical modeling of the dielectrophorectic force on nanoparticles in comparison to their thermal motion is used to predict the experimental conditions for the assembly of a single particle.

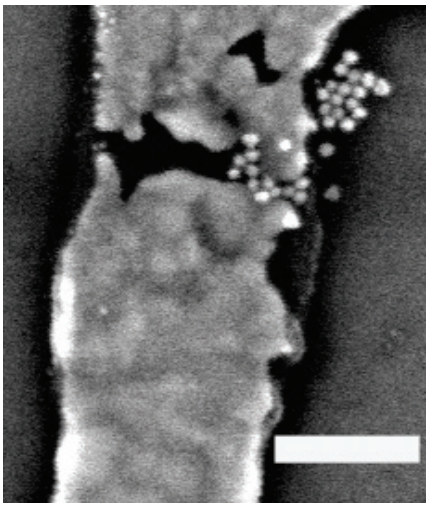

▲ Figure 1: An SEM image of assembly of citrate-stabilized 20-nm-diameter gold particles by the application of a 2-V_{pp}, 1-MHz alternating field across a 23-nm gap for 120 seconds. A solution concentration of 7 * 10^{10} particles/ml was used for this assembly. Scale bar=200 nm.

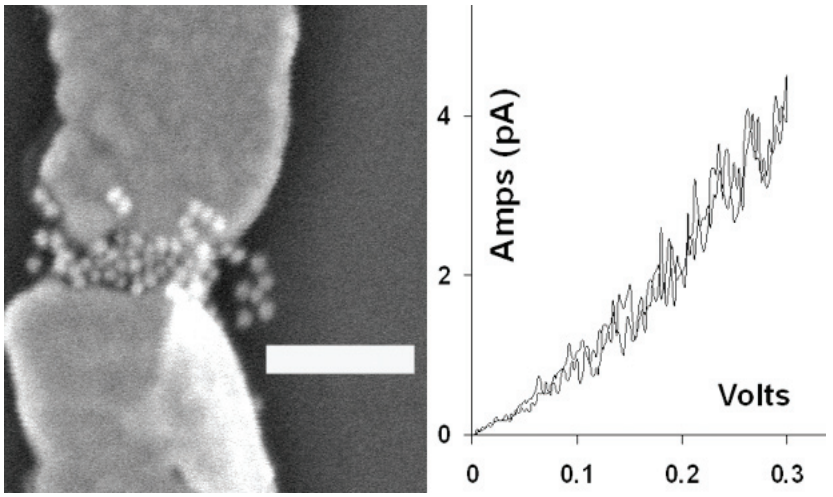

▲ Figure 2: An SEM image showing increased nanoparticle assembly at 3 V_{pp} for 120 seconds. Scale bar=200 nm. The IV characteristics of the assembly show a 100-fold increase in conductance after particle assembly. The electrical characteristics remain stable after 20 voltage sweeps.

REFERENCES

[1] I. Amlani, A.M. Rawlett, L.A. Nagahara, and R.K. Tsui, "Hybrid assembly technique using alternating current field for molecular electronic measurements," *J. of Vacuum Science and Tech. B*, vol. 20, no. 6, pp. 2802-2805, 2002.

[2] S.I. Khondaker and Z. Yao, "Fabrication of nanometer-spaced electrodes using gold nanoparticles," *App. Phys. Lett.*, vol. 81, no. 24, pp. 4613-4615, 2002.

Carbon Nanotube Assembly for Interconnect and Device Applications

T.M. Wu, B. Long, B. Wunsch, F. Stellacci
Sponsorship: MARCO IFC

Carbon nanotubes (CNTs) are materials with potentially useful electronic, thermal, and mechanical properties. Our current work with CNTs focuses on applications in the microelectronics arena, especially use as a substitute for conventional metal interconnects. As interconnect dimensions shrink, surface scattering begins to contribute dramatically to line resistance, leading to power loss and signal delay. The CNTs, with length-independent conductivity due to ballistic transport, offer a potential solution.

We are investigating currently methods to accurately and precisely construct CNT structures on surfaces via assembly from a suspension or solution. We use a series of chemical and physical interactions to direct the assembly of CNTs onto desired locations on a substrate. In the chemical sense, we can tune the interaction between CNTs and a surface by selectively growing polar and non-polar monolayer patterns on the substrate. In the physical sense, we can pattern the growth of the monolayer and of the CNT deposition by lithographic methods such as electron-beam writing and dip-pen nanolithography. By combining these two approaches, we hope to develop an integrated system for the massively parallel and accurate assembly of CNTs on a surface.

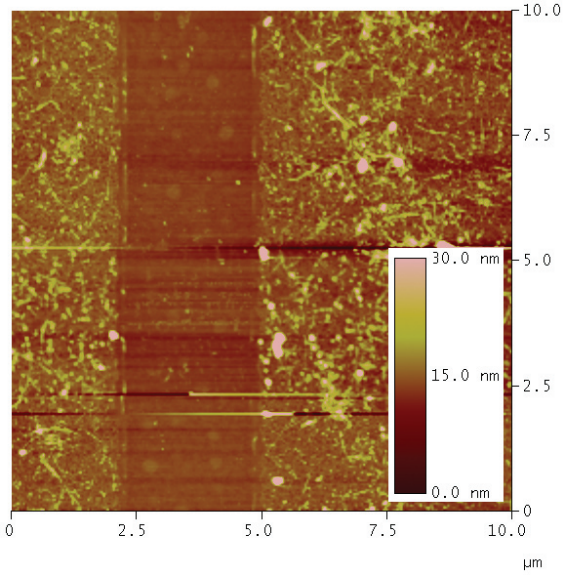

▲ Figure 1: Chemically-directed assembly of CNTs on polar and non-polar silane monolayers. The CNTs assemble on the polar monolayers (sides) and are repelled by the nonpolar monolayer (stripe).

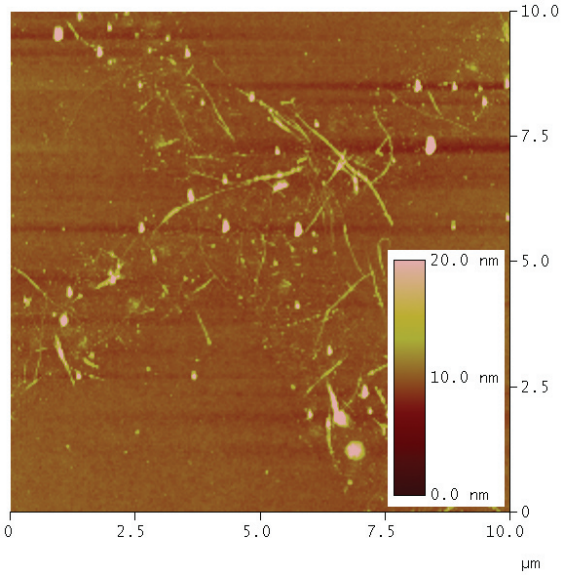

▲ Figure 2: Lithographically-directed assembly of CNTs on a polar silane monolayer. The resist was patterned with electron beam lithography and served as a liftoff mask for CNT deposition from solution.

Catalyst Engineering and Nanowire Growth Mechanisms

S. Boles, O. Nayfeh, E.A. Fitzgerald, D.A. Antoniadis, C.V. Thompson
Sponsorship: Singapore-MIT Alliance

The use of semiconductor nanowires for electronic and photonic applications has generated a great deal of interest in recent years, due to their mechanical, electronic, and photonic properties. A great deal of effort has been focused on demonstrating the unique properties of nanowires, while there has been less interest in developing techniques that allow growth of functional arrays of nanowires. Our research focuses on creating high-density nanowire arrays by controlling the metallic dots that catalyze wire growth through the vapor-liquid-solid mechanism. Our early work has focused on the development of a baseline growth process using disordered catalyst arrays, as show in Figure 1. Future work will involve growth on catalysts ordered through templated self-assembly techniques. Our ultimate goal is to grow ordered arrays that can be included in electronic and photonic device structures that will allow detailed correlations among the techniques of growth and the properties of nanowires.

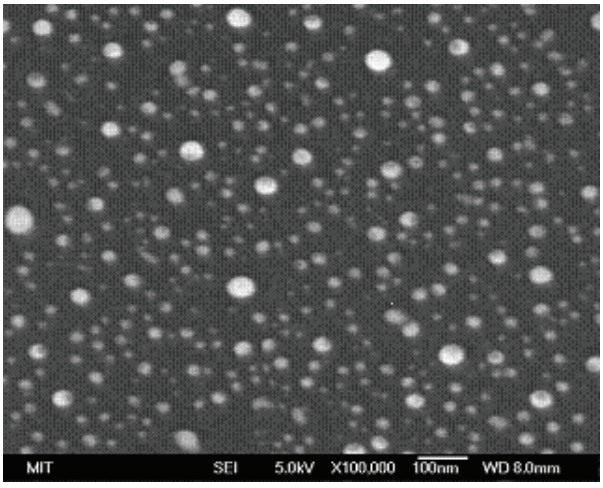

▲ Figure 1: Au particles produced by dewetting of 0.3nm-thick Au film at 550 C on a <111> silicon substrate.

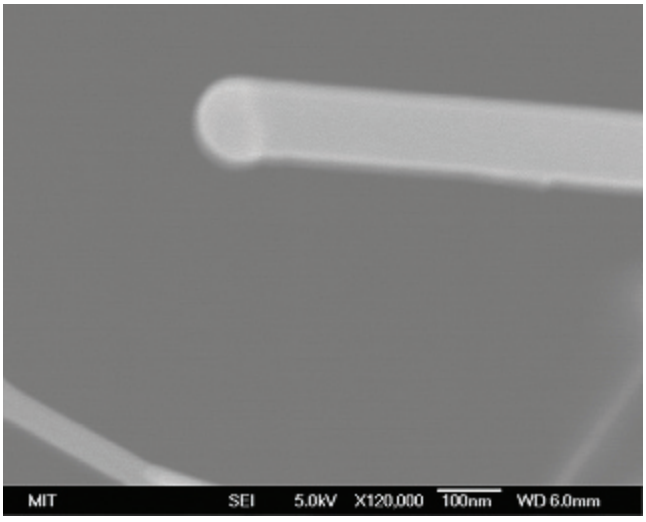

▲ Figure 2: Silicon nanowire grown by MOCVD using a Au catalyst on <111> Si substrate. The Au particle remains at the top of the wire and controls the diameter of the growing wire.

Templated Self-Assembly for Nano-particle Organization: Solid State Dewetting

A.L. Giermann, J. Ye, R. Mönig, C.V. Thompson
Sponsorship: NSF, Singapore-MIT Alliance

We are exploring solid-state dewetting of thin films as a tool for producing ordered arrays of metal nanodots over large areas. Such arrays may be interesting in memory or plasmonic applications and for use as catalysts for the growth of carbon nanotube or semiconductor nanowire arrays. Our current investigations focus on two topics: 1) the effects of materials anisotropies on dewetting; and 2) the effects of physical templates to control dewetting.

In the area of materials anisotropies, we seek a material system in which the islands formed by dewetting exhibit spatial order due to anisotropy in the surface energies and diffusivities. As an initial step, we observed significantly different dewetting behaviors of Ni thin films on MgO substrates, depending on the crystallographic orientation of the substrate surface. Our future work will involve investigating how micro-faceting of MgO affects the dewetting behaviors of Ni thin films.

In the area of physical templating, we use topographically patterned substrates to modulate the curvature of as-deposited films and thus influence the dewetting behavior of polycrystalline films [1]. We deposit and anneal gold films on di-periodic arrays of pits on oxidized silicon substrates to induce one-to-one self-assembly of ordered arrays of gold particles over large areas. Average particles sizes of less than 50 nm can be achieved. Compared to dewetting on flat substrates, the templates impose a significant decrease in average particle size, as well as ensure a narrow size and spatial distribution (Figure 1). This templating technique uniquely results in crystallographic ordering (i.e., graphoepitaxy) of the particles, imposing an in-plane texture and changing the out-of-plane texture (Figure 2). Particles formed in topographic features are expected to be stable with respect to agglomeration during growth of tubes or wires. Our current efforts include investigating additional techniques for imposing topographic templating on thin films; exploring the templating phenomena in other materials, including those that are known to catalyze carbon nanotubes and those with high surface mobilities; and developing numeric models of topographic dewetting in order to fully characterize the mechanism.

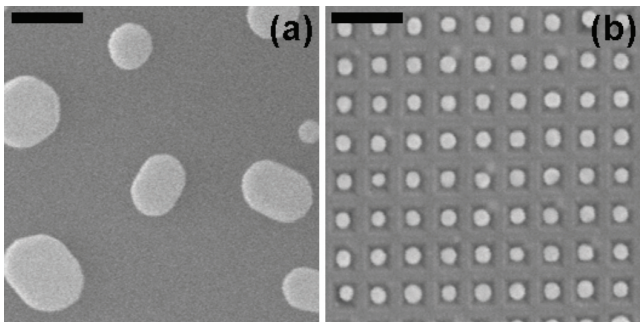

▲ Figure 1: The effect of topography on particle morphology. The results of dewetting a 10-nm-thick Au film on (a) a flat substrate and (b) a topographic substrate. Micrographs are displayed at the same magnification to emphasize the effect of topography on particle size. Scale bars are 200 nm in length.

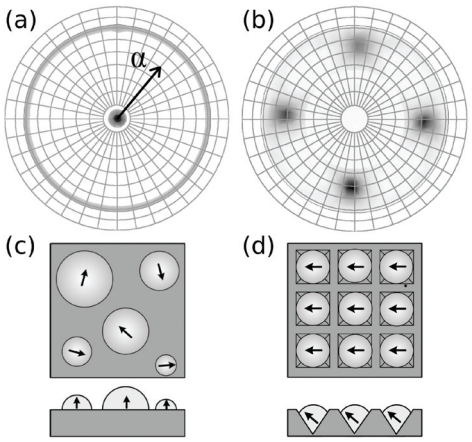

▲ Figure 2: The effect of topography on particle orientation. (a) and (b) show Au <111> X-ray pole figures ($37.4^\circ < 2\theta < 38.6^\circ$), (a) for particles on a flat substrate and (b) for particles on a topographic substrate. (c) and (d) schematically illustrate the particle orientation on flat and topographic substrates, respectively. The arrows indicate the <111> projection.

REFERENCES

[1] A.L. Giermann and C.V. Thompson, "Solid-state dewetting for ordered arrays of crystallographically oriented metal particles," *App. Phys. Lett.*, vol. 86, p. 121903, Mar. 2005.

Catalyst Engineering and Carbon Nanotube Growth Mechanisms

G.D. Nessim, J S. Kim, D. Acquaviva, A.J. Hart, C.V. Thompson
Sponsorship: MARCO IFC, Singapore-MIT Alliance

In addition to having many other applications in electronics and biology, carbon nanotubes (CNTs) are good substitutes for copper interconnects in integrated circuits. However, a significant challenge is the ability to control the density, type, size, and position of the nanotubes to be used as interconnects. These CNTs must also be grown on conductive substrates to achieve ohmic contact. Our approach to these challenges is to study and engineer catalysts in order to obtain CNTs with the required properties.

We initially studied nanotube growth with an iron catalyst on alumina underlayers using thermal chemical vapor deposition (CVD) and analyzed the influence of parameters such as catalyst size, temperature, reactant partial pressure, gas flow rate, timing of introduction of a reducing gas, pre-deposition annealing, and growth time. We have determined a range of conditions in which the growth of dense carpets of vertically aligned CNTs of different height, up to 1 mm (Figures 1 and 2), is possible. Characterization of the resulting CNTs with SEM, TEM, and AFM is underway.

We also started a series of experiments involving growth of CNTs with catalysts on conductive underlayers. This process is more challenging as evidenced by the very few successful reports of CNT growth directly on conductive substrates. With rapid heating of the samples prior to thermal CVD, we have grown CNTs as a mesh of CNTs ("spaghetti," not a regular carpet of CNTs). Preliminary measurements indicate that electrical conductivity exists between the nanotubes and the substrate.

Our next step is to grow CNTs on conductive underlayers inside a matrix of regularly spaced pores in an insulating overlayer, e.g., ordered porous alumina scaffolds developed in our group. Using this method we will measure and analyze the characteristics of regular arrays of individual multi-wall CNTs and bundles of CNTs with near-uniform dimensions.

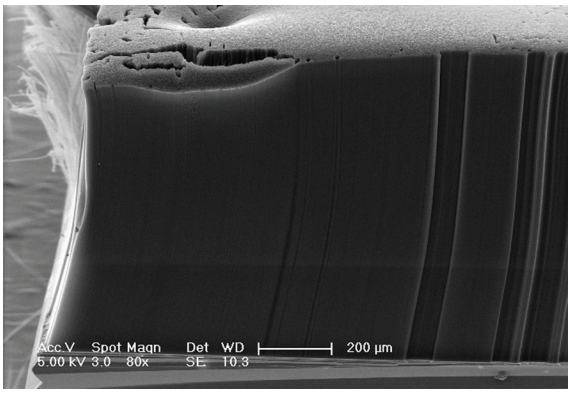

▲ Figure 1: Dense carpet of carbon nanotubes grown using thermal chemical vapor deposition (catalyst Fe/Al_2O_3 on SiO_2).

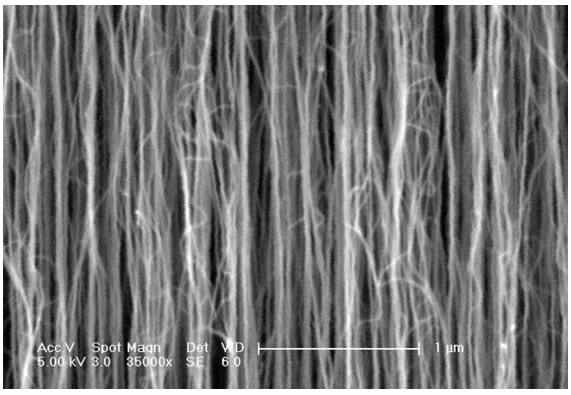

▲ Figure 2: Higher magnification image of the very dense carpet of CNTs of Figure 1.

Templated Self-Assembly for Nano-Particle Organization: Templated, Ordered Porous Alumina Templates

J. Oh, C.V. Thompson
Sponsorship: MARCO IFC, Singapore-MIT Alliance

Nano-sized materials are core building blocks for advanced functional systems such as electronic circuits, memories, sensors, and displays. Due to their size-sensitive electrical, optical, magnetic and chemical properties, it is desirable to fabricate nano-sized materials with controlled size and distribution on the system-applicable substrates. As a strategy, we are developing templated self-assembly methods that combine top-down (lithography) and bottom-up (self-assembly) approaches for fabricating and assembling metallic nano-wires, rods, and dots for new applications including nano-contacts for devices and interconnects for mixed-material and multifunctional micro- and nano-systems.

Anodic aluminum oxide (AAO) is a self-ordered nanostructured material that is suitable as a template in magnetic, electronic, and opto-electronic devices. Under proper anodization conditions, aluminum oxidizes as a porous structure with aligned pores that have a close-packed (hexagonal) order at short range and with pore sizes that can vary from 7 nm-300 nm. While short-range pore ordering can be achieved during anodization, domains (<5 μm) with different repeat directions occur at longer ranges. This breakdown in long-range order limits fabrication of large ordered arrays of devices using porous alumina templates. We developed perfectly ordered porous alumina scaffolds by combining interference lithography with anodization of evaporated Al thin films on silicon substrates. We have achieved regular arrays of pores with diameters of less than 30 nm and aspect ratios >50:1 in insulating alumina. Topographic templating of long-range order in anodic aluminum oxide allows independent control of the pore size, spacing, and order symmetry in ranges not achievable without templating. Using the perfectly-ordered AAO scaffolds, we have fabricated ordered metallic nanodots, nanorods, and nanotubes as well as well-aligned multi-walled carbon nanotubes (CNTs) on silicon substrates. We are currently pursuing the growth of uniform arrays of electrically contacted CNTs in templated AAO scaffolds to obtain statistical, electrical, and thermal characterizations of CNTs as a function of variations in the diameter and length of nanotubes.

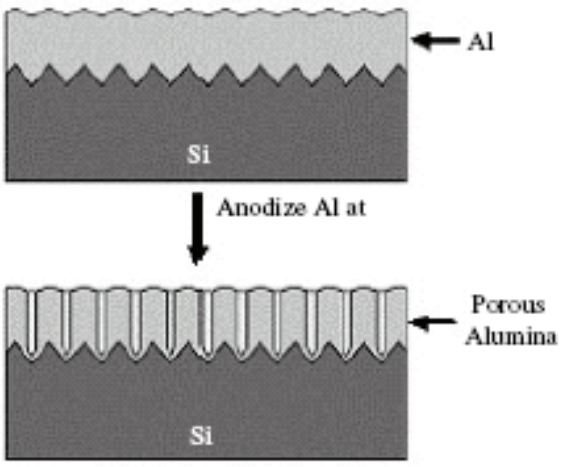

▲ Figure 1: Schematics of fabrication of templated porous alumina scaffold [1].

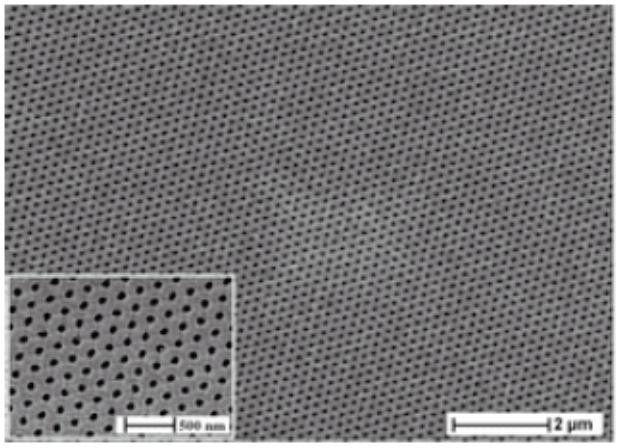

▲ Figure 2: An SEM image of perfectly ordered porous alumina with hexagonal symmetry on silicon-over-wafer-scale areas with pore diameter of 80 nm and pore spacing of 180 nm [1].

REFERENCES

[1] R. Krishnan, H.Q. Nguyen, C.V. Thompson, W.K. Choi, Y.L. Foo, "Wafer-level ordered arrays of aligned carbon nanotubes with controlled size and spacing on silicon," *Nanotechnology*, vol. 16, no. 6, pp. 841-845, 2005.

Templated Dewetting of Nano-Particle Solutions

S.-W. Chang, C.V. Thompson
Sponsorship: Singapore-MIT Alliance

A major issue in nanotechnology is the need for versatile techniques for self-organization of nanometer-scale building blocks, such as nanoparticles, to form large-area periodic systems. Our goal is to combine physical templating and self-assembly to form nanoparticle arrays that can be used as catalysts for the growth of nanowire or nanotube arrays, and other applications such as nanoelectronics or nanophotonics.

A combination of physical templating and capillary interaction has been employed to self-organize colloidal particles into lithographically patterned templates with well-controlled sizes and structures [1]. However, the diameters of the particles studied to date are typically in the range of hundreds of nanometers. The capillary interaction strength decreases with diminishing dimensions due to random thermal fluctuations. Controlling the appropriate parameters may make it possible to overcome the randomizing effects of Brownian motion to extend the templated self-assembly (TSA) approach to sub-50-nm diameter particles.

As an initial effort, patterned substrates with gratings were fabricated using conventional contact-mode photolithography and inserted into nanoparticle solutions for evaporation. The resulting capillary interaction due to solvent evaporation was found to be sufficiently strong to force the nanoparticles into the template trenches without leaving particles on the surrounding areas. Figure 1 presents a schematic outline of the process. Current efforts include applying the templated dewetting approach to smaller nanostructures and on different topographies.

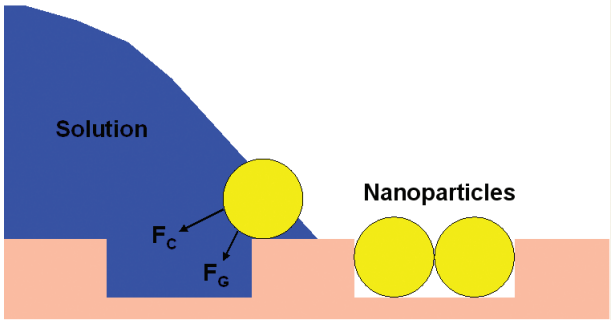

▲ Figure 1: A schematic outline of the assembly process. Forces that may be exerted on the gold particles are shown: capillary force (F_C) and gravitational force (F_G).

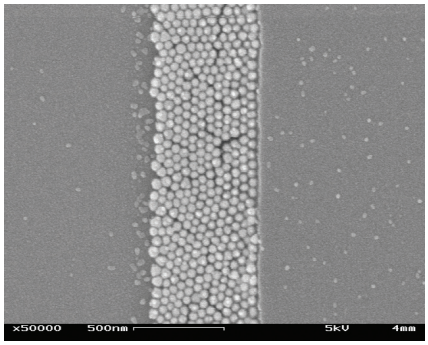

▲ Figure 2: Scanning electron micro-graph of ordered gold nanoparticles assembled in trenches.

REFERENCES:

[1] Y. Yin, Y. Lu, B. Gates, and Y. Xia, "Templated-Assisted Self-Assembly: A Practical Route to Complex Aggregates of Monodispersed Colloids with Well-Defined Sizes," *J. Am. Chem. Soc.* vol. 123, pp. 8718-8729, 2001.

Surface Mound Formation and Stress Evolution during Growth of High-Mobility Metal Films

R. Moenig, J. Leib, A.R. Takahashi, C.V. Thompson
Sponsorship: NSF

Residual stress is an important factor affecting the performance and reliability of many micro-mechanical devices and thin-film structures. In order to control the residual stress of a thin metal film, knowledge of the active stress generation mechanisms is necessary. Our work focuses on structural changes and associated stress effects that occur during the growth of high-mobility metal films, e.g., Au, Cu, Ag, and Al, using evaporative deposition. Film stress measurements using capacitive deflection measurements of Si and SiO_2 cantilevers show tensile stress excursions after the deposition flux is interrupted and compressive changes after the deposition has been resumed [1-2]. Earlier studies using reflected high-energy electron diffraction indicate that stress changes are correlated with changes in surface roughness during growth interruptions [3]. Figure 1 shows a stress curve characteristic for growth interrupts and subsequent growth resumptions of high-mobility metal films. This reversible behavior was observed in Volmer-Weber growth of polycrystalline as well as in epitaxial films. Flash depositions of 1Å of Ta have been used to suppress surface diffusion on a film after interrupting growth in order to allow for atomic-force microscopy imaging of "frozen" films. Figure 2 shows two examples where the Ta flash was performed at different times after the growth had been interrupted. Figure 2 shows that the average mound spacing and the mound area increase during interrupts. Our observations indicate that the step-edge barrier (Ehrlich-Schwoebel-Barrier) that governs the interlayer transport of adatoms has a strong effect on film morphology. This barrier is significantly higher than the barrier for intralayer diffusion and therefore leads to mound formation and growth (roughness) even on high-mobility metal films deposited at RT.

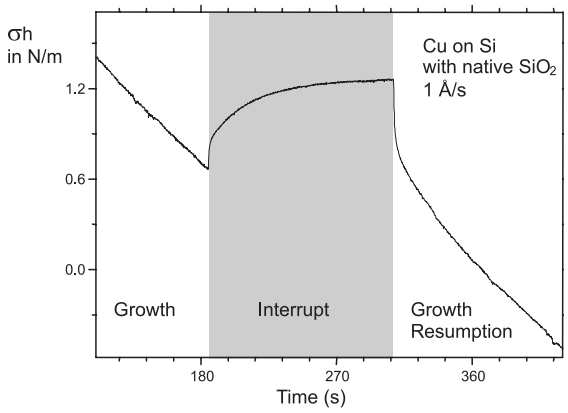

▲ Figure 1: Stress measurement during deposition of Cu on Si with amorphous SiO_2 at RT. The film grows in Volmer-Weber mode and during the growth interrupt the stress experiences a tensile excursion.

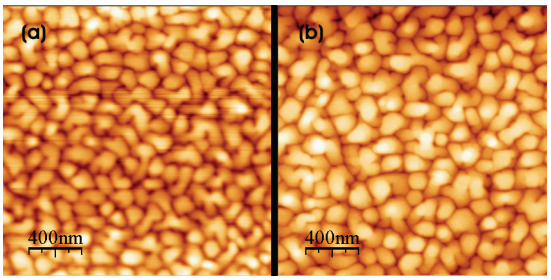

▲ Figure 2: AFM images of a 1000Å Cu film deposited on large-grained Au. a) Ta deposition less than 2 s after Cu growth. b) Ta deposition 5 min after Cu growth was interrupted.

REFERENCES

[1] R. Abermann and R. Koch, "The internal stress in thin silver, copper and gold films," *Thin Solid Films*, vol. 129, pp. 71-78, 1985.

[2] C. Friesen, S.C. Seel, C.V. Thompson, "Reversible stress changes at all stages of Volmer–Weber film growth," *J. Appl. Phys.*, vol. 95, no. 3, pp. 1011-1020, 2004.

[3] C. Friesen and C.V. Thompson, "Correlation of stress and atomic-scale surface roughness evolution during intermittent homoepitaxial growth of (111)-oriented Ag and Cu," *Phys. Rev. Lett.*, vol. 93, no. 5, pp. 056104:1-4, July 2004.

Stress and Structure Evolution Film Formation through Island Coalescence

A.R. Takahashi, J. Leib, R. Moenig, C.V. Thompson
Sponsorship: NSF

When thin films form through the Volmer-Weber mechanism, growth initiates through the nucleation and growth of isolated single-crystal nano-scale islands. As these islands impinge and coalesce to form a continuous film, dramatic evolution in the residual stress and microstructure of the film occurs. Island coalescence generates a tensile stress as islands strain towards each other to eliminate surface area [1-3]. While new models for the magnitude of the tensile stress due to coalescence [3-5] provide results that match experiments, the assumptions required to make these models tractable preclude a realistic consideration of the microstructure evolution. To complement analytic and numerical models for the magnitude of stress, we have initiated computational studies of microstructural evolution during boundary formation. The computational approach relies mainly on semi-empirical molecular dynamics (MD) calculations and some continuum finite element analysis(FEA)[6]. Using a fully atomistic approach such as MD provides direct insight into the types of boundaries formed during coalescence and their effect on continued structure evolution. An interesting preliminary result from atomistic modeling is that the boundary formation process can generate secondary defects such as stacking faults (Figure 1). For larger islands, the stress generated is insufficient to propagate defects and for smaller islands, size-strengthening inhibits formation of defects. However, in an intermediate range of island sizes, stacking faults are readily formed. Transmission electron microscopy (TEM) of late-stage coalescence films does show a high density of stacking faults and twins but the origin of these defects is still unclear (Figure 2). Future experiments will focus on controlling the size of islands at coalescence and characterizing the distribution of defect types formed for different size ranges.

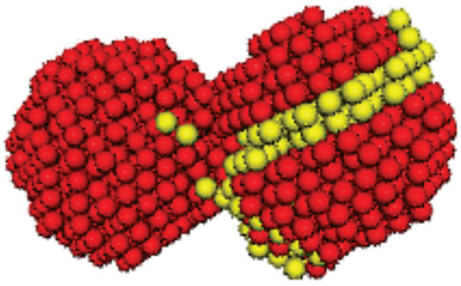

▲ Figure 1: Computer calculated stacking fault resulting from boundary formation. This type of defect is observed frequently in calculations of islands in the 3-to 5-nm diameter range.

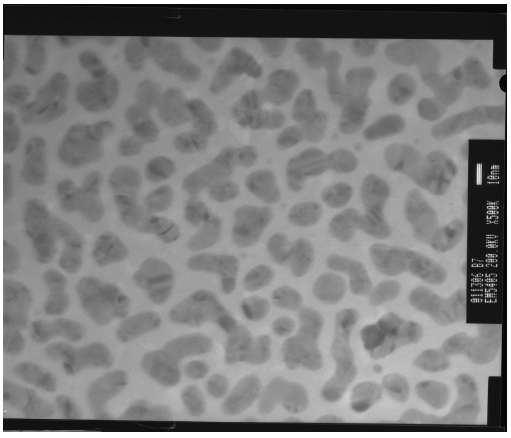

▲ Figure 2: Micrograph of later stage coalescence of Au on a thin silicon nitride membrane. Stacking faults are evident in several of the coalesced island structures.

REFERENCES

[1] R.W. Hoffman, "Stresses in thin films: The relevance of grain boundaries and impurities," *Thin Solid Films*, vol. 34, pp. 185-190, 1976.

[2] W.D. Nix and B.M. Clemens, "Crystallite coalescence: A mechanism for intrinsic tensile stresses in thin films," *J. of Materials Research*, vol. 14, pp. 3467-3473, 2000.

[3] L.B. Freund and E. Chason, "Model for stress generated upon contact of neighboring islands on the surface of a substrate," *J. of App. Physics*, vol. 89, pp. 4866-4873, 2001.

[4] S.C. Seel, C.V. Thompson, S.J. Hearne, and J.A. Floro, "Tensile stress evolution during deposition of Volmer-Weber thin films," *J. of App. Physics*, vol. 88, pp. 7079-7088, 2000.

[5] S.J. Hearne, S.C. Seel, J.A. Floro, C.W. Dyck, W. Fan, and S.R.J. Brueck, "Quantitative determination of tensile stress creation during island coalescence using selective-area growth," *J. of App. Physics* vol. 97, p. 083530, 2005.

[6] A.R. Takahashi, *Materials Research Soc. Proc.*, vol. 779, 2003.

Hybrid Carbon Nanotube-Composite Architectures

E.J. García, A.J. Hart, K. Sorensen, B.L. Wardle (in coll. with A.H. Slocum)
Sponsorship: La Caixa Foundation

Hybrid composite architectures employing traditional advanced composites and carbon nanotubes (CNTs) offer significant potential mechanical and multifunctional performance benefits. Dense patterns of well-aligned carbon nanotubes (CNTs) were grown on silicon wafers using a thermal chemical vapor deposition (CVD) process [1]. Wetting of CNTs and retention of mechanical properties of the fibers after the CVD process are considered fundamental issues related to realizing novel hybrid composite architectures. Wetting of CNT forests by several commercial polymers (including a highly-viscous epoxy, as shown in Figure 1) has been demonstrated at rates conducive to creating a fully-dispersed CNT/matrix region around the fibers in hybrid architectures [2]. A new microfabrication method [3] was developed to create well-aligned, regularly contracted pillars. The basic mechanical properties (elastic modulus, strength) of the polymer and the CNT/polymer nanocomposite were obtained by means of a nanoindenter to apply a compression test to the vertically aligned circular composite pillars [3]. The elastic modulus was obtained using the Oliver-Pharr theory adapted to the flat punch used in the experiments. These intermediate architectures of aligned CNTs in a polymer matrix are being employed to create more sophisticated architectures utilizing advanced fibers and prepregs of traditional advanced composites [4-5]. The dense, aligned, high-quality forests of CNTs grown at high rates (~50 microns per minute) suggest that the process is scalable for incorporation into traditional composites. Single-fiber tension tests [6] indicate no mechanical degradation for fibers undergoing the CNT growth process, as shown in Figure 2c). Results indicate that hybrid CNT/composite architectures are feasible; future work focuses on mechanical and multifunctional property characterization of other hybrid architectures and scaling to a continuous CNT growth process.

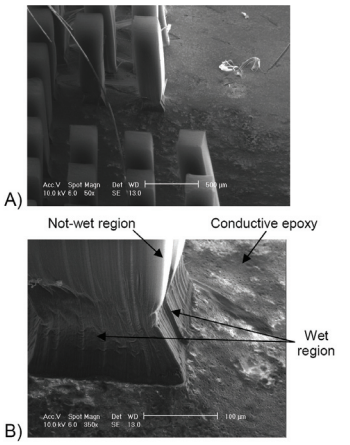

▲ Figure 1: A) Pattern of CNT pillars wet by 20-minute-curing, high-viscosity epoxy resin; B) Close-up of the wet region at the base of the pillar.

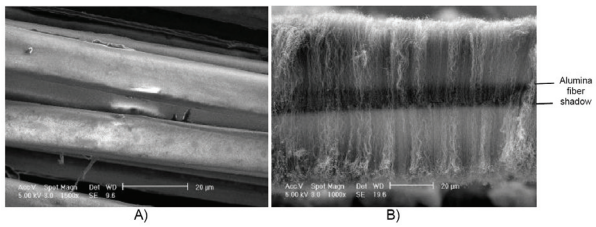

	Tensile strength [GPa]		Young's modulus [GPa]		Strain-to-failure [%]	
	Mean	Standard deviation	Mean	Standard deviation	Mean	Standard deviation
Pure alumina fiber	2.19	0.19	135	6.38	1.63	0.13
Alumina soaked in catalyst	2.30	0.21	138	12.6	1.73	0.06
Alumina fibers with CNTs	2.28	0.09	134	11.3	1.63	0.16

C)

▲ Figure 2: A) Pure alumina fiber; B) Alumina fiber (shadow behind CNTs) with well-aligned, 30-µm-long CNTs grown on its surface; C) Experimental results for pure alumina fibers, fibers soaked with catalyst, and fibers after the CNT growth process.

REFERENCES

[1] A.J. Hart and A.H. Slocum, "Flow-mediated nucleation and rapid growth of millimeter-scale, aligned, carbon nanotube structures from a thin-film catalyst," *J. of Physical Chemistry B*, vol. 110, no.16, pp. 8250-8257, 2006

[2] E.J. García, A.J. Hart, B.L. Wardle, and A.H. Slocum, "Fabrication and testing of long carbon nanotubes grown on the surface of fibers for hybrid composites," AIAA-2006-1854, *Proc. 47th AIAA/ASME/ASCE/AH/ Conf.*, Newport, R.I., May 2006.

[3] E.J. García, A.J. Hart, B.L. Wardle, and A.H. Slocum, "Fabrication of CNT/polymer nanocomposites and characterization of their mechanical properties using nanoindentation/compression tests," to be presented at *Proc. ASME IMECE Conf.*, Chicago, IL, Nov. 2006.

[4] B.L. Wardle and S.G. Kim. "Nano-engineered material architectures: Ultra-tough hybrid nanocomposite system," MIT TLO Case 11260, 2005.

[5] E.J. García, A.J. Hart, A.H. Slocum, and B.L. Wardle. "Production of reinforced composite materials and aligned carbon nanotubes," MIT TLO Case 12029, 2005.

[6] ASTM C 1557 – 03. "Standard test method for tensile strength and Young's modulus of fibers," ASTM International, 2003.